

Ground based radar observations of wind turbines

Chuck Livingstone
Shen Chiu
DRDC - Ottawa Research Centre

Defence Research and Development Canada

Scientific Report
DRDC-RDDC-2014-R57
August 2014

Ground based radar observations of wind turbines

Chuck Livingstone
Shen Chiu
DRDC - Ottawa Research Centre

Defence Research and Development Canada

Scientific Report
DRDC-RDDC-2014-R57
August 2014

- © Her Majesty the Queen in Right of Canada, as represented by the Minister of National Defence, 2014
- © Sa Majesté la Reine (en droit du Canada), telle que représentée par le ministre de la Défense nationale, 2014

Abstract

Wind turbines are large radar targets whose radar cross sections (RCS) contain both static and dynamic components that are major interference sources for air traffic surveillance radars (ASRs). Investigations in response to a Canadian Air Force support request revealed that currently available wind-turbine RCS models are too primitive to answer the ASR interference questions asked. This report documents the development of a first-order RCS model that uses environmental conditions to replicate the static and dynamic effects present in the radar returns from wind turbines and generates the expected Doppler signatures of wind turbine targets that cause ASR interference effects. The model uses measured data from reference wind turbines and uses published results from detailed electromagnetic scattering models to create a semi-empirical description of a wind turbine target that replicates the target's properties under all normal operating conditions. The model includes scaling laws that allow it to be used for a wide range of commercial wind turbines whose detailed designs differ from the reference cases used for model development. The model contains a terrain screening filter that allows the radar returns from a partially screened turbine to be replicated for ASR interference analysis. Results obtained from the model closely replicate published, observed effects for wind turbine targets. RCS estimates are judged to be accurate to within 5 dBm².

Significance to defence and security

This report is part of the DRDC (Defence Research and Development Canada) response to an RCAF (Royal Canadian Air Force), Director of Air Domain Development request for support in evaluating the impact of planned and existing wind turbines on air traffic surveillance radars that are currently in service and their planned replacements. The report describes wind turbines as radar targets in a form that is applicable to generic radars that perform air traffic control functions.

The first-order wind-turbine radar signature model described in this report is being considered by NORAD as an input to their active target modelling R&D.

Résumé

Les surfaces équivalentes radar (RCS) des éoliennes comptent tant des éléments dynamiques que des éléments statiques; cela en fait de fortes sources d'interférences pour les radars de surveillance aérienne (ASR). Des études faites à la suite d'une demande de soutien de la Force aérienne du Canada ont révélé que les modèles RCS actuels des éoliennes sont trop simplistes pour répondre adéquatement aux questions sur les interférences touchant les ASR. Le rapport décrit le développement d'un modèle RCS de premier ordre qui reproduit à l'aide des conditions ambiantes les effets sur l'écho radar des éléments statiques et dynamiques des éoliennes et qui génère les signatures Doppler prévues des éoliennes qui créent les interférences touchant les ASR. À l'aide de données mesurées d'éoliennes de référence et de résultats publiés de modèles détaillés de diffusion électromagnétique, le modèle crée une description semi-empirique d'une éolienne qui en reproduit les propriétés dans toutes les conditions ambiantes normales. Le modèle intègre aussi des règles d'échelonnage qui lui permet de reproduire un grand nombre d'éoliennes commerciales dont la conception détaillée diffère des éoliennes de référence utilisées pour le développer. Il comporte aussi un modèle de filtrage du terrain qui permet aux fins d'analyse des interférences ASR de reproduire les échos radar d'une éolienne partiellement occultée par le terrain. Ce modèle reproduit étroitement les effets radar observés et publiés des éoliennes. Nous jugeons que les surfaces équivalentes radar sont fidèles à une précision de plus ou moins 5 dBm².

Importance pour la défense et la sécurité

Le rapport fait partie d'une réponse de Recherche et développement pour la défense Canada (RDDC) à une demande de soutien provenant du Directeur – Développement du domaine aérien, Aviation royale du Canada (ARC) visant à évaluer les répercussions des éoliennes existantes et prévues sur les radars de surveillance aérienne en service et sur leurs successeurs. Le rapport décrit les éoliennes en tant que cibles radar sous une forme utile aux radars génériques qui servent au contrôle de la circulation aérienne.

L'OTAN envisage d'utiliser le modèle RCS de premier ordre de la signature radar des éoliennes décrit dans ce rapport pour ses efforts de R et D en modélisation des cibles actives.

Table of contents

Abstract	i
Significance to defence and security	i
Résumé	ii
Importance pour la défense et la sécurité	ii
Table of contents	iii
List of figures	v
List of tables	viii
1 Introduction.....	1
2 Wind turbine operating constraints and rotor geometries	3
2.1 Turbine size	3
2.2 Blade design	4
2.3 Turbine operating profile.....	10
2.3.1 Dynamic control, blade pitch	10
2.3.2 Dynamic control, turbine yaw	15
3 Radar observations of wind turbines.....	17
3.1 Wind turbines as radar targets	17
3.2 Air traffic and weather radar observations of wind turbines	28
3.2.1 ASR primary surveillance radars	28
3.2.2 ASR observations of wind turbines.....	29
4 Modelling wind turbine effects	35
4.1 Static RCS effects and scaling laws	37
4.1.1 Wind turbine towers.....	37
4.1.2 Wind turbine nacelles.....	38
4.2 Dynamic RCS effects	40
4.2.1 Wind speed effects	40
4.2.2 Rotor RCS model for yaw angles -175° to -5° and 5° to 175°	42
4.2.3 Rotor RCS model for yaw angles within $\pm 5^{\circ}$ of 0° and $\pm 180^{\circ}$	52
4.2.4 Yaw and pitch angle effects for turbine rotor RCS	57
4.2.5 Terrain height masks	61
4.3 Wind turbine RCS model implementation	67
5 Wind-farm arrays of wind turbines	69
6 Conclusions and summary	74
References	77
Annex A Turbine blade models	81
Annex B Turbine RCS models	83
B.1 Empirical observations	83

List of figures

Figure 1	Rated power for commercial wind turbines as a function of turbine radius.	4
Figure 2	Fiberglass composite blade with carbon fiber components.	5
Figure 3	Lightning protection strategies in current use.	6
Figure 4	Composite fiberglass, carbon fiber blade design showing the box-beam spar. ...	7
Figure 5	The relationship between turbine blade twist and the apparent wind direction. ...	8
Figure 6	Calculated blade twist angle for a 20 MW turbine (initial design).	9
Figure 7	A typical wind turbine power curve.	10
Figure 8	Wind turbine blade angle of attack.	11
Figure 9	Schematic airfoil response to its angle of attack.	12
Figure 10	Analytical approximation of $CP(\lambda, \beta)$ for blade pitch angle in degrees.	13
Figure 11	Vertical wind shear, height (m) vs. mean wind speed (m/s).	14
Figure 12	Wind turbine blade pitch angles over a full rotor rotation for independently controlled blades.	15
Figure 13	Radar scattering model calculations for fiberglass turbine blades at 3 GHz radar frequency.	18
Figure 14	Radar reflection coefficients for various shell thicknesses as a function of local incidence angle.	19
Figure 15	Model results for the relationship between the radar Doppler shift in Hz and the RCS in dBm ² when the blade root components are suppressed.	20
Figure 16	Anechoic chamber measurements of a model section of a turbine blade.	21
Figure 17	3 GHz radar cross section for an Enercon E66 wind turbine viewed at 90° to the turbine shaft axis at 23 RPM rotation rate [14] as derived from the radar video output.	22
Figure 18	Time frequency display of the Doppler returns from the Enercon E 66 wind turbine at Swaffham UK for the data displayed as RCS in Figure 17.	23
Figure 19	Enercon E66 turbine Doppler spectrum for radar observation of the rotor disk plane at -10° yaw angle.	24
Figure 20	Enercon E66 turbine Doppler spectrum for radar observations of the rotor disk edge.	25
Figure 21	Modeled radar cross section of an Enercon E66 turbine at 0° yaw angle.	26
Figure 22	Turbine blade locations for figure 20.	26
Figure 23	3.05 GHz measurements of an Enercon E66 turbine at 0° yaw angle.	27
Figure 24	Doppler spectrum-time plot measured for an Enercon E66 turbine at 0° yaw. ...	28
Figure 25	Enercon E66 nacelle RCS from model calculations.	30
Figure 26	Vestas V47 nacelle RCS from model calculations.	31
Figure 27	S-band air traffic control radar azimuth pattern.	32

Figure 28	ISAR spotlight image of a REpower MM82 82 m wind turbine rotor.	33
Figure 29	High resolution range-Doppler image of a REPOWER MM82 wind turbine at 90° yaw angle.....	34
Figure 30	Side view schematic of the Enercon E66 turbine showing the nacelle profile and the major internal components.	38
Figure 31	Vestas V80 wind turbine nacelle.	39
Figure 32	Wind power curve for a 2 MW Enercon turbine.....	42
Figure 33	Schematic plan view of the turbine blade.	43
Figure 34	Enercon E66 measured (blue) and predicted (red) Doppler spectrum over 1.5 rotations.....	44
Figure 35	Linear segmental models of the normalized Doppler spectrum in Figure 34 in dB..	46
Figure 36	Normalized blade cross section functions for the Doppler spectrum in Figure 34....	46
Figure 37	Single blade RCS in m2 for a blade vertically up.....	48
Figure 38	Spectral history for the Enercon E66 reference model turning at 16 RPM and viewed at -90° yaw angle. The color bar gives the turbine rotor RCS in dBm2..	49
Figure 39	Enercon E66 rotor RCS at yaw angle 90° and rotation rate 16 RPM.	50
Figure 40	Enercon E66 reference turbine RCS.	50
Figure 41	Enercon E66 turbine RCS after a two-pole high pass filter with 55 Hz cut-off...	52
Figure 42	Rotor RCS for a 126 m diameter turbine as a function of yaw angle when one blade is vertically up from [22] Figure 78.	58
Figure 43	Simplified rotor RCS yaw dependence from Table 5 scaled for the Enercon E66 turbine.....	60
Figure 44	Enercon E66 turbine radar cross section in m2 for -90° yaw as a function of terrain mask height at the turbine base when the turbine blades are vertically down.....	65
Figure 45	Enercon E66 turbine radar cross section in m2 for -90° yaw as a function of terrain mask height at the turbine base when the turbine blades are vertically up.	66
Figure 46	Doppler returns form an Enercon E66 turbine viewed at -90° yaw when the turbine is turning at 16 RPM as a function of terrain mask height in m.	66
Figure 47	Wind turbine wakes in an ocean wind farm under favorable atmospheric conditions.....	70
Figure 48	Wolfe Island wind farm turbine locations corresponding to Table 6. The yellow arrow indicates the approximate wind direction.	71
Figure B.1	Data extracted from a figure in [15] for an Enercon E66 turbine nacelle modeled at 3.0 GHz and 1.0 GHz.	84
Figure B.2	Enercon E66 turbine nacelle RCS at 3.0 GH.	86
Figure B.3	Model residuals for the Enercon E66 turbine nacelle model.	87
Figure B.4	Data extracted from a figure in [15] for a Vestas V47 turbine nacelle modeled at 3.0 GHz and 1.0 GHz.....	88
Figure B.5	Vestas V47 nacelle model RCS showing the source data points.	90

Figure B.6	Vestas V47 nacelle model residuals.....	90
Figure C.1	(a) Turbine RCS at -10° yaw angle (b) Turbine power spectrum as a function of rotation time. The color bar scale is the power density in dBm2.	95
Figure C.2	(a) Turbine RCS at -20° yaw angle (b) Turbine power spectrum as a function of rotation time. The color bar scale is the power density in dBm2.	96
Figure C.3	(a) Turbine RCS at -30° yaw angle (b) Turbine power spectrum as a function of rotation time. The color bar scale is the power density in dBm2.	96
Figure C.4	(a) Turbine RCS at -40° yaw angle (b) Turbine power spectrum as a function of rotation time. The color bar scale is the power density in dBm2.	97
Figure C.5	(a) Turbine RCS at -50° yaw angle (b) Turbine power spectrum as a function of rotation time. The color bar scale is the power density in dBm2.	97
Figure C.6	(a) Turbine RCS at -60° yaw angle (b) Turbine power spectrum as a function of rotation time. The color bar scale is the power density in dBm2.	98
Figure C.7	(a) Turbine RCS at -70° yaw angle (b) Turbine power spectrum as a function of rotation time. The color bar scale is the power density in dBm2.	98
Figure C.8	(a) Turbine RCS at -80° yaw angle (b) Turbine power spectrum as a function of rotation time. The color bar scale is the power density in dBm2.	99
Figure C.9	(a) Turbine RCS at -90° yaw angle (b) Turbine power spectrum as a function of rotation time. The color bar scale is the power density in dBm2.	99
Figure C.10	(a) Turbine RCS at -100° yaw angle (b) Turbine power spectrum as a function of rotation time. The color bar scale is the power density in dBm2.	100
Figure C.11	(a) Turbine RCS at -110° yaw angle (b) Turbine power spectrum as a function of rotation time. The color bar scale is the power density in dBm2.	100
Figure C.12	(a) Turbine RCS at -120° yaw angle (b) Turbine power spectrum as a function of rotation time. The color bar scale is the power density in dBm2.	101
Figure C.13	(a) Turbine RCS at -130° yaw angle (b) Turbine power spectrum as a function of rotation time. The color bar scale is the power density in dBm2.	101
Figure C.14	(a) Turbine RCS at -140° yaw angle (b) Turbine power spectrum as a function of rotation time. The color bar scale is the power density in dBm2.	102
Figure C.15	(a) Turbine RCS at -150° yaw angle (b) Turbine power spectrum as a function of rotation time. The color bar scale is the power density in dBm2.	102
Figure C.16	(a) Turbine RCS at -160° yaw angle (b) Turbine power spectrum as a function of rotation time. The color bar scale is the power density in dBm.	103
Figure C.17	(a) Turbine RCS at -170° yaw angle (b) Turbine power spectrum as a function of rotation time. The color bar scale is the power density in dBm2.	103

List of tables

Table 1	Airfoil data for a 5 MW turbine with a 61.6 m blade.	9
Table 2	Wind speed vs. pitch angle relationship for a 5 MW turbine.....	13
Table 3	Enercon E66 normalized Doppler spectrum for the blade trailing edge (negative Doppler).	45
Table 4	Enercon E66 normalized Doppler spectrum for the blade leading edge (positive Doppler).	45
Table 5	Normalized yaw dependence of the turbine blade RCS.....	59
Table 6	Symmetrized yaw dependence of the turbine blade RCS.	59
Table 7	Selected model parameters.....	61
Table 8	Wolfe Island wind turbine operating condition measurements for October 9, 2009 at 23 h UTC.....	72
Table B.1	Enercon E66 nacelle Fourier coefficients.	85
Table B.2	Vestas nacelle Fourier coefficients.	89

1 Introduction

Following inquiries by RCAF personnel, DRDC (Defence Research and Development Canada) investigated the impact of the radar signatures of commercial wind turbines on Airport Surveillance Radars (ASRs). Initial DRDC studies [1] revealed that the available wind-turbine radar cross section (RCS) models were too primitive to answer some of the questions asked about wind turbine interference with ASR detection and tracking functions. The DRDC research effort was extended to include the development of a first-order RCS (radar cross section) model that captured all of the major static and dynamic wind-turbine RCS components that can influence ASR performance with and without terrain masking effects to provide a tool for characterizing wind turbines as radar targets.

To support the wind turbine RCS model development, design information and operating characteristics for commercial, horizontal-axis power generation turbines were examined to identify common parameters that could be generalized into a model structure that can be used to represent the dynamic RCS signature of a typical turbine. Selected radar RCS measurements were combined with detailed electromagnetic scattering model results to create a semi-empirical model that:

1. Combines wind direction and radar look direction to estimate the turbine yaw angle that is observed by the radar,
2. Captures wind speed effects on turbine rotation rates,
3. Computes the turbine tower and nacelle contributions to the wind turbine RCS,
4. Computes the turbine rotor RCS as a function of radius,
5. Computes the turbine Doppler power spectrum that is observed by an ASR, and
6. Applies a terrain shadowing mask to ASR returns from a wind turbine.

Where published information was not available to define model details, reasonable assumptions were used to qualitatively emulate observed effects. The assumptions are clearly identified in this report. The first-order model developed in this report does not include coherent fading effects that will be observed in actual observations nor does it include multipath scattering from intervening terrain.

Although the model was developed using details from specific wind turbines, scaling rules have been incorporated to allow its generalization to most systems. The data used in the model are specific to S-band ASRs that are in common use across Canada. RCS reduction technologies that are currently being investigated are not included in the model.

The report is organized as follows:

1. Chapter 2 discusses wind turbine geometry and operating constraints,

2. Chapter 3 discusses radar observations of wind turbines,
3. Chapter 4 discusses the model development and the algorithms used in the model to generate the turbine RCS and Doppler signatures without and with terrain masking,
4. Chapter 5 introduces factors that need to be considered when the turbine is part of a wind-farm array,
5. Chapter 6 summarizes the report,
6. Annex A presents published electromagnetic scattering model results for a selection of turbine blade types,
7. Annex B.1 describes the development of the turbine nacelle RCS models,
8. Annex B.2 introduces the Matlab script modules that were used to generate the results in this report and
9. Annex C presents example results showing the yaw angle dependence of radar signatures for a reference turbine.

The Matlab code referred to in Annex B.2 is internally documented and has been designed in a modular fashion to allow the inclusion of additional experimental data as they become available.

2 Wind turbine operating constraints and rotor geometries

2.1 Turbine size

The turbine designs used for commercial power systems are based on the desired rated power per turbine and the expected wind fields at the turbine site. The turbine power output is a function of the area swept by the rotating turbine blades A , the average wind speed over the rotor v , the local air density ρ , and the turbine blade power factor C_P [2]:

$$P_{Turbine} = \frac{n}{2} C_P(\lambda, \beta) \rho A v^3 \quad (1)$$

In equation (1), the turbine power factor C_P is a semi-empirical function of the turbine blade tip speed ratio $\lambda = \frac{\omega R}{v}$ (where ω is the angular velocity of the rotor and R is the turbine radius) and β is the rotor blade pitch angle measured from the turbine shaft axis. C_P is a function of the integrated aerodynamic lift to drag ratio along a rotor blade and is modulated by the control parameter β to control the rotor speed and thus the output power.

For commercial wind turbines the number of blades, n , is chosen as 3 for efficiency and cost reasons [3].

Figure 1 summarizes the relationship between the rated power of 28 commercial wind turbines and their rotor radii. In current wind-farm design practice, terrestrial wind turbines have rated powers less than 4 MW. The rotor radii are determined by the rated power, the expected wind stability and the local wind speed statistics that have been projected to include extreme 50 year events. A typical wind turbine design life is 20 years.

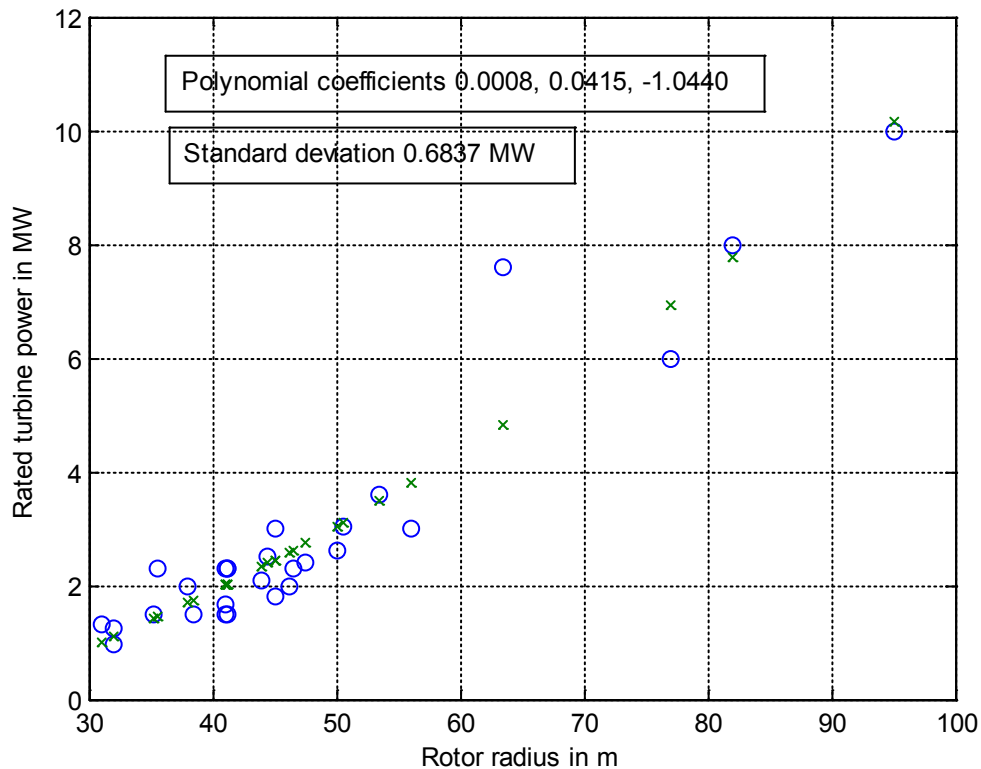


Figure 1: Rated power for commercial wind turbines as a function of turbine radius.

The height of the turbine mounting tower is determined by ground and vegetation clearance, by the typical wind field vertical profile in the wind farm area and by cost.

2.2 Blade design

Although early commercial wind turbines used metallic blades, the large rotors required for economical wind farm design favor blades built of fiberglass or carbon fiber composites [4]. Typical designs use a cylindrical section to mount the blade to the turbine hub followed by a twisted airfoil whose chord length and thickness decreases from the start of the airfoil section at the hub end to the blade tip. Figures 2, 3 and 4 show typical design features [5], [6].

The designs show the use of foam core panel sections and carbon fiber composite in the structural central spar of the blade. Both single and box-beam [7] spars are used. Lightning protection is provided by the use of a metalized blade tip, embedded lightning receptors along the blade length [8], internal lightning conductors and grounding mechanisms across mechanical drive components. Although the carbon-fiber composites used for internal reinforcing of blade structures are conductive, they can be damaged by the large currents found in a lightning strike and are not part of the lightning protection system. Figure 3 illustrates the major components of various lightning protection strategies. Typically lightning receptors are dispersed over the blade and are often clustered near the blade tip.

Blade shapes and construction details vary for specific designs with blade length. A European commission reference design study for a 64.5 m long blade [9] for a 5 MW turbine provides information on the laminate thickness and layer structure over the blade surface. In the blade root and along the central spar, solid laminate thickness varies from 10.6 cm at the blade root to 2.58 cm at 49 m radius and a laminate-foam-core composite forms the outer end of the blade.

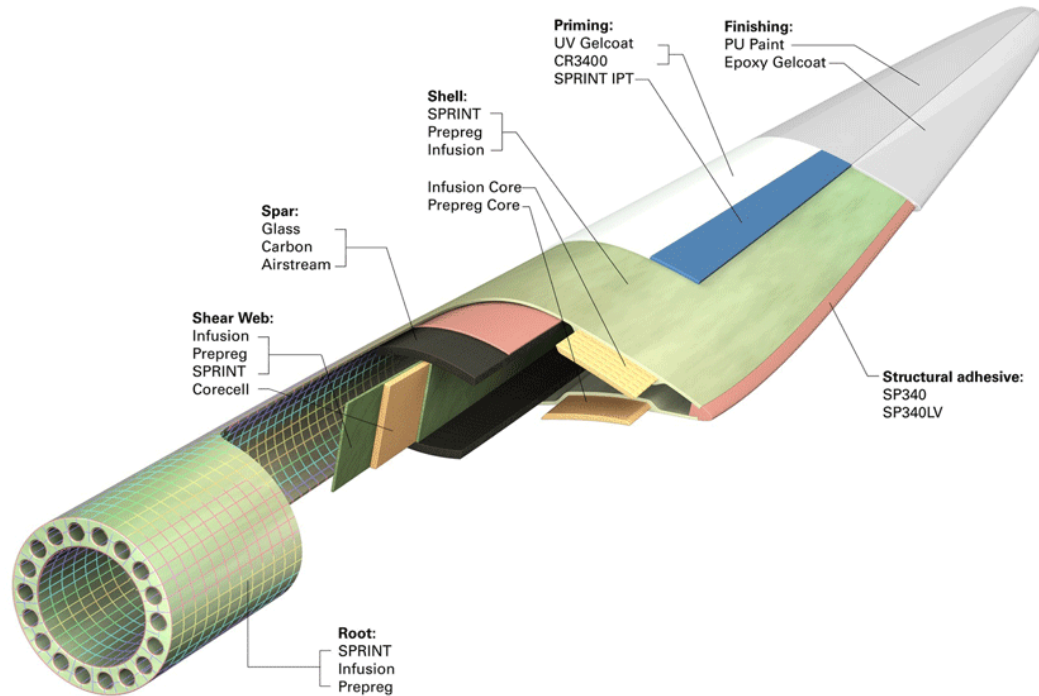


Figure 2: Fiberglass composite blade with carbon fiber components.

Illustration credit: reference [4].

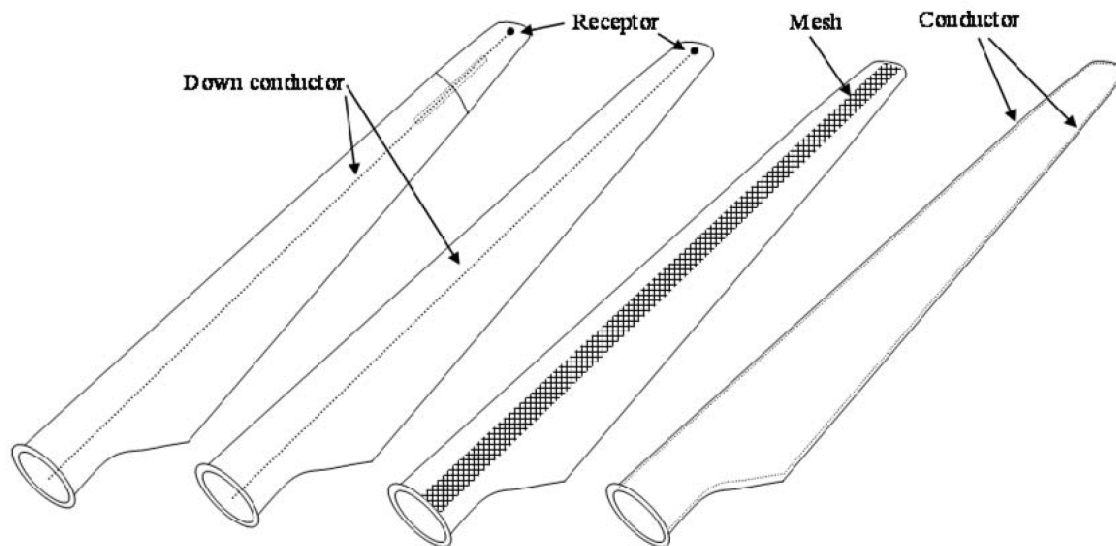


Figure 3: *Lightning protection strategies in current use.*

Illustration credit: reference [2].

The two left configurations in Figure 3 differ by the presence of a metal coated blade tip in the leftmost illustration.

Gamesa: G87 and G90 Blade Design

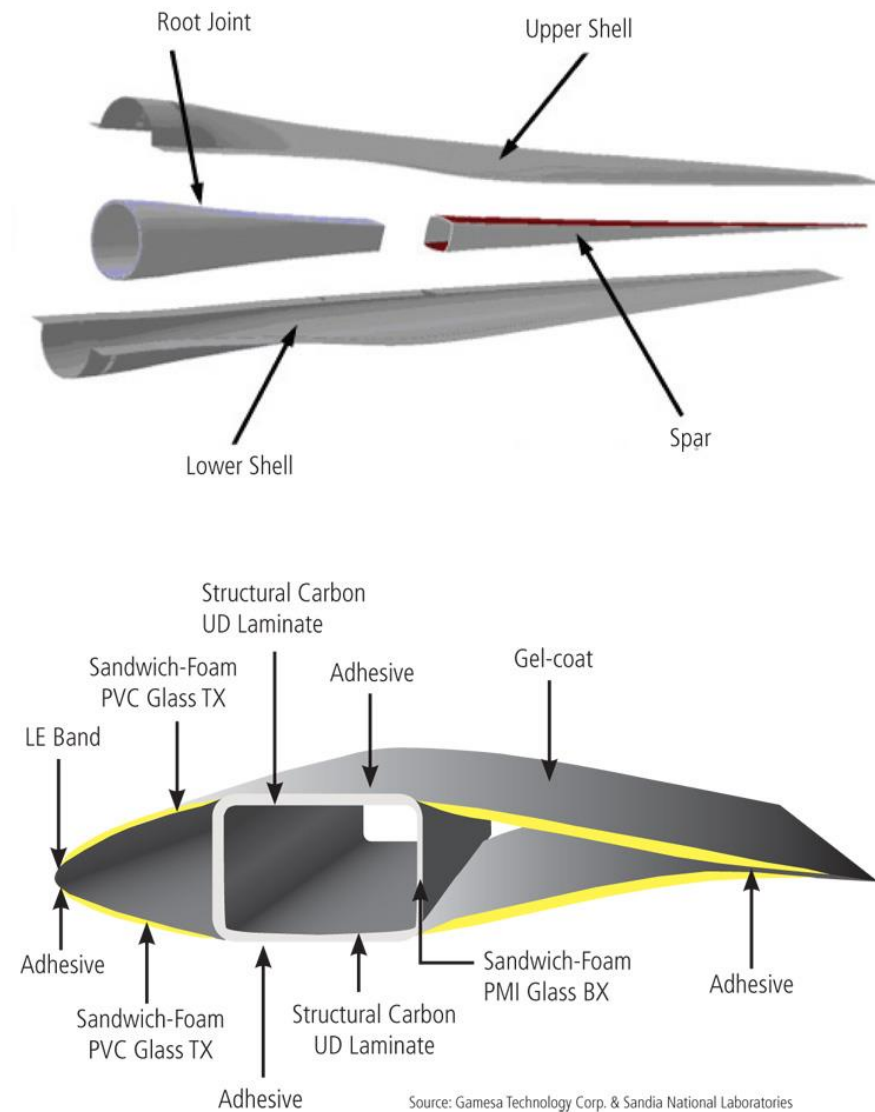


Figure 4: Composite fiberglass, carbon fiber blade design showing the box-beam spar.

Illustration credit: reference [5].

Turbine blades twist towards the rotor plane along their length to optimize the local angle of attack of the blade airfoil along the blade to compensate for the blade rotation component of the effective air velocity [6] as shown in Figure 5. In Figure 5, note that the vector diagrams have been rotated 90°. The blade speed vector is actually out of the page. Figure 6 shows blade twist calculation results for a very large (20 MW) wind turbine [10]. The twist angles in Figure 6 employ an older European convention where a comma is used as a decimal point. The blue curve in Figure 6 shows the blade twist decreasing almost linearly over the outer 100 m of the blade length (from the blade root to the fully-formed airfoil). This curve is scaled to blade size from

conventional design. The blade twist angle range is a function of blade size and typically is between 9° and 12° over the length of the blade.

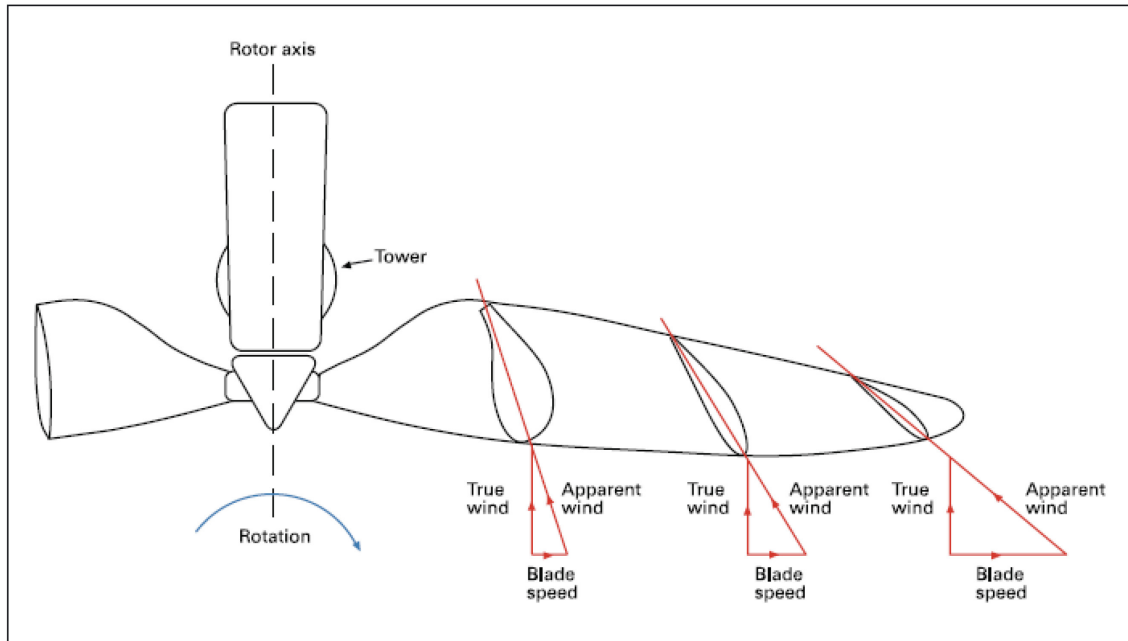


Figure 5: The relationship between turbine blade twist and the apparent wind direction.

Illustration credit: reference [32].

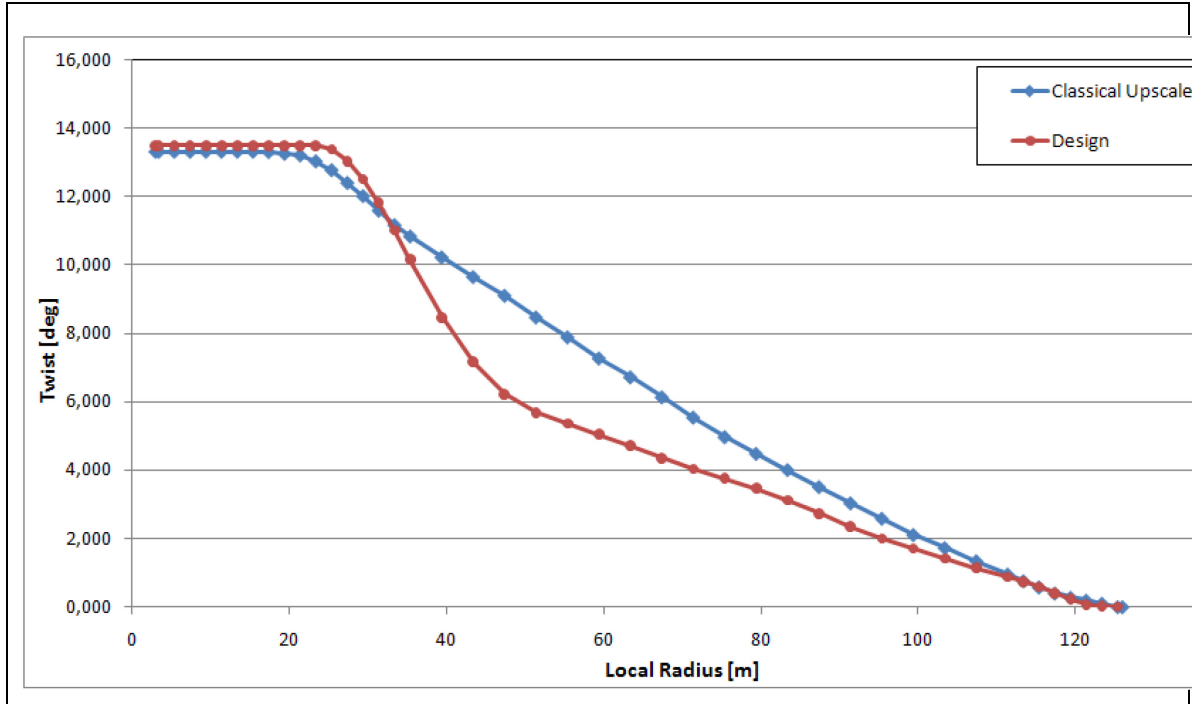


Figure 6: Calculated blade twist angle for a 20 MW turbine (initial design).

Illustration credit: reference [6].

Table 1 shows turbine blade twist angles for a 5 MW offshore turbine design [7].

Table 1: Airfoil data for a 5 MW turbine with a 61.6 m blade.

Node (-)	RNodes (m)	AeroTwst (°)	DRNodes (m)	Chord (m)	Airfoil Table (-)
1	2.8667	13.308	2.7333	3.542	Cylinder1.dat
2	5.6000	13.308	2.7333	3.854	Cylinder1.dat
3	9.3333	13.308	2.7333	4.167	Cylinder2.dat
4	11.7500	13.308	4.1000	4.557	DU40_A17.dat
5	15.8500	11.480	4.1000	4.652	DU35_A17.dat
6	19.9500	10.162	4.1000	4.458	DU35_A17.dat
7	24.0500	9.011	4.1000	4.249	DU30_A17.dat
8	28.1500	7.795	4.1000	4.007	DU25_A17.dat
9	32.2500	6.544	4.1000	3.749	DU25_A17.dat
10	36.3500	5.361	4.1000	3.502	DU21_A17.dat
11	40.4500	4.188	4.1000	3.256	DU21_A17.dat
12	44.5500	3.125	4.1000	3.010	NACA64_A17.dat
13	48.6500	2.319	4.1000	2.764	NACA64_A17.dat
14	52.7500	1.526	4.1000	2.519	NACA64_A17.dat
15	56.1667	0.963	2.7333	2.313	NACA64_A17.dat
16	58.9000	0.370	2.7333	2.086	NACA64_A17.dat
17	61.6333	0.106	2.7333	1.419	NACA64_A17.dat

The RNodes column in Table 1 is the distance from the blade root in m, the Chord column is the airfoil chord length in m, and the Airfoil table identifies the airfoil type (shape) used in the reference design being studied.

2.3 Turbine operating profile

Large-scale commercial wind turbines are designed to generate power over a range of turbine rotation rates. For very low wind speeds the wind energy is insufficient to turn the turbine rotor and the turbine does not respond to the wind. When the wind speed exceeds the cut-in value, the turbine operates at maximum efficiency and turbine rotation rate changes in response to the measured wind speed. When the turbine approaches its rated power, the turbine efficiency is reduced as a function of wind speed and the rotation rate is controlled to yield the rated power of the turbine. When the wind speed increases to the point that the wind stress on the turbine blades becomes large enough to damage the machine, the turbine efficiency is reduced to zero and the turbine rotor is parked. Figure 7 shows the turbine control domains for a typical wind turbine.

There is an older class of small turbines that operate at a fixed rotation rate. These are not discussed in this report although the same modelling principles apply.

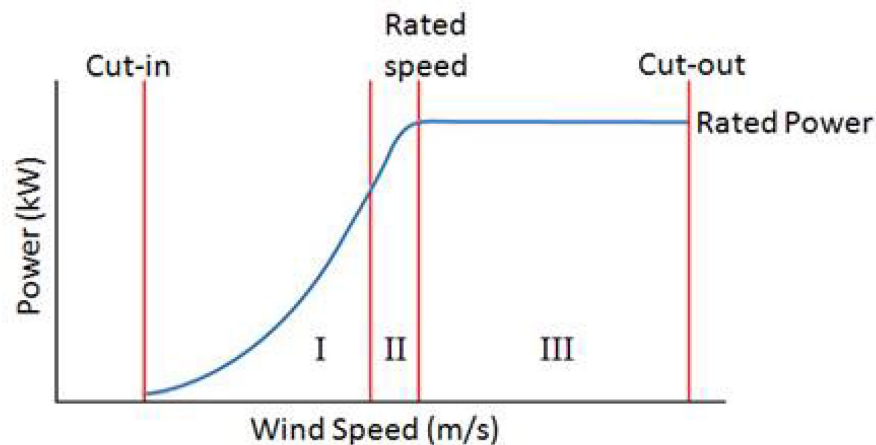


Figure 7: A typical wind turbine power curve.

Image credit: reference [8].

The turbine rotation rate at the rated wind speed is defined by the turbine model used. Typical rated-rotation rate values range from 11 revolutions per minute (RPM) to 22 RPM with the larger rotation rates corresponding to smaller rotor diameters.

2.3.1 Dynamic control, blade pitch

When the wind turbine is operating at its rated power, the shaft rotation speed is regulated by adjusting the airfoil angle of attack (Figure 8) over the length of the turbine blades and thus controlling the airfoil lift to drag ratio [3].

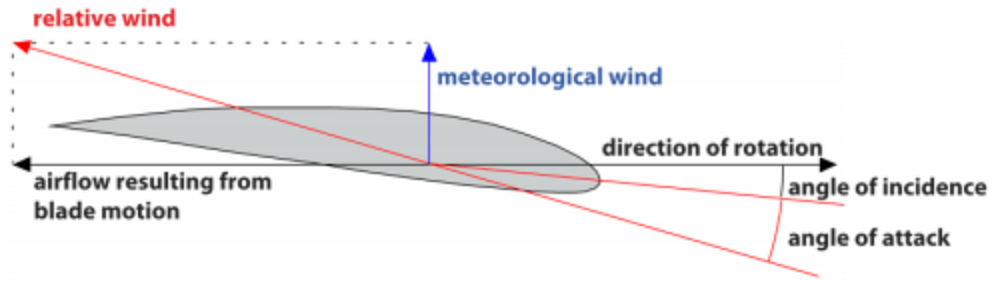


Figure 8: Wind turbine blade angle of attack.

Illustration credit: reference [3].

In Figure 8, the relative wind is the vector sum of the meteorological wind and the local velocity of the turbine blade. The blade twist compensates for the local blade velocity as a function of distance from the hub. The angle of incidence in Figure 8 is the angle between the rotation plane of the turbine and the local airfoil chord at radial distance D from the turbine hub. This angle is the sum of the blade twist and the controlled blade pitch angle and is used to control the airfoil angle of attack and thus the lift forces that drive the blade rotation. The component of the lift force vector in the direction of rotation powers the turbine.

As that angle of attack increases, the lift force increases until the airflow begins to separate from the airfoil skin due to cavitation effects (partial stall) as shown in Figure 9. At this point the lift begins to decrease, the drag increases and the airfoil efficiency decreases. Angle of attack control (blade pitch control) is used to decrease the turbine blade efficiency when the wind speed exceeds the rate wind speed of the turbine and thus regulate both the rotational speed of the turbine and the electrical power generated.

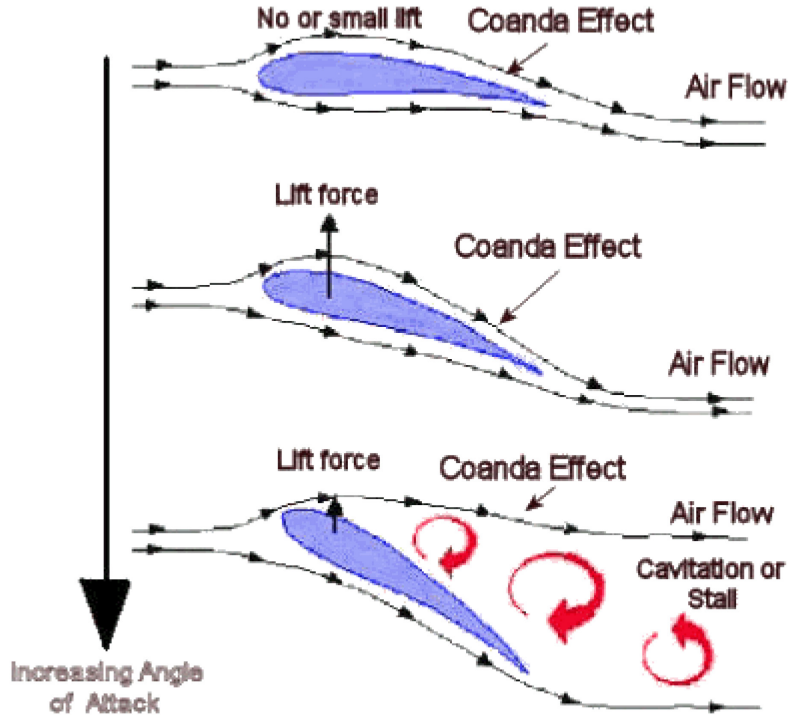


Figure 9: Schematic airfoil response to its angle of attack.

Illustration credit: http://www.formuladictionary.net/coanda_effect.

The wind turbine extracts mechanical power from the incident wind field as shown in equation (1). The wind energy extraction efficiency is contained in the parameter C_p which is a function of the normalized turbine blade tip-speed λ and the blade pitch angle β :

$$C_p(\lambda, \beta) = c_1 \left(\frac{c_2}{\lambda} - c_3\beta - c_4\beta^x - c_5 \right)^{\frac{c_6}{\lambda}} \quad (2)$$

where:

$$\frac{1}{\lambda} = \frac{1}{\lambda + 0.08\beta} - \frac{0.035}{1 + \beta^3} \quad (3)$$

and x , c_1 to c_6 are parameters that are specific to a turbine blade design. For low wind speeds, the pitch angle is set to 0 and C_p increases with increasing wind speed until the rated turbine power is approached. Once the turbine reaches its rated power, C_p is reduced by pitch angle increases until the cut-off wind speed is reached as shown in Figure 10 for a 70 m diameter turbine. In Figure 10, θ is the blade pitch angle and λ is the normalized blade tip speed.

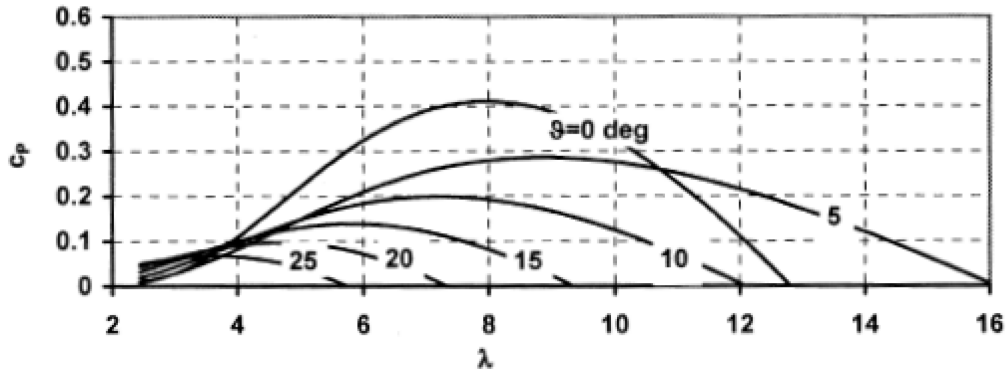


Figure 10: Analytical approximation of $C_p(\lambda, \beta)$ for blade pitch angle in degrees.

Illustration credit: reference [1].

When the cut-off wind speed is reached the turbine rotor is slowed and stopped (using stall effects in some cases), the rotor pitch angle is set to the feathered (no lift) pitch attitude and a brake is applied.

Table 2 shows the collective blade pitch angle for a 5 MW turbine with a 61.5 m blade when the turbine is operating within its rated power range [4].

Table 2: Wind speed vs. pitch angle relationship for a 5 MW turbine.

Wind Speed (m/s)	Rotor Speed (rpm)	Pitch Angle (°)	$\partial P / \partial \theta$ (watt/rad)
11.4 - Rated	12.1	0.00	-28.24E+6
12.0	12.1	3.83	-43.73E+6
13.0	12.1	6.60	-51.66E+6
14.0	12.1	9.70	-58.44E+6
15.0	12.1	10.45	-64.44E+6
16.0	12.1	12.06	-70.46E+6
17.0	12.1	13.54	-76.53E+6
18.0	12.1	14.92	-83.94E+6
19.0	12.1	16.23	-90.67E+6
20.0	12.1	17.47	-94.71E+6
21.0	12.1	18.70	-99.04E+6
22.0	12.1	19.94	-105.90E+6
23.0	12.1	21.18	-114.30E+6
24.0	12.1	22.35	-120.20E+6
25.0	12.1	23.47	-125.30E+6

Wind turbines are subject to boundary layer effects on wind speeds at all times. A typical vertical wind shear profile for a site in Colorado is shown in Figure 11 and would result in approximately 1.3 m/s wind speed differential between the upper and lower extremities of a 40 m diameter turbine that was mounted on a 60 m tall tower.

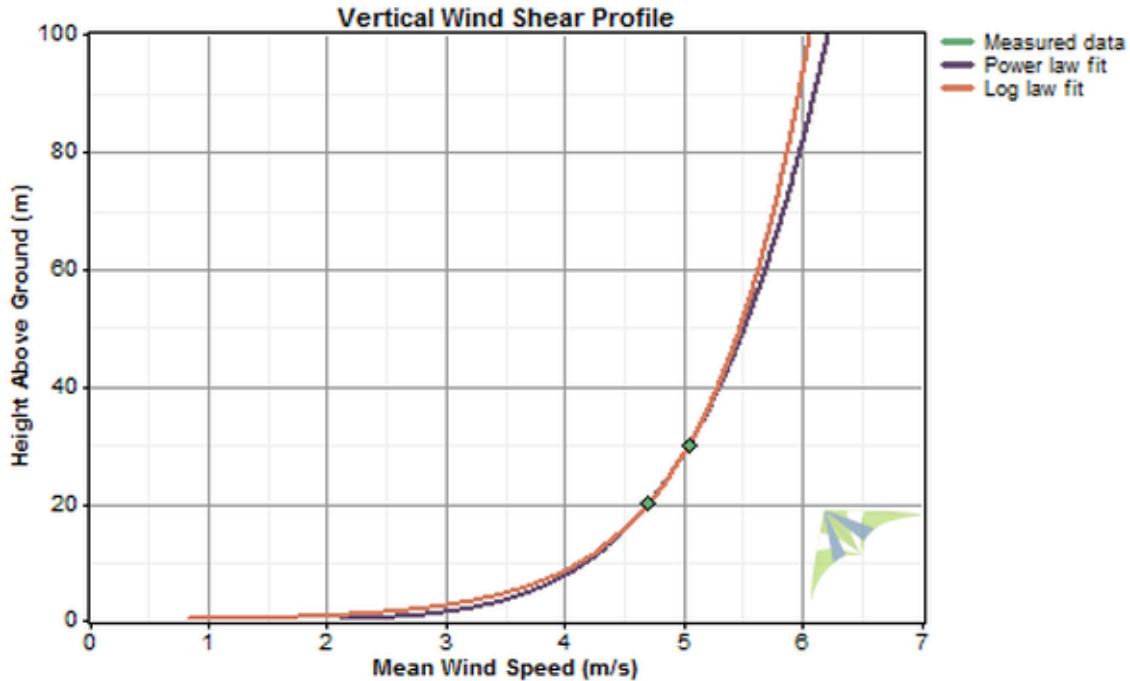


Figure 11: Vertical wind shear, height (m) vs. mean wind speed (m/s).

Illustration credit: http://projects-web.engr.colostate.edu/ALP/ALP_97_Waverly.

For this wind shear, a 40 m turbine blade would deliver approximately 40% less power traversing the lower half of its arc. Modern turbines compensate the vertical wind shear effect by independently controlling the pitch angle of each blade as it completes a full rotation about the turbine hub [11]. The pitch angle variation over one control cycle depends on the turbine design and the wind speed. For the model case reported in [11] the pitch angle spectrum has peaks at approximately 0.5 Hz and 2 Hz for a turbine rotation rate of 18 RPM.

In addition to the vertical wind shear, airflow around the tower influences the wind speed and direction. When the blade is under pitch control, the pitch angle is modulated by the angular position of each blade during one turbine rotation as shown in Figure 11 for a 2 MW, 63 m diameter turbine.

In Figure 12, the ideal response and system response for blade pitch angle θ is displayed for turbine rotation angle Ψ for one rotation of the turbine. The pitch angle modulation is a function for vertical wind shear and wind flow around the tower. The maximum variation of the dynamic rotation is approximately 6° for the case shown.

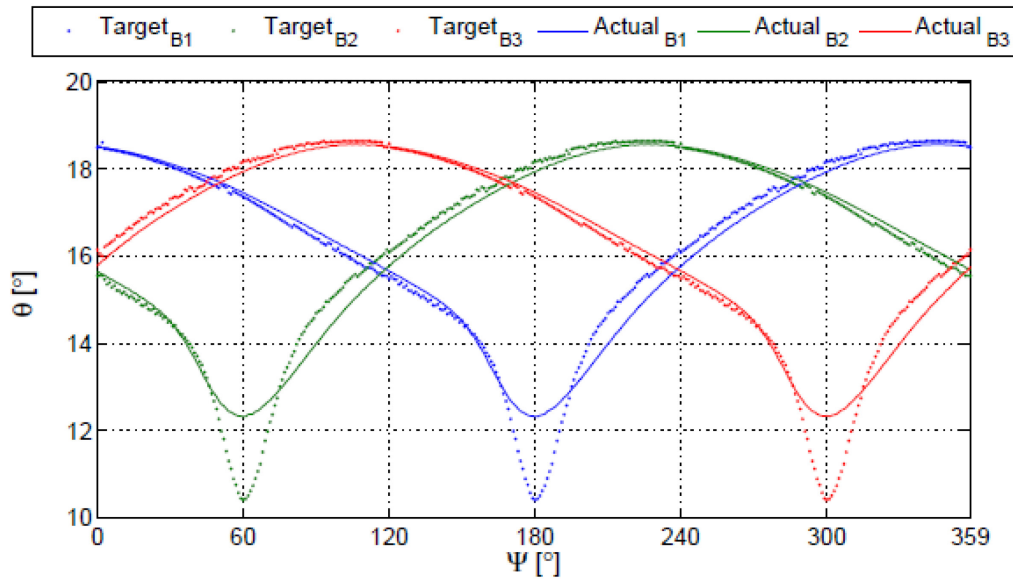


Figure 12: Wind turbine blade pitch angles over a full rotor rotation for independently controlled blades.

Illustration credit: reference [11].

2.3.2 Dynamic control, turbine yaw

To minimize wind turbulence effects due to the turbine tower and the generator nacelle most wind turbines are operated with the blades turned to the windward side of the tower. The turbine efficiency is maximized by aligning the turbine rotor shaft towards the up-wind direction (yaw angle = 0) using wind direction sensors mounted at the aft end of the nacelle. Because of the location of these sensors, they are affected by the turbine rotation and require careful calibration.

The combination of wind sensor measurement accuracy and the yaw drive servo yields pointing accuracies of approximately $\pm 10^\circ$ when the wind is steady. The turbine yaw-control drives are activated when the time-integrated wind direction deviates from the turbine yaw angle by a pre-defined pointing accuracy error tolerance and the turbine yaw axis is stabilized by brakes between corrections. Yaw slew rates for large turbines are in the vicinity of $0.3^\circ/\text{s}$ and wind directions estimates are averaged over many seconds to determine when yaw angle adjustments are required.

When the local wind speed exceeds the maximum rating of a turbine, the yaw control is used to turn the rotor so that the blade plane is 90° to the wind direction to minimize wind loading effects on the parked, stationary turbine.

Standard design practice uses a cable that has fixed ends to carry power generated by the turbine down the tower to the ground. There are no slip-ring joints and the cable is designed to twist as the nacelle rotates in azimuth. When the twist accumulates to a design limit, the nacelle is rotated in yaw to return it to a neutral position. For large, high power turbines, typical rotation rates are in

the vicinity of $0.3^\circ/\text{s}$ during this action. The turbine rotor is locked in the feathered state during yaw adjustment to the neutral cable twist condition.

3 Radar observations of wind turbines

3.1 Wind turbines as radar targets

Considering a wind turbine as a radar target, there are three major contributors to radar returns seen by ground-based radar:

- the turbine tower,
- the nacelle, and
- the turbine hub and blade assembly.

The tower is a nearly stationary target that has a limited sway motion component and a very narrow Doppler spectrum. Model calculations for plane wave incidence on a 60 m high tower [12] result in radar cross sections in the vicinity of 35 dBm² for radar frequencies between 400 MHz and 5000 MHz.

The nacelle moves in response to sway motion at the top of the tower and executes yaw rotation steps in response to wind direction measurements. Both motions are slow and have narrow Doppler spectra. When the flat-sided nacelle is broadside to the radar, plane-wave incident model calculations [12] yield radar cross sections decreasing from 47 dBm² to 39 dBm² as the radar frequency drops from 5000 MHz to 400 MHz.

The turbine blade assembly rotates in a plane that is normal (to within yaw control error) to the wind direction vector while the turbine is active. At wind speeds below the turbine cut in speed, the turbine axis is adjusted to be parallel to the wind direction. At wind speeds above the turbine cut-out limit, the turbine plane is oriented to be parallel to the wind vector to minimize wind loading effects of the mechanical structure and the rotor is parked.

Each turbine blade has a fixed twist from blade root to blade tip as shown in Figure 6 and Table 1 which will cause some systematic variation in radar cross section along the blade. When the turbine is operating at its rated power, the blades are rotated in pitch (about the longitudinal axis of the blade root) in response to wind speed as shown in Figure 10 and Table 2. In addition, modern wind turbines independently control the blade pitch angles in response to the blade's azimuth rotation angle in its operating plane as shown in Figure 12 to compensate for vertical wind shear and tower flow effects.

The blade pitch rotation will dynamically influence the radar cross section of the blade along its length.

Model calculations for the Enercon E66 1.8 MW turbine blades and hub [12] (without the tower and nacelle) are shown in Figure 13 to display two scattering model cases for 1.3 GHz radar illumination at the 90° polar angle in the diagram. The model calculations correspond to the blade disk being illuminated from one edge so that the rotor plane is normal to the radar illumination vector. The radar wave-front is assumed to be planar at the turbine. The scattering patterns shown are in the vertical plane.

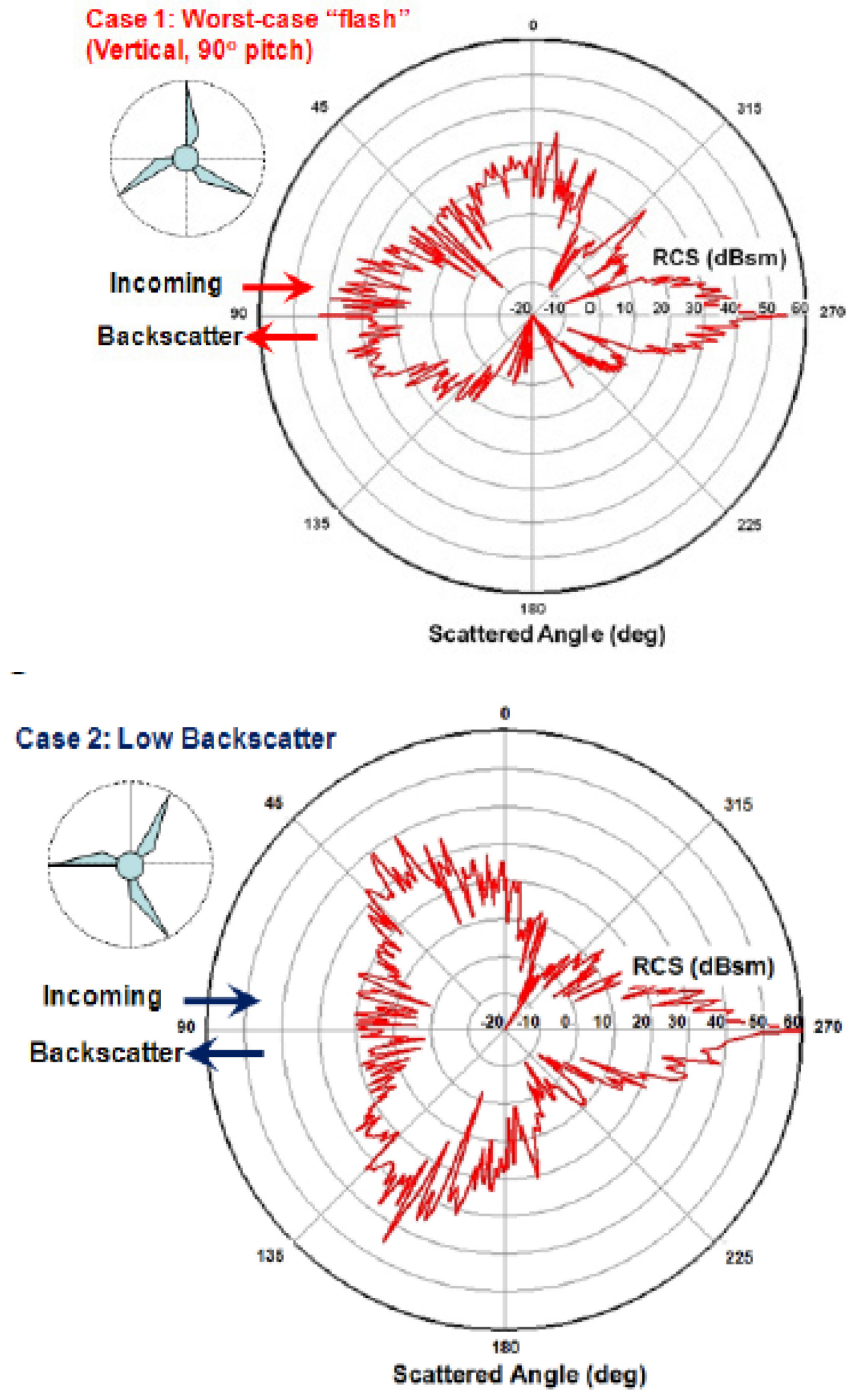


Figure 13: Radar scattering model calculations for fiberglass turbine blades at 3 GHz radar frequency.

Illustration credit: reference [12].

The corresponding 3 GHz radar reflection coefficients for the fiberglass used to model the results shown in Figure 13 are shown in Figure 14 as a function of local incidence angle on the blade for various shell thicknesses.

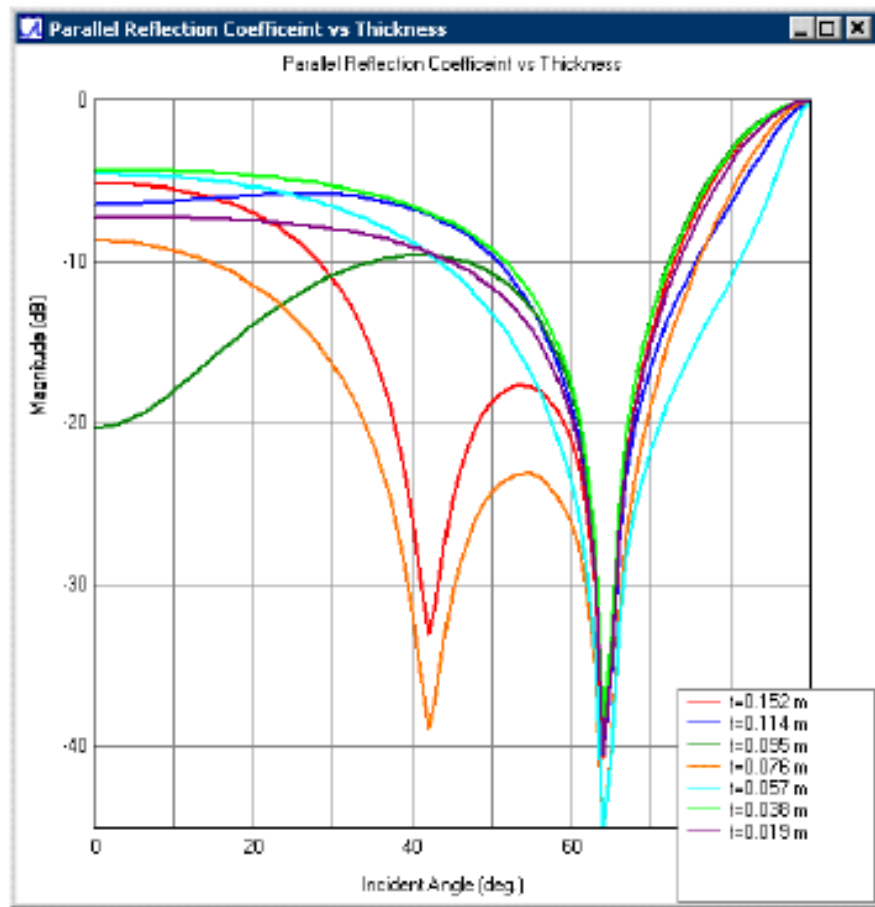


Figure 14: Radar reflection coefficients for various shell thicknesses as a function of local incidence angle.

Illustration credit: reference [12].

Figure 13 demonstrates a complex scattering pattern that has bistatic scattering peaks that depend on the blade angles. The back-scattering results for case 1 show the blade flash effect, reported by many authors, to be a single peak at approximately 42 dBm² with companion peaks between 36 and 40 dBm² that are distributed over approximately 5° of rotation angle. As expected, minimum radar returns are observed when one blade is pointed at the radar (case 2) and the peaks of these returns are at approximately 20 dBm² for the modelled blades and are clustered over approximately 70° of rotation angle. The results suggest that the peak observed radar cross section varies by approximately 12 dB with peaks observed every 120° of rotation. For both case 1 and case 2 in Figure 12 the forward scatter peaks can approach 60 dBm² independent of the rotor angle. The forward scattered signals play a large role in wind-farm multi-path scattering.

Figure 15 shows the model ray tracing results [12] in terms of the correlation between the measured RCS and the Doppler frequency of the radar returns when the Case 1 blade is rotating towards the radar at 16 RPM (revolutions per minute).

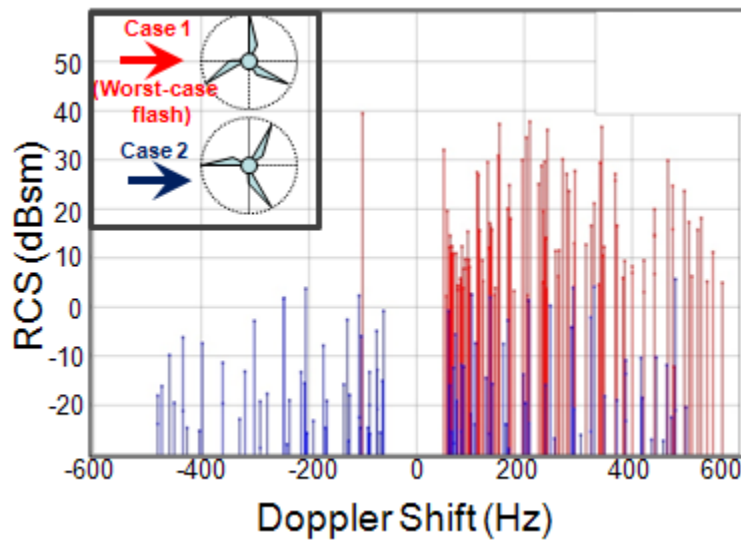


Figure 15: Model results for the relationship between the radar Doppler shift in Hz and the RCS in dBm^2 when the blade root components are suppressed.

Illustration credit: reference [12].

The scattering model used to generate Figures 13 and 15 treated the turbine blades as hollow shells that had an external blade shape extracted from a CAD (computer aided design) representation provided by the blade manufacturer. The shell thickness was varied over the blade length and the material reflection coefficients given by Figure 14 were used to perform the ray tracing calculations. The internal structure of the blades was not included in the calculations.

The internal spar structure of the blades was not modelled in [12] but anechoic chamber measurements made by ONERA [13] shown in Figure 16 suggests that the internal spar structure plays a role in the blade's radar signature when the blade is observed with its trailing edge (and possibly leading edge) pointed towards the radar. The red arrows in Figure 16 show the radar illumination direction. No other data of this type have been found.

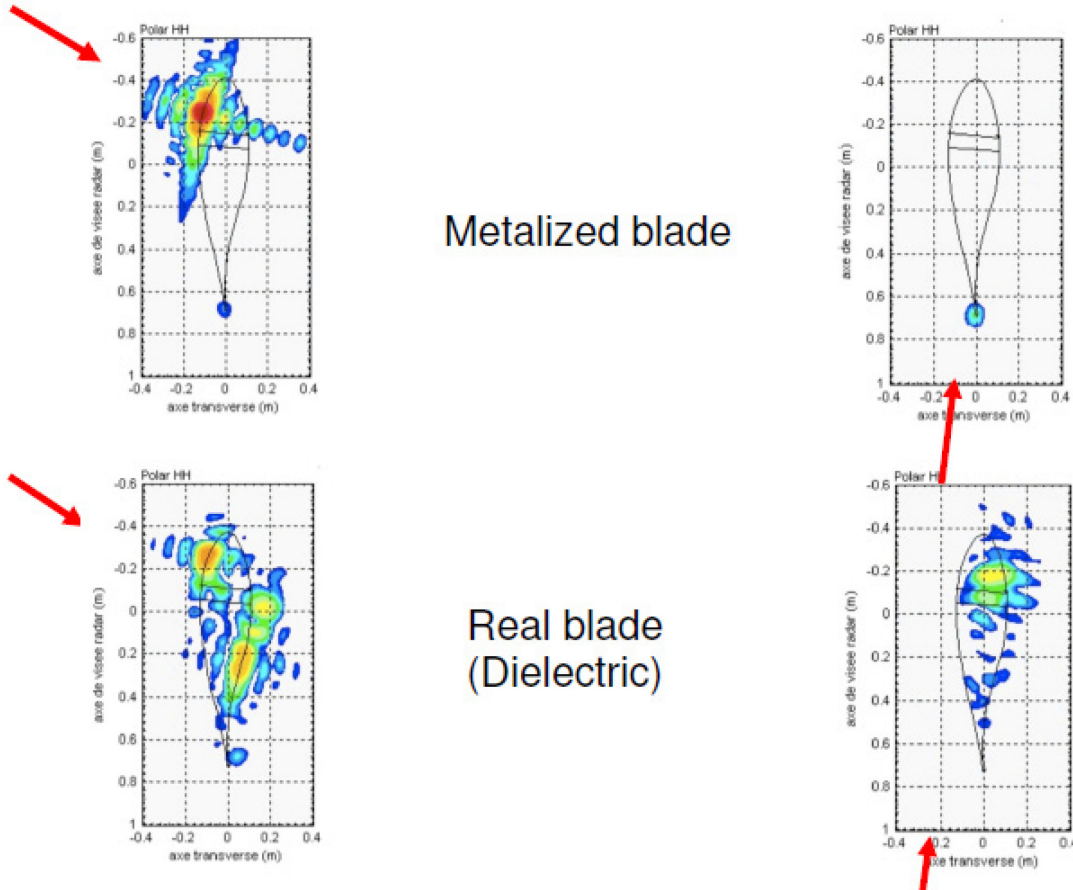


Figure 16: Anechoic chamber measurements of a model section of a turbine blade.

Illustration credit: reference [13].

In a 2002 study for the UK Department of Trade and Industry, a research team from QinetiQ used 3.05 GHz radar to observe the Enercon E66 turbine at Swaffham UK [14]. Since the radar viewed the turbine at a range of 3.45 km and the plane wave approximation used for the model calculation results shown in Figures 12 and 14 was not met. The site photograph provided in [14] suggests that the radar antennas were approximately at the turbine hub height.

Observations of the turbine rotor plane edge are shown in Figure 17 for 1.15 rotations when the rotor was operating at its rated speed of 23 RPM. The radar measurements include the turbine tower and the turbine nacelle. Model calculations suggest that six RCS peaks should be observed over one turbine rotation. Figure 17 shows nine peaks over this same period. In Figure 17, the peaks at 0.21 s, 1.1 s and 2 s correspond to one blade pointed vertically down with its leading edge moving towards the radar. The peaks at 0.65 s, 1.6 s and 2.45 s correspond to one blade pointed vertically up with its trailing edge moving away from the radar. The third set of peaks at 0.38 s, 1.35 s and 2.18 s are interpreted by the author of [14] to be a multi-path effect that represents scattering between blades. This interpretation is supported by the Doppler spectrum results shown in Figure 18. The measurements shown in Figure 17 exhibit significant coherent

fading for all blade rotation angles and the width of the approaching blade peaks corresponds to approximately 3° of rotor rotation which is comparable to the model results in Figure 13.

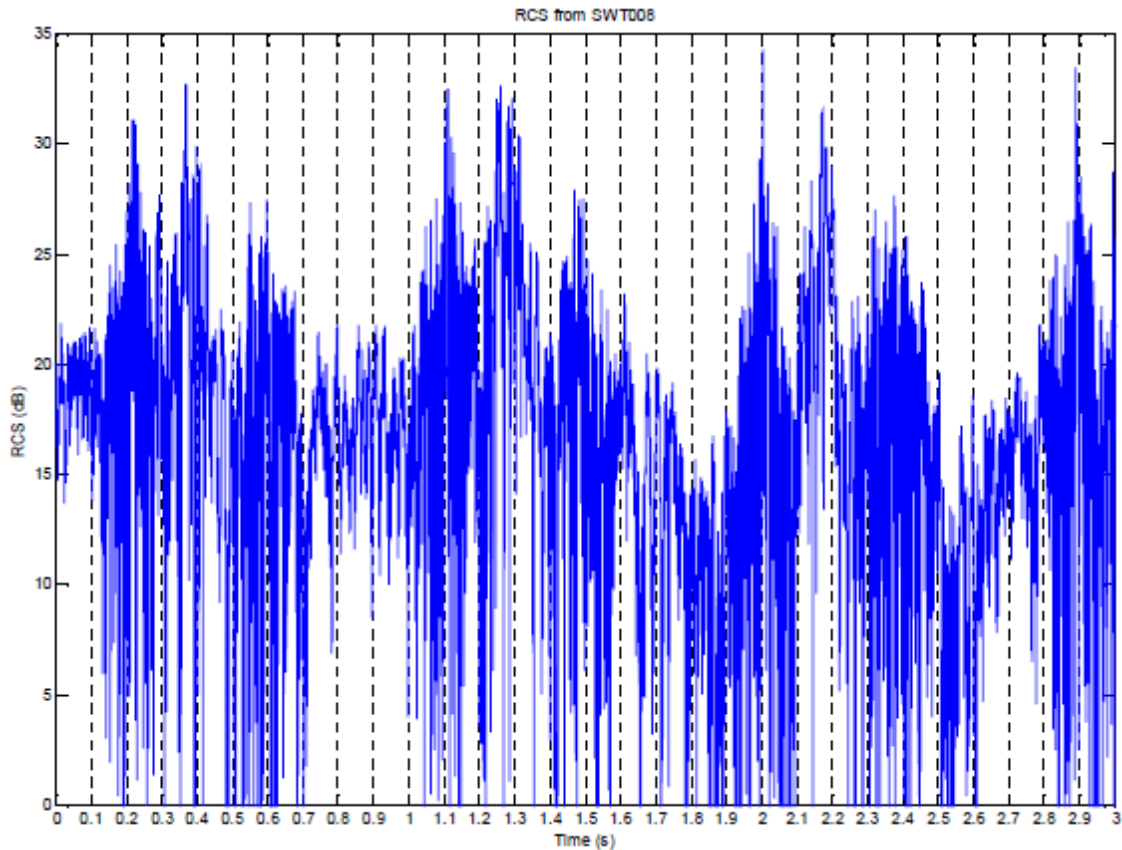


Figure 17: 3 GHz radar cross section for an Enercon E66 wind turbine viewed at 90° to the turbine shaft axis at 23 RPM rotation rate [14] as derived from the radar video output.

Illustration credit: reference [14].

When the leading edge blade peaks are compared to the trailing edge blade peaks in Figure 16, the trailing edge cross sections are approximately 6 dB smaller.

Examining the frequency-time description of the radar signature in Figure 18, the negative frequency peaks in the vicinity of 0.38 s, 1.35 s and 2.18 s have a small Doppler range (<300 Hz) and suggest that the multi-path peaks in Figure 17 are concentrated near the blade roots. Figure 18 also suggests that the spectral response of the blades passing the tower contains components with Doppler shifts larger than those from the blades that are vertically up and the difference between the two cases is approximately 300 Hz. For the measurements reported in [14] some of the imbalance between the Doppler shift maxima for the approaching and receding blades may be due to multi-path scattering between the blade and the tower and between the blade and the ground surface.

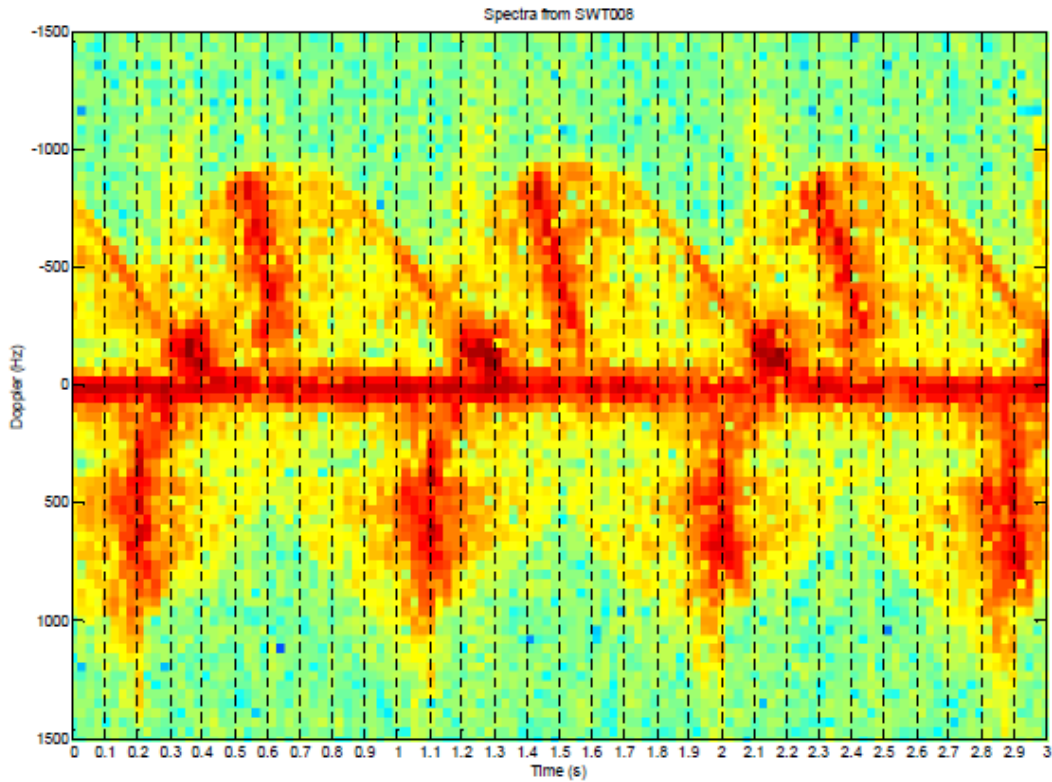


Figure 18: Time frequency display of the Doppler returns from the Enercon E 66 wind turbine at Swaffham UK for the data displayed as RCS in Figure 17.

Illustration credit: reference [14].

Received signal Doppler spectra from the Enercon turbine are reported in [14] for two yaw angle cases:

yaw = 90° (the rotor is viewed from its edge) and yaw = -10° (the rotor is viewed at -10° from its plane).

Figure 19 displays the received signal spectrum for one turbine rotation when the rotor disk axis is -10° from the radar range vector and the rotor is turning at 12.4 RPM. Figure 19 displays the received signal spectrum when the rotor disk edge is viewed by the radar, the disk axis is 90° to the radar range vector and the rotor is turning at 12.5 RPM.

The zero Doppler spike shown in Figures 19 and 20 displays the radar returns from the turbine tower and nacelle and is nearly independent of yaw angle (the tower signature is dominant for the Enercon nacelle design) and is approximately 24 dB larger than the radar returns from the rotating components. When the disk plane is observed by the radar (Figure 19) there are two Doppler peaks near ± 150 Hz that represent the -10° projection of the disk rotation. The rest of the spectrum may be multi-path components of the disk scattering. When the rotor disk is viewed at yaw angle 90° (Figure 20) the rotor hub and blade roots appear as a spectral peak bounded by \pm

100 Hz. The blade that is receding from the radar past the tower (trailing edge visible to the radar) shows a nearly level spectral response with mean near -32 dB and then decays in spectral amplitude as expected by the model calculations shown in red.

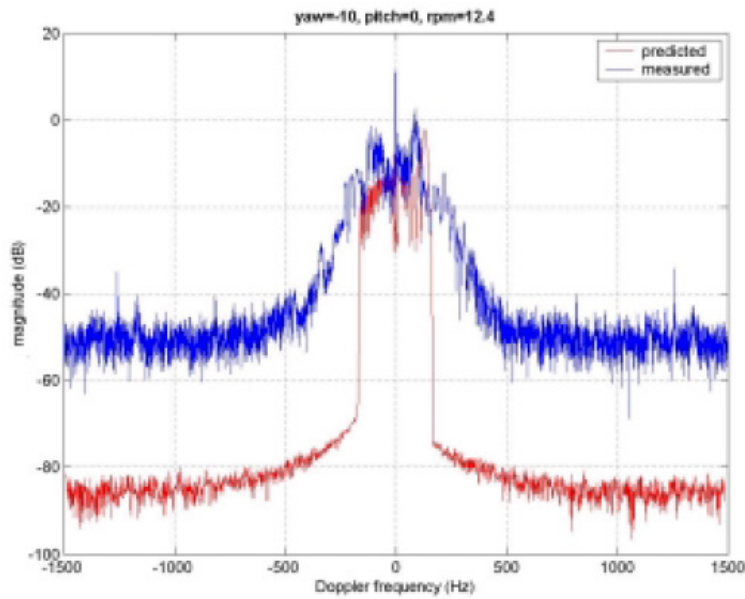


Figure 19: Enercon E66 turbine Doppler spectrum for radar observation of the rotor disk plane at -10° yaw angle.

Illustration credit: reference [14].

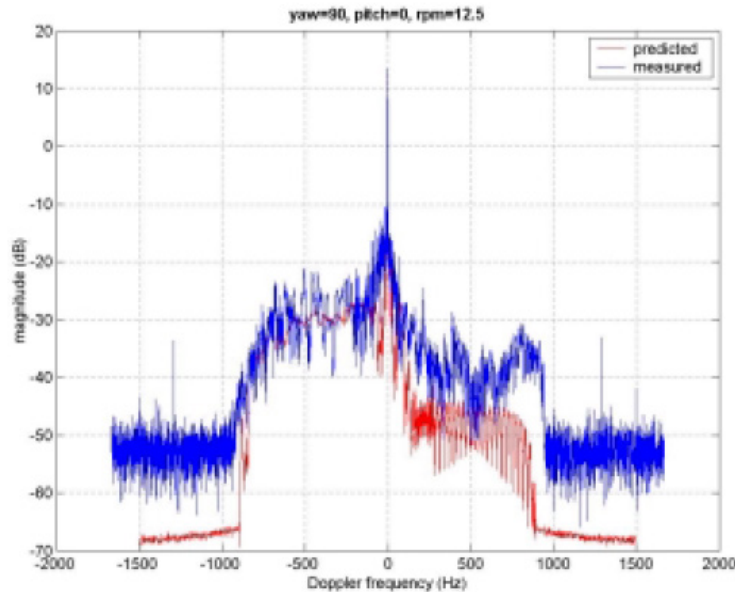


Figure 20: Enercon E66 turbine Doppler spectrum for radar observations of the rotor disk edge.

Illustration credit: reference [14].

The blade that is approaching the radar (leading edge visible) shows a more complex spectral amplitude behavior that does not match the model calculations as well. The peak radar returns from an approaching blade (leading edge viewed by the radar) show relative maxima at the blade root, near the blade center and near the blade tip. These maxima are approximately 8 dB lower than maximum returns from a receding blade.

Discussions in [15] also consider the radar cross section of flat-sided wind turbine nacelles such as those used by the Vestas wind turbines. The rectangular nacelles have peak radar cross sections that exceed 40 dBm² (more than 20 dB greater than the rounded Enercon nacelle return) and can dominate the static component of the turbine return when the rotor edge is viewed by the radar.

Studies of blade pitch angle effects in [14] show that the blade pitch angle for a vertical blade has little effect on the blade RCS when the radar views the turbine rotor plane from the edge but shifts RCS peaks that occur for radar observation angles within $\pm 30^\circ$ of the turbine axis by the applied pitch angle.

When the radar observes the turbine disk at 0° yaw (parallel to the turbine rotation axis) model calculations, Figures 21 and 22, show the relationship between the turbine blade orientation and the peak expected RCS [14] to vary approximately 12 dB over a partial turbine rotation. From Figures 21 and 22, it is seen that the radar cross section has a large scale periodic modulation of fine structured scattering effects that repeats three times per revolution and that the largest radar cross section occurs when a turbine blade passes the mounting tower. For yaw = 0° the Doppler spectrum of the wind turbine will be similar to that shown in Figure 19 without the Doppler lobes that are caused by the projected blade motion.

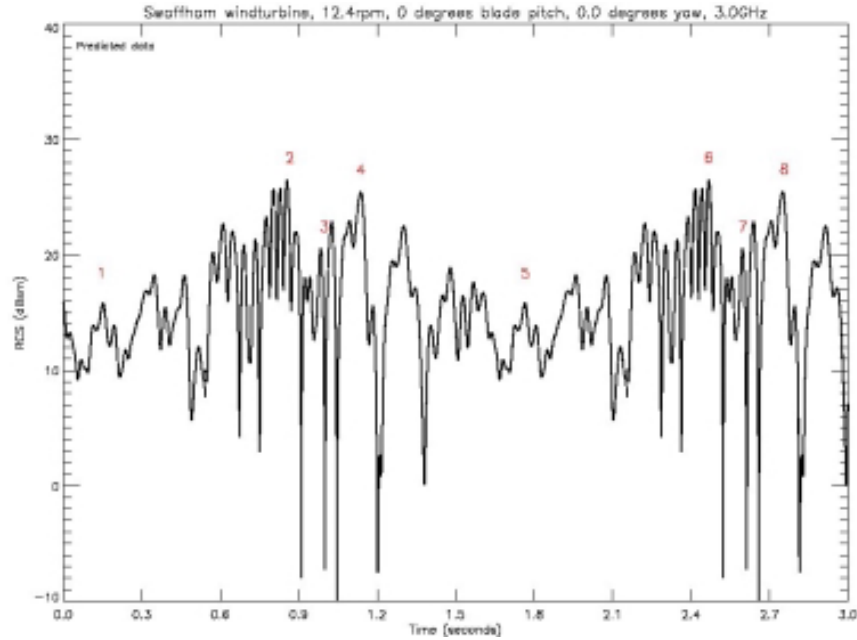


Figure 21: Modeled radar cross section of an Enercon E66 turbine at 0° yaw angle.

Illustration credit: reference [14].

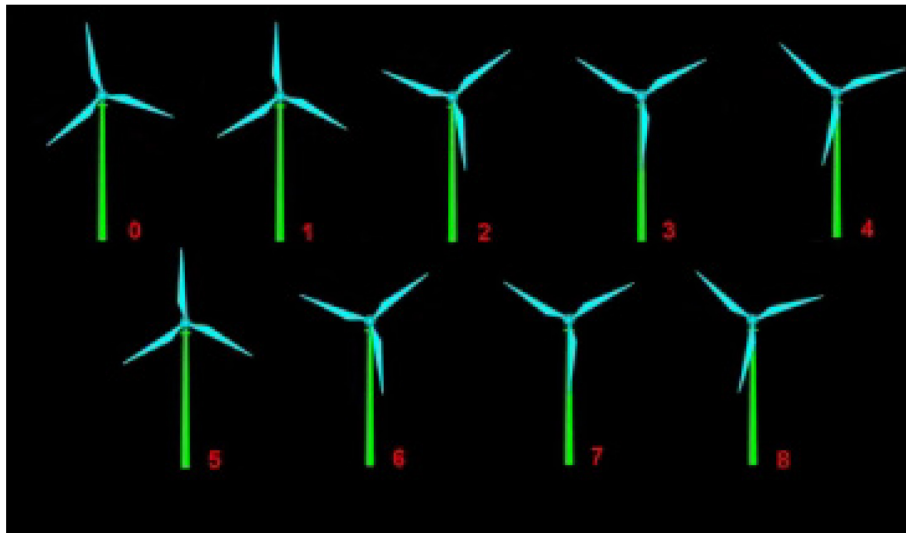


Figure 22: Turbine blade locations for figure 20.

Illustration credit: reference [14].

Figure 23 combines the model calculations shown in Figure 21 with measurements of an Enercon E66 turbine at 0° yaw. Although the model calculates the gross features of the turbine RCS, measurement results show much finer coherent fading results and peak RCS values that are approximately 5 dB larger than the model predictions. As was noted previously, blade pitch control will act to shift the positions of the RCS peaks in the 0° yaw case.

Noting that the turbine will be contained within a single radar resolution cell that spans hundreds of radar wavelengths and noting that all radar returns add coherently at the radar to define the radar signal. The fine fading effects seen in Figure 23 are expected for all radar frequencies of interest.

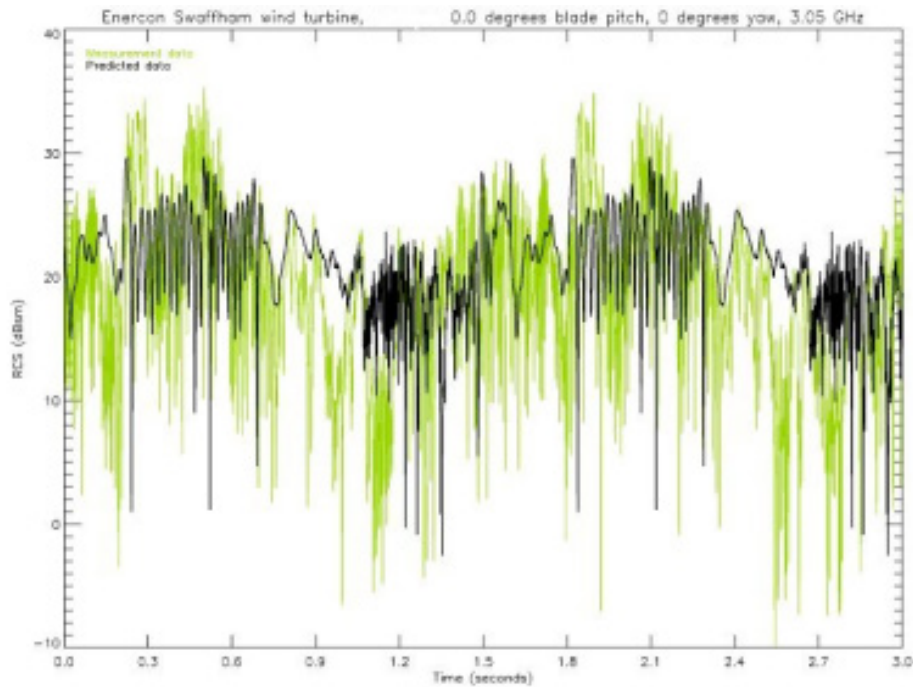


Figure 23: 3.05 GHz measurements of an Enercon E66 turbine at 0° yaw angle.

Illustration credit: reference [14].

A Doppler frequency time plot for one full turbine rotation is shown in Figure 24 for the case where the radar range vector is aligned with the turbine axis. A comparison with Figure 18 shows that the spectral frequency peaks are reduced approximately a factor of 5 when the turbine axis is rotated 90° to align with the radar range vector.

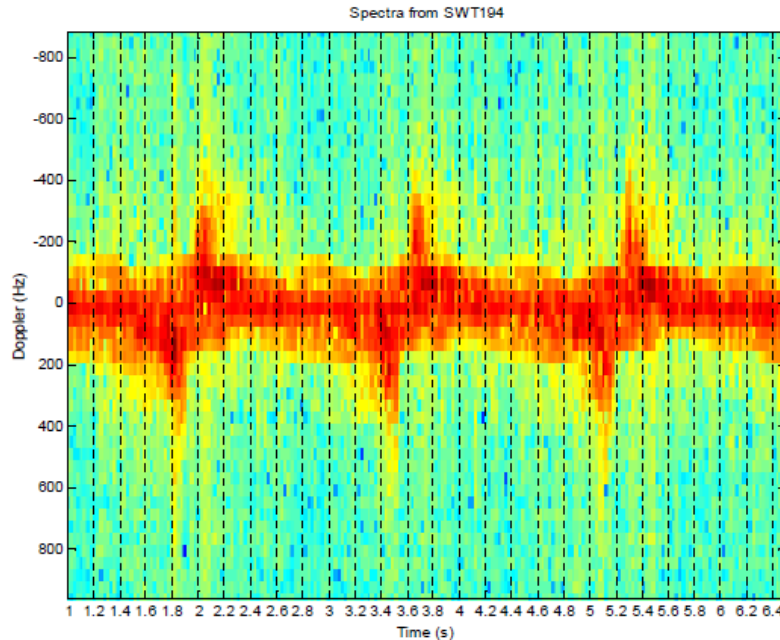


Figure 24: Doppler spectrum-time plot measured for an Enercon E66 turbine at 0° yaw.

Illustration credit: reference [14].

An Enercon E66 (66 m diameter rotor with a 67 m tower) turbine has formed the basis of the RCS measurements discussion in this section. Although the turbine blade structure is expected to alter the details of the turbine RCS, the major features of the data presented in this note should be replicable from turbine to turbine and results should be approximately scalable by turbine rotor diameter.

Comments in [14] indicate that fiberglass turbine blades should have approximately 3 dB smaller RCS than equivalent metal blades. Radar scattering based on CAD shape data for the turbine blades should be usable (if somewhat conservative) in most cases to model the expected wind tunnel interference with air traffic control radars.

3.2 Air traffic and weather radar observations of wind turbines

3.2.1 ASR primary surveillance radars

Airport primary surveillance radars (ASRs) typically operate at S-band (2.7 GHz to 2.9 GHz) or L band (1.25 GHz to 1.35 GHz). They are designed to monitor the position and radial speed of aircraft within 80 nautical miles (148 km) of the radar position and to track these targets. These radars often use two simultaneous beams, to provide data on both distant and closely approaching aircraft. Distant aircraft are monitored by a low, pencil beam with nominal 1.2° to 1.5° azimuth beam width that is oriented so that the -3 dB beam edge scans the selected radar horizon. Closely approaching aircraft are monitored by a high beam that has a cosecant² weighting in elevation that provides range compensated radar signatures up to 50° elevation angle and has an azimuth beam

width between 1.2° and 1.5°. Both beams capture ground clutter signals. ASR antennas do not contain multiple phase centers to measure the elevation angle of arrival of the received signals and are paired with a secondary surveillance radar (a transponder query system that receives aircraft flight parameters from cooperating aircraft). ASRs are range-Doppler radars that use signal processing to suppress stationary ground clutter contamination in the received radar signals. Many primary surveillance radars use offset carrier channels to transmit different waveforms to minimize false alarms and to enhance small target detection. The airport primary surveillance radars also contain processing channels to extract meteorological data.

ASRs use mechanically scanned antennas whose rotation rates typically vary between 12 and 15 RPM in normal use. Pulse repetition frequencies range between 700 Hz and 2000 Hz. The average transmitter power ranges from approximately 25 kW to 50 kW. Range resolutions are typically between 130 m and 210 m although some radars have a higher resolution (50 m mode) for aircraft tracking. Target Doppler estimates are usually determined by analyzing the phase history of 8 to 12 pulses in a coherent burst of received signals.

Most of the currently active ASR systems have been in service for many years and some date back to the mid-1970s. ASR technology has improved continuously with the result that newer systems are more capable than the older ones. Some of the older US *en route* monitoring radars were updated in the early 1990s [16] to extend their useful life and to upgrade their performance. Some of these same capabilities have been incorporated into heritage ASRs in the early 1990s.

Upgraded, heritage ASRs have not been designed to fully mitigate wind turbine clutter properties. At issue are signal amplitude dependent CFAR (constant false alarm rate) detectors, STC (sensitivity-time-control) algorithms and processing capabilities for dealing with and recognizing wind turbine signatures to eliminate these from tracking algorithms. Since many older radars do not have sufficient dynamic range to accommodate wind turbine clutter, radar gain control variations along wind-turbine range vectors can reduce ASR radar sensitivity to air targets along these vectors and Doppler processing in some older radars will identify wind turbine signals as air targets.

More modern ASR designs [17] can significantly mitigate wind turbine effects on estimating small aircraft tracks but few of these are currently in service.

3.2.2 ASR observations of wind turbines

Wind turbines are typically more than 10 km from active air traffic control and meteorological radar sites to minimize turbine blade effects on radar observations and land-based turbines are typically placed on level, unobstructed terrain or on elevated terrain to minimize wind shadow effects. Typically ASR antennas are mounted on towers with heights up to ~30 m to clear nearby terrain obstructions. For a smooth, bald earth (ocean surface) and a radar antenna height of 30 m above this surface, the radar horizon is 19.5 km from the radar and a turbine hub (mounted on a 100 m tower) is at the radar horizon when the tower is 55 km from the radar. The visibility of land based turbines depends on the terrain elevation and terrain cover specifics at a site and is site dependent.

Several factors determine the radar returns from a wind turbine.

1. The yaw angle of the turbine rotor is determined by estimates of the local wind direction at the turbine site to within the wind direction measurement accuracy (typically $\pm 10^\circ$). The width of the Doppler spectrum of the turbine rotor varies approximately as the sine of the angle between the turbine axis and the radar range vector (the radar observation angle). Figure 24 shows that there are residual Doppler flashes when the two axes are aligned. In addition, the radar return from the turbine nacelle is a zero Doppler signal that varies in magnitude with the radar observation angle. For rounded nacelle designs, the maximum nacelle RCS is similar to the tower RCS and its rotation has little effect on the RCS of the static radar return from the turbine as is shown in Figure 25.

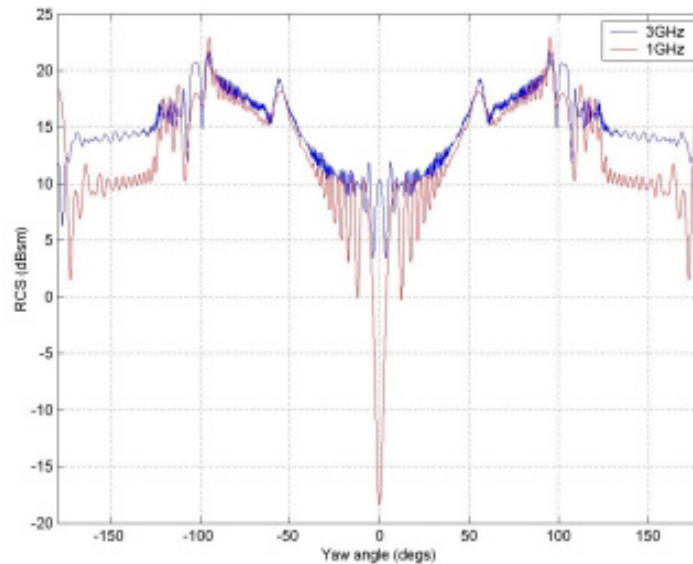


Figure 25: Enercon E66 nacelle RCS from model calculations.

Illustration credit: reference [14].

For flat sided nacelle designs, the nacelle RCS can exceed the tower RCS by up to 20 dB at 90° radar observation angle as is shown in Figure 26 and can have a large effect on the static RCS component over an approximately 5° observation angle interval.

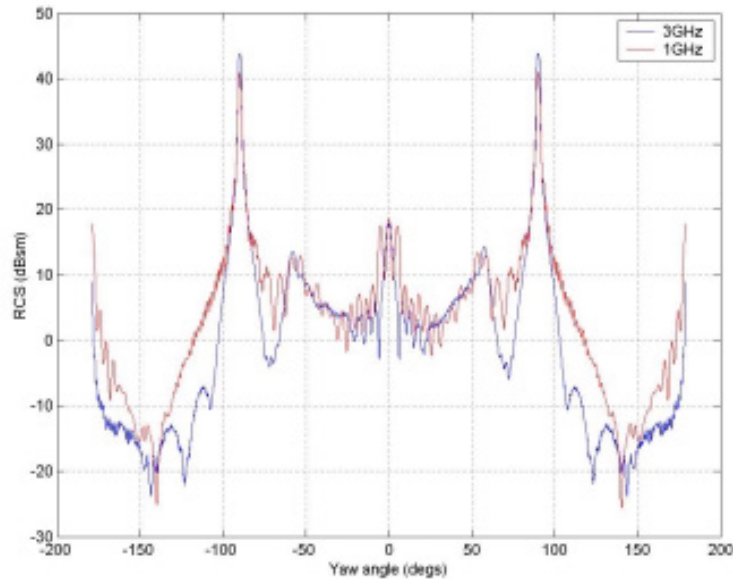


Figure 26: Vestas V47 nacelle RCS from model calculations.

Illustration credit: reference [14].

2. The turbine rotation rate increases with wind speed from the cut-in wind speed to the rated wind speed. For wind speeds above the rated wind speed and below the shut-down wind speed, the turbine rotates at a nearly constant rate that is determined by the turbine design. When the wind speed is greater than the turbine shut down speed, the turbine is parked with its rotor disk aligned with the wind and becomes a totally static target.

When the turbine is rotating, the RCS of the turbine disk varies from a sinusoidal envelope of structured returns (Figure 21) whose dominant frequency is three times the turbine rotation rate when the turbine is viewed along its rotation axis; to a sequence of six equally spaced spikes (flashes) that are associated with a broad Doppler spectrum (Figure 18) when the disk is viewed at 90° to its rotation axis. The special case shown in Figure 17 contains a set of dihedral RCS spikes that are associated with a reduced Doppler spectrum. These are observable over a limited range of geometries for some radar systems and probably for some turbine blade designs.

For the yaw = 0 data in Figures 21 and 23, the RCS modulation depth is approximately 12 dB when fading effects are smoothed. For the yaw = 90° data, The RCS modulation depth is also approximately 12 dB. The peak RCS is comparable for the two cases [15].

3. For all radar observation angles the ASR scan rotates at a constant angular speed that depends on the radar design. Typical ASR scan rates vary from 12 RPM to 15 RPM and typical azimuth beam widths vary from 1.2° to 1.4° . A wind turbine whose rotor diameter is 66 m, observed by a radar at 30 km range subtends an angle of 0.01° and can be considered as a point when estimating the radar antenna gain for the turbine target. A typical ASR azimuth antenna gain is shown in Figure 27 for an S band antenna with a 1.4° beam width [17].

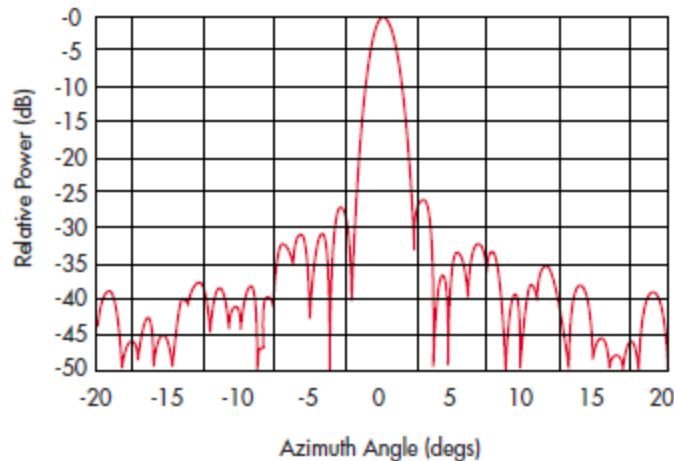


Figure 27: S-band air traffic control radar azimuth pattern.

Illustration credit: reference [17].

Using the Enercon E66 data, the peak return from the wind turbine is 32 dBm^2 and noting that many ASRs are designed to locate and track aircraft whose cross sections are as small as 2 dBm^2 , the peak return from a wind turbine can equal or exceed a small aircraft return for up to 12 degrees of radar rotation. The radar observes the turbine for up to 0.17 seconds (170 pulses at 1000 Hz radar PRF). This includes the first side lobes on each side of the beam. If the turbine is viewed edge-on, the turbine cross section can change by $\sim 10 \text{ dB}$ over the same time interval (Figure 16), thus considerably shortening the peak observation time where the turbine return exceeds the small target return as seen by the radar. This is the spectral ‘flash’ effect.

When the turbine is viewed face-on the peak turbine cross section (Figure 23) can vary approximately 6 dB over the observation time. There will be three maxima per turbine rotation.

The turbine rotation rate varies with local wind speed and is totally asynchronous with the ASR scan rate. The turbine tower, hub, nacelle and blade root will be observed as stationary and low-bandwidth moving targets on every ASR scan (Figures 19 and 20). Observations of the bulk of the turbine blade length will vary in frequency depending on the turbine rotation rate, the ASR scan rate and the angle between the turbine axis (wind direction dependent) and the radar beam.

From Figures 17 and 23, coherent fading effects will modulate the radar returns and may be visible within short groups of radar pulses.

4. A critical radar parameter that will determine the impact of the wind turbine on the radar sensitivity is the instantaneous dynamic range of the radar receiver. This will be primarily determined by the instantaneous dynamic range of the radar which is in turn determined by the linearity of the radar electronics and the digitizer that captures the radar signal (a

12 bit digitizer has a linear dynamic range of 72 dB). Most ASRs use CFAR algorithms to control the moving target detection thresholds used for aircraft detection. The CFAR algorithm is usually applied to radar returns following a zero-Doppler notch filter in the radar receiver output and is not usually affected by the static returns from the turbine assembly. For heritage radars, wind turbine returns can result in a radar gain reduction in the wind turbine range bin and can compromise the detection of other targets.

5. Distant, land based wind turbines can be partially obscured by terrain and by intervening vegetation. Depending on the fraction of the turbine rotor that is obscured, an integral of the spectral energy described by Figures 19 and 20 can be used to estimate the expected reduction in turbine cross section. Where the turbine tower and hub are both obscured, Figure 20 suggests that the radar cross section of the blades decreases along the blade length. The ISAR (Inverse Synthetic Aperture Radar) spotlight image shown in Figure 28 and the range-Doppler image shown in Figure 29 [18] confirms that the blade root and the rotor hub are major contributors to the radar cross section of the rotor as was inferred from Figures 19 and 20.

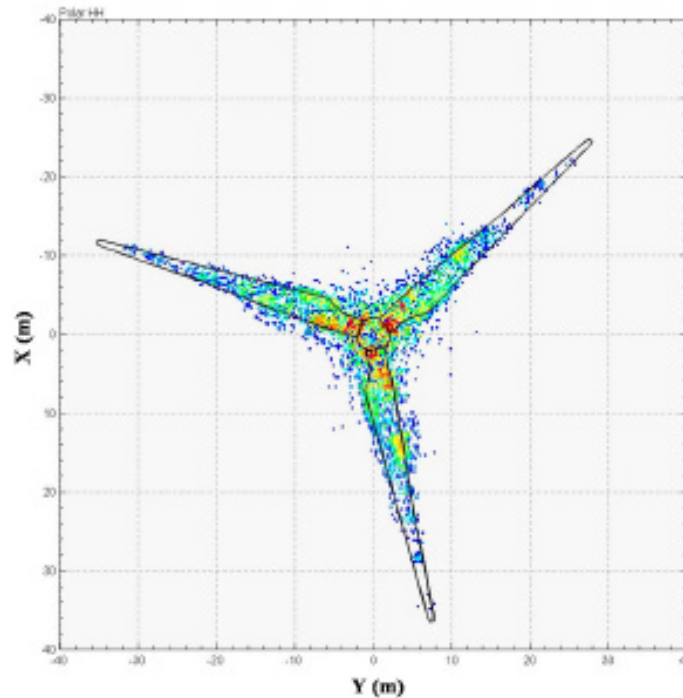


Figure 28: ISAR spotlight image of a REpower MM82 82 m wind turbine rotor.

Illustration credit: reference [18].

Figure 28 shows that the radar returns from a fiberglass blade come from scattering centers that are distributed over the blade volume. Figure 29 shows that the blade cross sections also depend on rotation angle when the rotor axis is almost 90° from the radar range vector. The large zero-Doppler return seen in Figure 29 is likely from the tapered, flat-sided nacelle of the Repower turbine. The Doppler frequency spike that is associated

with the tower plus nacelle signature is of unknown origin and is probably a radar saturation artifact.

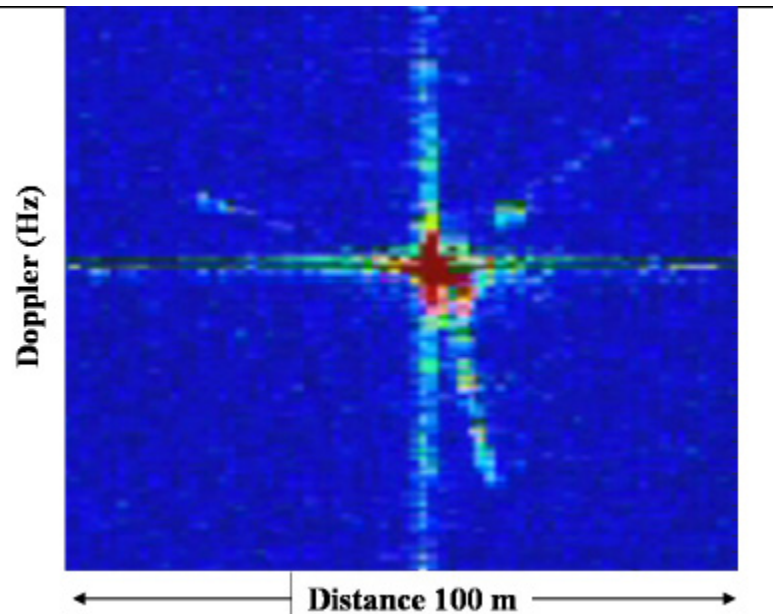


Figure 29: High resolution range-Doppler image of a REPOWER MM82 wind turbine at 90° yaw angle.

Illustration credit: reference [18].

4 Modelling wind turbine effects

Wind turbine RCS models can play several roles in determining and managing the impact of a single wind turbine or a complete wind farm on the performance of ASR systems.

1. The models can be used to assess the impact of proposed new or modified wind farms on existing ASRs by addressing the questions:
 - a. Will the presence of selected wind turbines severely degrade ASR performance?
 - b. How often will this occur?
 - c. Can terrain screening mitigation be used?
2. The models can be used to assess the impact of changing turbine type for proposed wind farm upgrades.
3. The models can be used to explore signal processing features to support ASR upgrades.
4. The models can be used to provide operational warning of unfavorable conditions for existing ASRs with wind farms in their field of view.

When evaluating the potential impact of a new wind turbine or a new wind turbine array in the field of view of an existing ASR, a generic RCS model can be conditioned by inserting available data about the proposed wind turbine properties and its observation geometry. Several model runs with different, expected, environmental conditions can be used to generate expected received signals that can then be analyzed in the context of the ASR properties and processing functions to determine ASR performance impacts and their probable occurrence frequencies. Target model calculations, combined with observation scenarios provide risk factor estimates for each new turbine type and location.

Where wind turbines are in place within the ASR field of view. Wind turbine RCS models can be tuned to the properties of the existing turbines and their observation geometries and can then be used to evaluate proposed signal processing upgrades or can be used to flag the onset of unfavorable air-target CFAR conditions from environmental data.

Although much work is in progress to minimize the radar RCS of wind turbine components [21], most of the features that are under investigation have not been implemented yet. This document focusses on the properties of turbines that do not use RCS suppression techniques.

At a detailed level, the international family of commercial wind turbines embodies a wide range of custom features which will have an impact on the RCS model for each turbine type. In practice, the operating constraints that define the major turbine design features restrict the unit-to-unit RCS variability to a set of scalable parameters [20] and a small set of selectable elements. Observations and commentary in the literature suggest that a general RCS model should be

constructible and should be able to provide static and dynamic RCS estimates that are within 5 dB of measured values.

The RCS model developed in this document combines the RCS estimates for the static and dynamic wind turbine components as seen by 2.7 to 2.9 GHz ASRs. The model assumes a far-field radar geometry but does not include coherent interference between radar signals that are returned from the modeled components.

Since available, published RCS modeling and experimental measurement results are usually incomplete for any system that is defined in the literature, a semi-empirical approach has been used to define and assemble the model components. In some cases such as scattering angle distributions, empirical rules have been based on disparate results and commentary. Where detailed descriptions of the S-band RCS are available and represent significant component features, these have been captured as reference models and are selectable in the composite RCS model.

All model components have associated scaling laws to allow the model to adapt to different turbine architectures.

Factors that need to be considered when configuring and operating a turbine RCS model include:

1. Turbine features:

- a. Turbine rotor size
- b. Nacelle design (shape)
- c. Tower height
- d. Cut-in wind speed
- e. Cut-out wind speed
- f. Rated wind speed
- g. Turbine rotation rate (if available for radar operations)
- h. Turbine yaw angle (if available for radar operations)

2. Environmental features:

- a. Wind speed statistics (prediction)
- b. Wind speed (operating)
- c. Wind direction statistics (prediction)
- d. Wind direction (operating)
- e. Turbine visibility from the radar (including partial terrain screening)

3. Radar features:
 - a. Instantaneous dynamic range
 - b. CFAR algorithm used
 - c. Scan rate
 - d. Elevation and azimuth beam patterns
 - e. Doppler filtering algorithms or filter specifications

The turbine dimensions, nacelle design and operating speed profile as well as the wind statistics and radar properties are predictive parameters that can be used to estimate the probable effects of the wind turbines on the radar operation and the statistical frequency of severe interference. When a turbine is in place, the dynamic parameters can be used to manage the interpretation of radar outputs and to activate mitigation routines if these have been developed. When dealing with operational turbines it would be valuable to acquire dynamic turbine parameters automatically from the wind farm owner for use in radar interference mitigation.

4.1 Static RCS effects and scaling laws

As observed by an ASR, a wind turbine signature consists of static radar returns (zero or very small Doppler components) from the turbine tower and nacelle and dynamic radar returns (significant Doppler components) from the turbine blades. The static returns will not affect the radar performance unless their received signal levels activate the radar automatic gain control functions or unless strong, static wind turbine returns alter the radar CFAR threshold. These effects are mainly seen on older radars.

The static radar returns can be estimated from the radar cross sections of the tower and the nacelle and from the radar range and observation geometry.

4.1.1 Wind turbine towers

The towers are tapered cylinders constructed of steel or concrete. Discussion in [14] indicates that the tower taper angle has a significant impact on the tower RCS. Discussions in [14] show that the 67 m, 0.8° taper Enercon tower studied has a RCS of approximately 100 m² between 1 GHz and 3 GHz. These data will form the baseline reference for tower RCS estimates.

Given the relationship between tower height and diameter, it is expected that a tower RCS will approximately scale from the Enercon reference as the square of the height ratio with respect to the reference to yield the rule:

$$A_{Tower} = 100 \left(\frac{H}{67} \right)^2 \quad (4)$$

for a tower that is H m tall.

4.1.2 Wind turbine nacelles

Although wind turbine nacelles are rotated to point the rotor into the wind, nacelle rotation responds to the local wind direction that has been averaged over many seconds. Nacelle rotation is activated when the difference between the nacelle axis direction and the average wind direction exceeds a threshold angle that lies between $\pm 5^\circ$ and $\pm 10^\circ$. Discussions in [22] suggest that the optimum wind direction integration time is 60 seconds and that the optimum yaw-error threshold angle is $\pm 8^\circ$. From the vantage point of an ACR, the nacelle RCS is static (it has no associated Doppler shift most of the time) but does vary with -mean wind direction over time.

Wind turbine nacelle RCS varies significantly with nacelle design. Figures 25 and 26 respectively show electromagnetic scattering model estimates for the 1.8 MW Enercon E66 nacelle shown in Figure 30 and the 600 kW Vestas V47 nacelle shown in Figure 31. Figure 31 actually shows the Vestas V 80 nacelle which is a scaled-up version of the V47 nacelle.

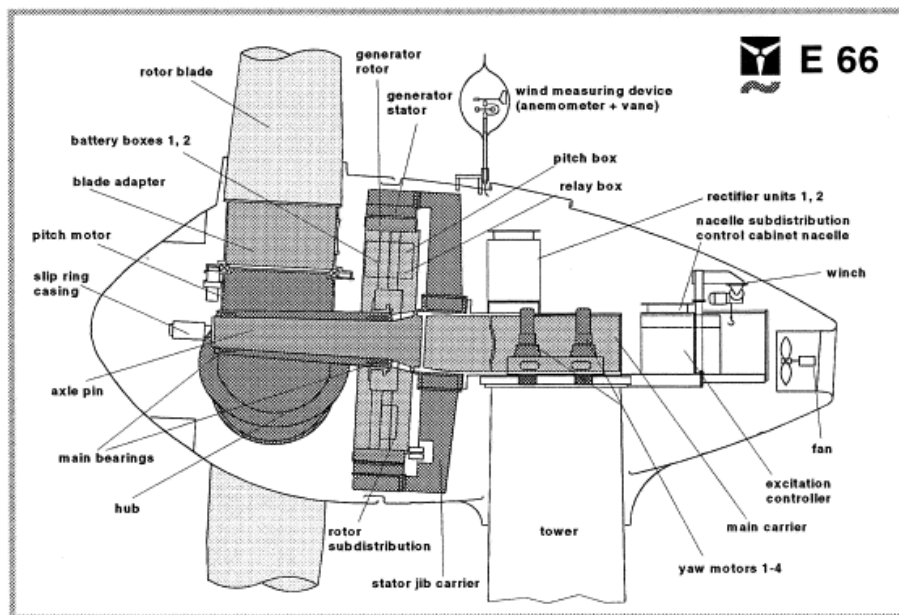


Figure 30: Side view schematic of the Enercon E66 turbine showing the nacelle profile and the major internal components.

Illustration credit: <http://mragheb.com/NPRE%20475%20Wind%20Power%20System>.

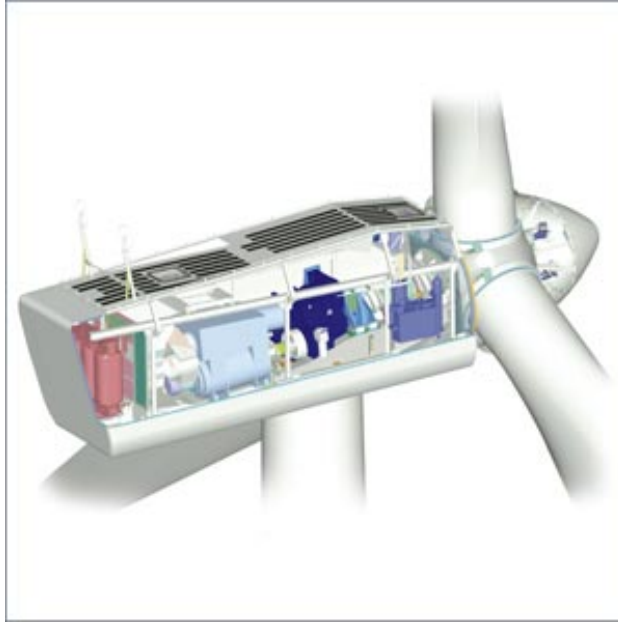


Figure 31: Vestas V80 wind turbine nacelle.

Illustration credit: www.interchopen.com.

The two nacelle configurations differ in peak RCS by more than 20 dB, primarily due to the RCS spikes at yaw angle $\pm 90^\circ$ for the Vestas nacelle's flat panel sides and rectangular form factor.

The Enercon E66 nacelle and the Vestas V47 nacelle represent two different nacelle architectures. For modelling purposes, the Enercon RCS data in Figure 25 are taken to be representative of rounded and tear-drop shaped nacelles used by Siemens, Enercon, Avantis and Acconia. The Vestas RCS data in Figure 26 are taken to be representative of rectangular, flat sided nacelles used by Vestas, Siemens, GE, Mitsubishi and Gamesa. The two nacelle shape classes are selectable reference parameters in the model.

The Enercon and Vestas nacelle models developed from Figures 25 and 26 are discussed in detail in Annex B.1 for the ASR frequency range. The yaw angle that is used in the model calculations is defined on a $\pm 180^\circ$ range where the yaw angle is measured between the turbine axis and the radar range vector to the turbine. 0° yaw corresponds to the turbine rotor facing the radar, $\pm 180^\circ$ corresponds to the turbine rotor facing away from the radar and $\pm 90^\circ$ represents an edge view of the rotor disk.

For RCS model calculations, once a nacelle type is used to select the reference model, the RCS needs to be scaled to compensate for the size discrepancy between the modeled reference nacelle RCS and the nacelle of interest. The scaling law is assumed to be proportional to the cross sectional area of the nacelle as viewed by the radar. Since this parameter is not readily available from public data, we will assume that the nacelle RCS reasonably scales as the square of the rotor hub diameter to yield:

$$A_{Nacelle} = A_{Nacelle_reference} \left(\frac{D_H}{D_{Reference}} \right)^2 \quad (5)$$

The hub diameter $D_{Reference}$ for the rounded nacelle model is 5 m and for the rectangular nacelle model is 3 m. The S-band (2.7GHz to 3.0 GHz) reference RCS $A_{Nacelle_reference}$ for the rounded nacelle is developed in Annex B.1.1 and $A_{Nacelle_reference}$ for the rectangular nacelle is developed in Annex B.1.2. $A_{Nacelle_reference}$ is a function of the yaw angle.

Results in Figure 25 and Annex B.1.1 show that for a 1.8 MW turbine similar to the Enercon design, the nacelle RCS approaches or slightly exceeds the tower RCS at yaw angles in $\pm 30^\circ$ intervals about -100° yaw and 100° yaw. At all other angles, the tower RCS dominates the static radar returns.

Results in Figure 26 and Annex B.1.2 show that for a 660 kW turbine similar to the Vestas design, the nacelle RCS exceeds the tower RCS for approximately $\pm 5^\circ$ about the -90° and 90° yaw angle orientations. The peak nacelle RCS at -90° and 90° is approximately 26 dBm^2 greater than the tower RCS and completely dominates the static RCS of the wind turbine. Applying the approximate scaling law to estimate the effects for a 1.8MW turbine, the peak RCS would exceed the tower RCS by approximately 35 dBm^2 and affected angle range about $\pm 90^\circ$ would expand to $\pm 10^\circ$. With the expected scaling, the RCS of the hub and aft ends of the nacelle are expected to become significant. The RCS models in Annex B.1 can be used to look at the problem in more detail as required. Large, rectangular nacelle turbines are expected to be troublesome for ASRs for a small and identifiable range of turbine yaw angles. For ASR operation, a knowledge of wind direction at the turbine site or actual turbine yaw angle can provide good indicators of expected aircraft detection problems.

4.2 Dynamic RCS effects

While the static wind-turbine RCS describes the radar returns from the turbine tower and nacelle and have no associated Doppler shifts, the dynamic RCS effects describe the radar returns from the turbine rotor and include the Doppler shifts from the rotor components caused by rotor rotation.

4.2.1 Wind speed effects

Figure 7 [23] shows the generic relationship between wind speed and turbine power output and shows the turbine operating regimes. All wind turbine designs have a similar diagram that is part of their operating specifications. Figure 32 shows the wind-speed / power curve for a 3 MW Enercon E82 turbine. This curve represents the theoretical power output of the turbine. For this turbine design, the cut-in wind speed is 4 m/s, the rated wind speed is 13 m/s, and the shut-down wind speed is 25 m/s.

Expanding on the general information provided in Section 2.3.1, when the wind speed, averaged over 10 minutes reaches the cut-in speed, the turbine nacelle is driven in yaw angle to place the turbine axis along the mean wind direction as measured at the top of the nacelle, the turbine

generator output is disabled, and the blade pitch angle¹ is adjusted into the mean wind direction. When the blade rotation speed increases, the blade pitch is adjusted away from the wind direction and towards the rotation velocity direction until the rotor is turning quickly enough to drive the generator at its minimum starting speed. Information from [23] suggests that the rotor starting time is approximately five minutes for turbines delivering 2 MW or more. When the turbine rotor reaches its minimum useful rotation rate, the blade pitch is reduced to zero and is left there until the turbine reaches its rated speed. The turbine generator is activated at its starting rotation rate and the generator rotation rate increases in proportion to the wind speed until the turbine rotation rate and power output reach their rated values. As the wind speed increases beyond the turbine rating, the blade pitches are controlled to maintain constant power output until a shut-down wind speed is reached. When the mean wind speed reaches the shut-down condition the blade pitch is increased to aerodynamically stall the blades and the turbine is stopped and parked with the turbine axis at 90° to the mean wind direction.

During power generation, the pitch angle of each turbine blade is dynamically controlled as a function of rotation angle as shown in Figure 12 to compensate for the vertical variation in wind speed due to the terrain boundary layer illustrated in Figure 11 and to compensate the up-wind boundary layer effects from the turbine tower.

To a first approximation the turbine rotation rate varies as:

$$\omega = \frac{\omega_{Rated} - \omega_{Start}}{V_{Rated} - V_{Cut-in}} V_{Wind} \quad (6)$$

where V_{Wind} is the 10 minute average wind speed. Equation 4 does not include generator loading effects which are also used for rotation rate control.

In most wind farms each turbine is self-controlled and local wind conditions can only be broadly inferred from area or coarsely gridded measurement data due to local terrain effects. Area estimates of wind speed and direction will be of some value for the estimation of expected effects but real-time data from wind farm operators will be operationally valuable for monitoring air-traffic radar interference.

Figure 32 shows a computed power output curve based on published data for an Enercon E 82 turbine [33].

¹ The lift forces driving the turbine rotation are controlled by the airfoil angle of attack with respect to the local wind speed. Since the turbine rotation rate varies radially from the hub, the blades are twisted along their length (Figure 6) to produce a radially varying angle of attack. The actual angle of attack is controlled as a function of rotation rate and required efficiency by adjusting the blade pitch angle.

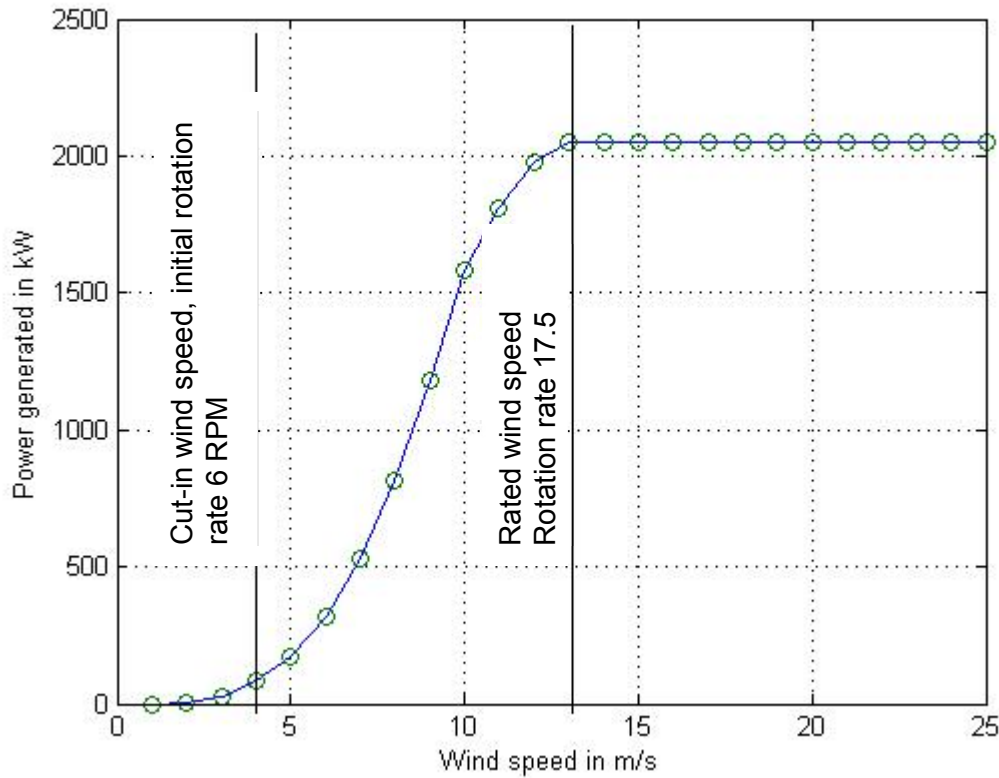


Figure 32: Wind power curve for a 2 MW Enercon turbine.

4.2.2 Rotor RCS model for yaw angles -175° to -5° and 5° to 175°

When the yaw angle is more than $\pm 5^\circ$ from 0° and $\pm 180^\circ$, the radar returns from the turbine rotor come from the vertically oriented blades and from the rotor hub. When the yaw angle lies within $\pm 5^\circ$ of either 0° or $\pm 180^\circ$, a coherent integral over all three blades and the rotor hub contains contributions from all rotor components and has a very small Doppler component, and its power varies with rotation angle as shown in Figure 21. Coherent modelling of a turbine rotor [22] shows this power is approximately six times larger than the return from a single vertical blade view at yaw = 90° .

For the yaw angle range that contributes significant Doppler frequency shifts, $5^\circ \leq \text{yaw} < 175^\circ$ and $-175^\circ \leq \text{yaw} < -5^\circ$, we will use Enercon E66 data from [15] to generate a turbine RCS model for a rotating turbine. For simplicity and in recognition of structural differences in the rotor components, the turbine rotor will be modelled in three parts:

1. the rotor hub assembly,
2. the rotor blades, and
3. blade-tip features.

The blade tip features that are often observed in wind turbine RCS power spectra are probably related to lightning protection system components.

An approximate plan view of the rotor blade is shown in Figure 33.

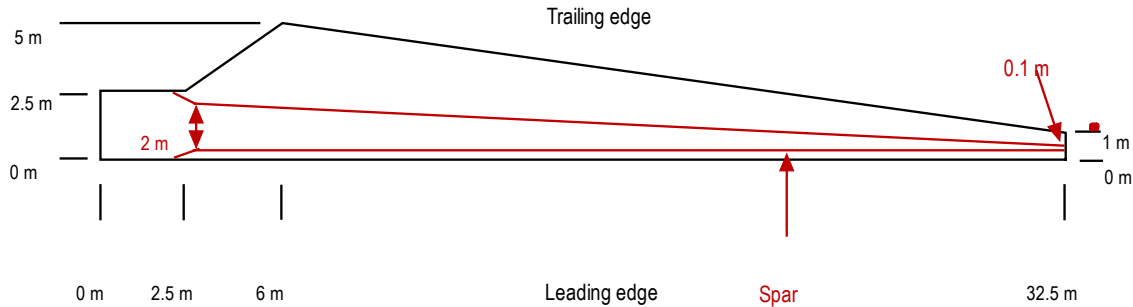


Figure 33: Schematic plan view of the turbine blade.

For and Enercon E66 blade, the blade root attachment point in the rotor hub is assumed to be 1.1 m from the hub center and the maximum hub fairing diameter is assumed to be 5 m. Both assumptions are based on judgements made from structure photographs. Dimensioned details have not been found. The blade root is assumed to be a circular cylinder and the blade cross section transitions to an airfoil when the blade reaches full width. The internal blade structure is assumed to be a box beam similar to that illustrated in Figure 4.

For the rotor RCS model calculations the turbine will be viewed at 90° yaw angle (the radar views the rotor edge). We will model a vertical blade as its mechanical cross section (thickness T) given by $T = 2.5$ m for $0 \leq L < 2.5$ m and $T = 2.5 - 0.08(L - 2.5)$ m for $2.5 \text{ m} \leq L < 32.5$ m, where L is the distance from the blade root attachment point to the computation point. L_{Max} is the blade length shown in Figure 33. The blade thickness at the blade tip is assumed to be 10% of the blade chord. The internal blade spar is centered on the maximum blade thickness. Assuming a blade shell thickness of 0.125 m at the spar root, the spar thickness (viewed from the blade leading edge) varies from 1.75 m at the spar root to 0.08 m at the blade tip (assuming a blade-tip shell thickness of .01m). We will assume that the blade spar has an approximately rectangular cross section as shown in Figure 4. The rotor radius at the computation point, as measured from the hub center, is $R = L + 1.1$ m.

Analysis reported in [21] shows that the RCS of fiberglass blade structures is not well represented by the shell alone and that the central spar contributes at approximately half of the expected blade RCS. Modelling results that display RCS for a vertical blade as a function of yaw angle must be treated with caution if the central spar structure is not included in the model. The shape of the spar suggests that the rotation angle dependence of the leading and trailing edges may demonstrate an approximately 2° asymmetry in the spar component of the RCS. [21] also suggests that the electromagnetic scattering interaction between the blade shell and the blade hub has a broader scattering angle dependence than the blade shell alone.

The rotor hub is modelled as the hub fairing over the radius $0 \leq R < 2.5$ m (for the Enercon E66 reference model) but has a rotation-angle dependent modulation caused by the blade root attachment fixtures. This modulation will vary from turbine to turbine depending on the hub design. We will use a scattering approximation for which the scattered radar signal power varies

as a Gaussian function of observation angle in blade-root model calculations to estimate observed rotor power spectrum features.

RCS observations along the length of turbine blades provide information on the radar scattering distribution in this dimension. The ISAR image, shown in Figure 28 [19], shows that the largest turbine blade RCS comes from the blade root section and the blade RCS declines towards the blade tip. The largest scattering contributions from the 40 m blades in this figure come from the central 6 m of the blade and hub structure.

To estimate the distribution of RCS along the length of a turbine blade a turbine Doppler spectrum for a full rotor rotation, Figure 34, was used to generate two simplified functions corresponding to approaching blades (leading edge) that have positive Doppler shifts and receding blades (trailing edge) that have negative Doppler shifts. The data in Figure 34 will support a more complex spectrum-magnitude / Doppler frequency approximation but, since only one example of this type has been found, the simplest, reasonable form was deemed to be the most appropriate. If other data are found, they can be incorporated in the model by the use of a selection command to designate the most appropriate model.

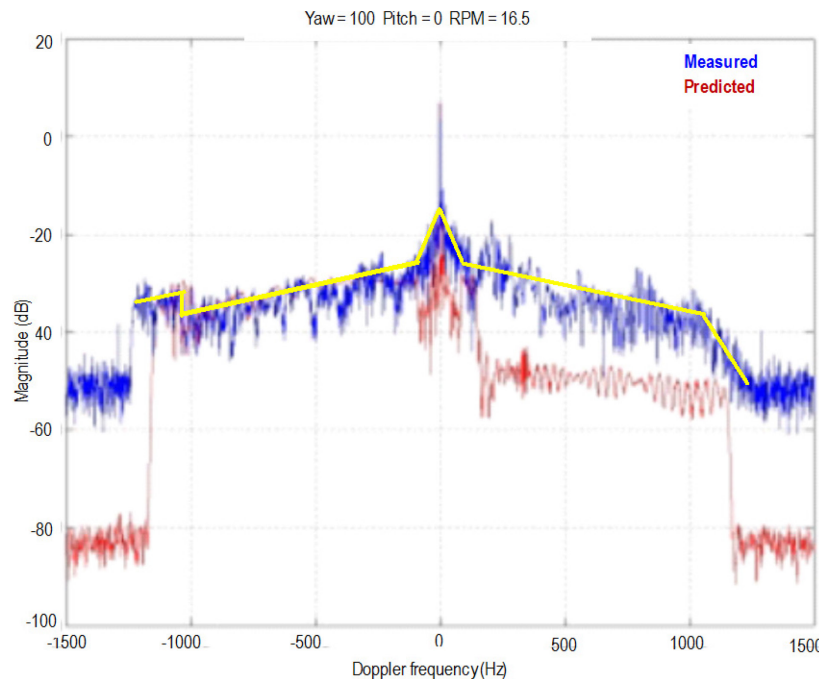


Figure 34: Enercon E66 measured (blue) and predicted (red) Doppler spectrum over 1.5 rotations.

Image credit: reference [14].

To generate scalable functions, the data in Figure 34 was normalized to -16 dB (nominal zero Doppler). The frequency scale was converted to a blade radius scale using:

$$R = \frac{\lambda f_D}{2\omega} \quad (7)$$

where λ is the radar wavelength (nominally 0.10 m), f_D is the Doppler frequency in Hz and ω is the turbine rotation rate in radians/s. Although the rotation rate reported in [14] is 16.5 RPM, the best fit between the Doppler spectrum and the blade length is achieved at 17.8 RPM. Figure 34 contains data from the edge-viewed full turbine over 1.5 rotor rotations and the Doppler spectrum is dominated by the blades in their two vertical positions, up and down. For the creation of a simple blade RCS model, the data are assumed to represent the vertical blade positions where the blades are rotating towards and away from the radar. To generate a simple RCS model, the positive and negative halves of the spectrum in Figure 34 are represented by linear segmental approximations shown by the yellow lines in the figure. The positive and negative Doppler spectra are different due to the blade shape as viewed by the radar and due to the (assumed) visibility of part of the lightning protection system (seen as an RCS step near the negative spectrum blade tip). The discrepancies between the modeled and measured results in Figure 34 suggest that a multi-path interaction between the blade and the turbine tower is present in the assumed vertically down blade position (positive Doppler).

The blade that is rotating away from the radar is assumed to be vertically up so that the observation yaw angle is -90° .

The magnitudes of the normalized negative spectrum data (blade trailing edge) were modeled in a linear segmental sense and then converted to linear quantities to yield Table 3. The blade flash RCS results can be scaled to other yaw angles [24]. Available data to estimate the scaling relationships is spotty and an empirical relationship is proposed. Sources agree that the pressure side of the blades seen at yaw angle 0° can be 10 dB larger than the maximum returns from the other side of the blades and that the RCS at 90° yaw angle is somewhat smaller than either of these.

Table 3: *Enercon E66 normalized Doppler spectrum for the blade trailing edge (negative Doppler).*

R	$10\log_{10}(F)$	F	Notes
$0 \leq R < 2.45$ m	-4.48R	$10^{-0.448R}$	Rotor hub
$2.45 \leq R < 33.5$ m	$-11-0.426(R-2.45)$	$10^{-1.1-0.0426(R-2.45)}$	Blade
$28.8 \leq R < 33.5$ m	$-17-0.426(R-28.8)$	$10^{-1.7-0.0426(R-28.8)}$	Blade tip feature

The magnitudes of the normalized positive spectrum data (blade leading edge) were modeled in a linear segmental sense and then converted to linear quantities to yield Table 4.

Table 4: *Enercon E66 normalized Doppler spectrum for the blade leading edge (positive Doppler).*

R	$10\log_{10}(F1)$	F1	Notes
$0 \leq R < 2.45$ m	-4.48R	$10^{-0.448R}$	Rotor Hub
$2.45 \leq R < 27.5$ m	$-11-0.37992(R-2.45)$	$10^{-1.1-0.037992(R-2.45)}$	Blade
$27.5 \leq R < 33.5$ m	$-21-2.50(R-27.5)$	$10^{-1.1-0.0250(R-27.5)}$	Blade

The $10\log_{10}(F)$ and $10\log_{10}(F1)$ columns of Tables 3 and 4 respectively are plotted in Figures 35 and 36.

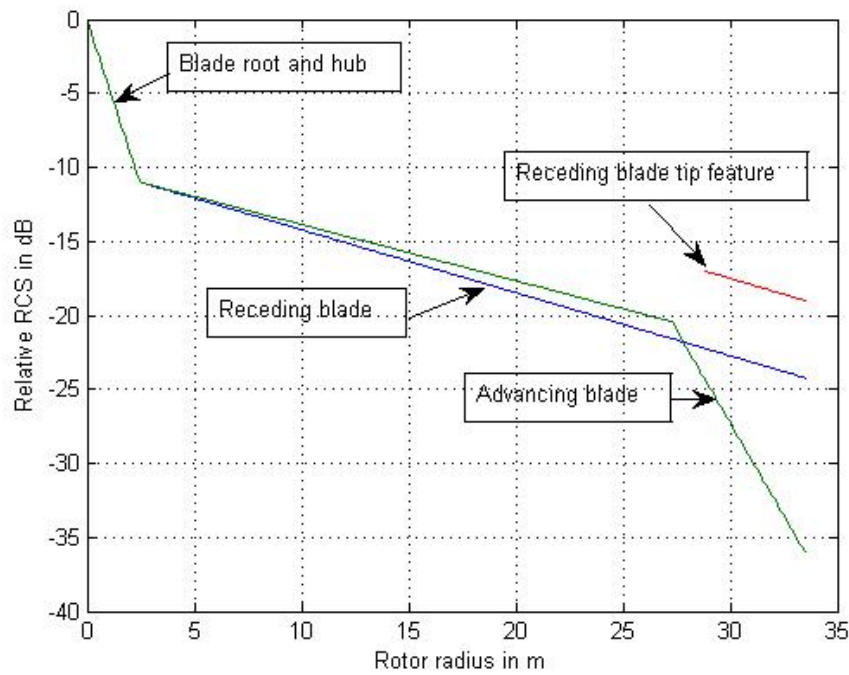


Figure 35: Linear segmental models of the normalized Doppler spectrum in Figure 34 in dB.

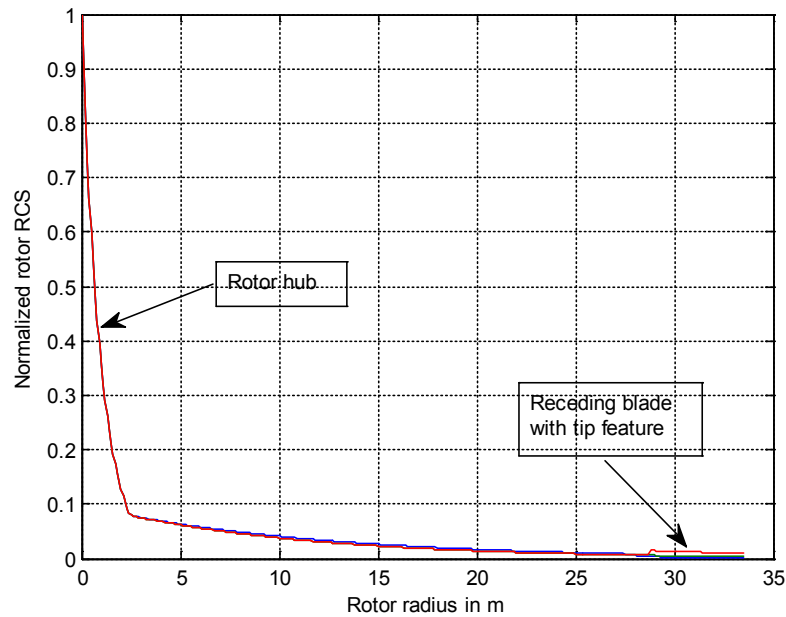


Figure 36: Normalized blade cross section functions for the Doppler spectrum in Figure 34.

The integral of F over the turbine's 33.5 m radius is 6.3685. For the Enercon E66 blade at rotation angles of 0°, 120° and 240°, and a yaw angle of 90° the RCS is 30 dBm² (1000m²). The linear scaling factor for the blade RCS is 157 to produce the RCS as a function of radius in m².

The integral of F1 over the turbine's 33.5 m radius is 5.0669. Assuming the same RCS scaling as for the previous blade orientation, the total blade RCS is 1 dB smaller at 60°, 180° and 300° turbine rotation angles. Even larger asymmetries are seen in many reported cases.

The information provided in [14] does not define the blade rotation direction. Comparison of Figures A.5 and 34 show significant discrepancy (~20dB) between the predicted and measured RCS for the vertically down, positive Doppler case. It is assumed that the positive Doppler spectrum contains the tower multi-path interference effects.

The raised RCS feature near the blade tip for the trailing edge Doppler signature and its absence for the leading edge Doppler signature is compatible with rotation angle dependent blade tip features seen in Doppler spectrum time histories of the form shown in Figure 18.

Observations reported in [14] suggest that the RCS of a near vertical blade is only significant over turbine rotation angles of the order of $\pm 5^\circ$, and results in [21] suggest that the RCS is within approximately 15 dB of the peak over 5° and within 20 dB of the RCS peak over 7.3° of rotation. Antenna range measurement results shown in Figure 16 support these observations and discussions in [22] note that the blade spar is a significant contributor to the blade RCS. Since the radar scattering properties of the blades are not well documented we will assume the slightly-rough surface model for radar scattering [25] (small scale RMS (Root Mean Square) surface relief is less than 0.03λ where λ is the radar wavelength) applies so that the angular width of the blade scattering has the functional form:

$$A(R, \varphi) = \sqrt{G(R)} e^{-\left(\frac{\varphi}{\gamma}\right)^2} \quad (8)$$

where:

- A is the power of the scattered signal,
- G is either F from Table 3 or F1 from table 4,
- φ is the turbine rotation angle measured from the vertical, and
- γ is the function width (or roughness) parameter expressed in the units of φ .

This model seems to be empirically reasonable but does not fit the scattering physics involved as the blade surfaces are actually smooth and the scattering appears to be caused by some combination of volume and multiple-surface radar reflection effects within the blade structure.

To match with the apparent conditions of Figure 34, we assume that the turbine is rotating clockwise in the standard manner and that it has been measured at yaw = -90°.

The blade RCS has the form shown in Figure 36 in m² and Figure 35 in dBm² and is compatible with published comments about the scattering width. The functional form does not match that

shown in [21] Figure 29 (the figure quality does not permit insertion here). Taking the entire blade to have the angular scattering dependence of equation (8), we have the rotation angle dependence shown in Figure 37.

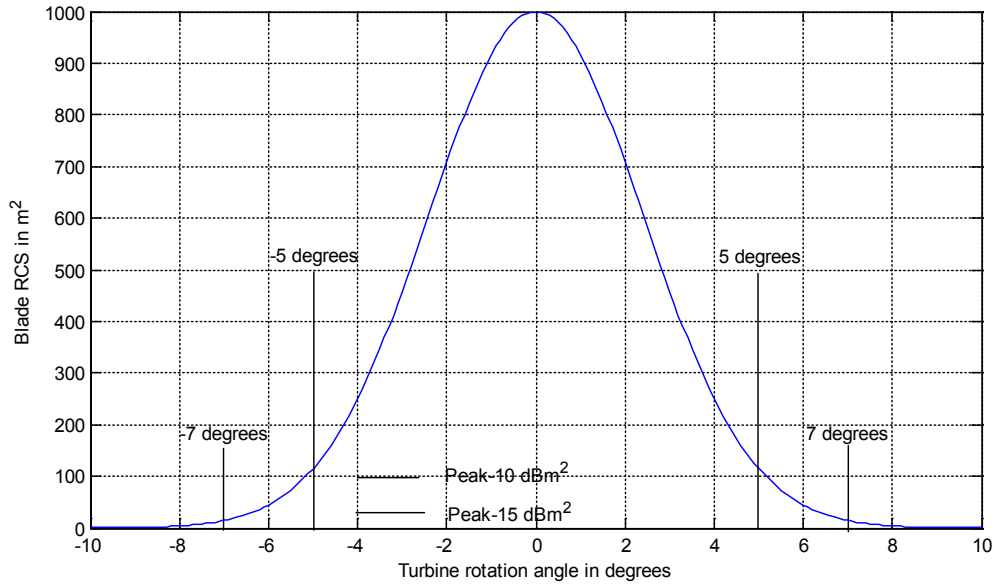


Figure 37: Single blade RCS in m^2 for a blade vertically up.

An examination of Figures 35 and 36 shows that the rotor hub is the major contributor to the rotor RCS. The hub structure shown in Figure 30 is quite complex and contains the blade mounts and the pitch drive motors covered by a fairing. No RCS data was found for the hub assembly and the following model assumptions were made:

1. The hub assembly fairing is assumed to be parabolic with tangents at $\pm 160^\circ$.
2. The RCS of central 1 m hub radius is assumed to not depend on the yaw or turbine rotation angles.
3. The RCS blade mounting structure and blade root components within the hub fairing are assumed to be independent of yaw angle except for shadowing effects and the RCS varies with rotation angle at three times the rotor rotation rate.
 - a. The blade root RCS is assumed to be a Gaussian function of rotor rotation angle as shown in equation 8. Scattering width (roughness) parameters between 20° and 30° appear to be compatible with observed data.
4. The hub RCS is assumed to vary with radius as shown in Figure 35.

Until further information on the hub scattering structure is found, all turbine hubs will be treated in the same manner and will be scaled to the reference turbine hub diameter.

To be observationally compatible with published rotor spectrum time histories, the blade tip feature shown in Figure 34 is treated as a low RCS structure whose scattering angle dependence follows equation (8) with the scattering-width (roughness) parameter β set to 34° .

The rotor model is constructed as the sum of the hub, blade and blade tip RCS functions where the Doppler frequency is proportional to the radius distance from the hub center and to the turbine rotation rate. The turbine rotor RCS is the integral of all components over the rotor radius.

Combining these terms for the Enercon E66 reference turbine, turning at 16 RPM, we get the power-spectral history shown in Figure 38.

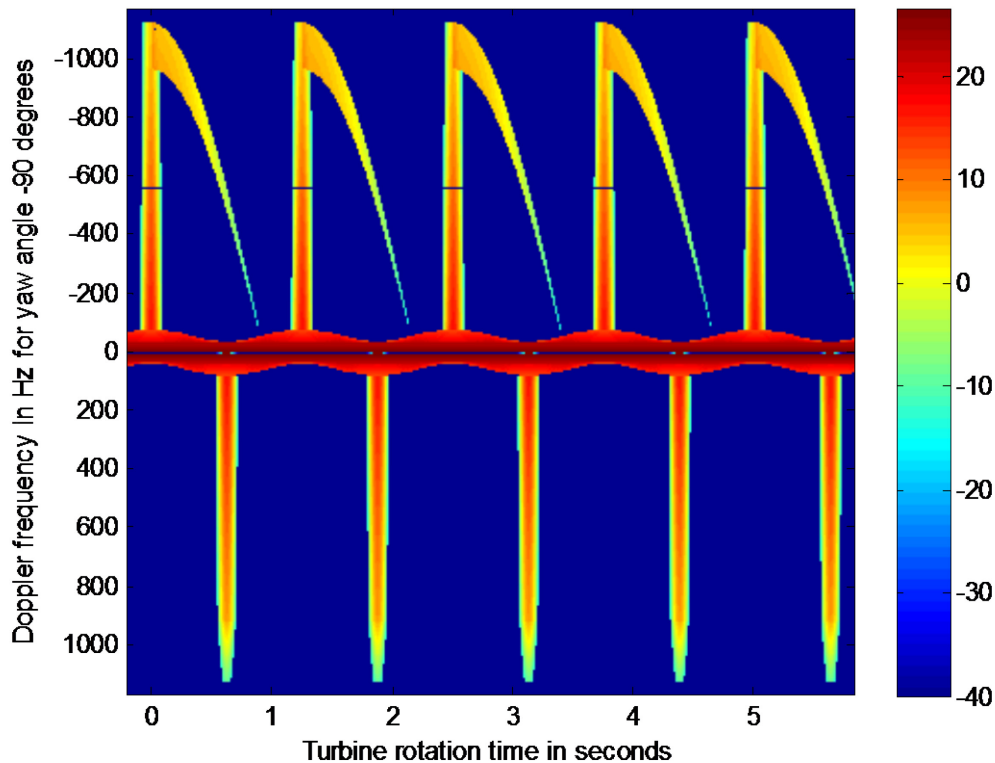


Figure 38: Spectral history for the Enercon E66 reference model turning at 16 RPM and viewed at -90° yaw angle. The color bar gives the turbine rotor RCS in dBm^2 .

Since the distribution of scattering centers within a turbine blade is unknown we will assume that the scattering phase is zero while the vertical axis is within a square cross section spar within the rotating blade and otherwise varies with radar range from the blade center in the normal manner. Summing the complex radar returns over 1.5 rotations, converting to RCS and scaling the result, the radar cross section sequence (in dBm^2) shown in Figure 39 is seen when the tower RCS is ignored. Figure 40 displays the rotor, nacelle and tower RCS in dBm^2 when the yaw angle is 90° and when coherent interference effects between the nacelle, tower and the rotor blades are ignored.

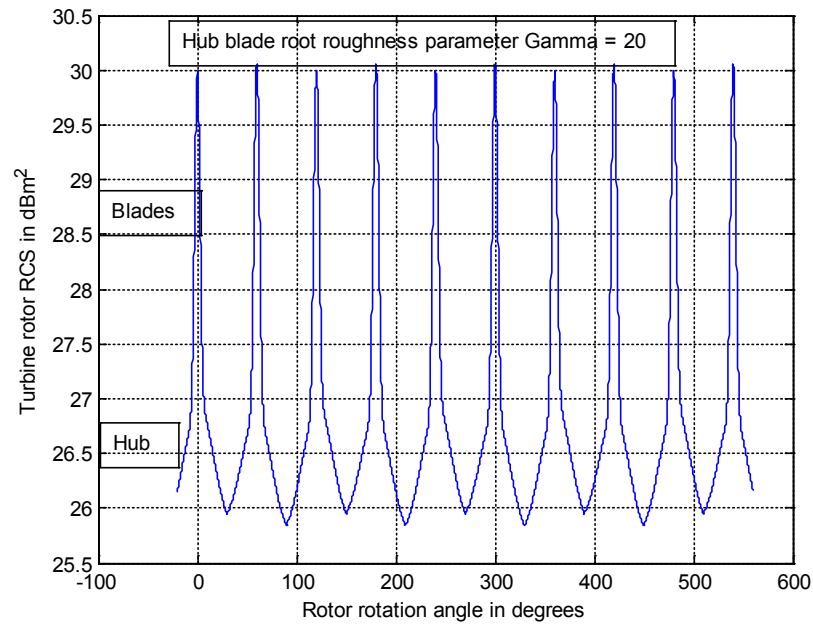


Figure 39: Enercon E66 rotor RCS at yaw angle 90° and rotation rate 16 RPM.

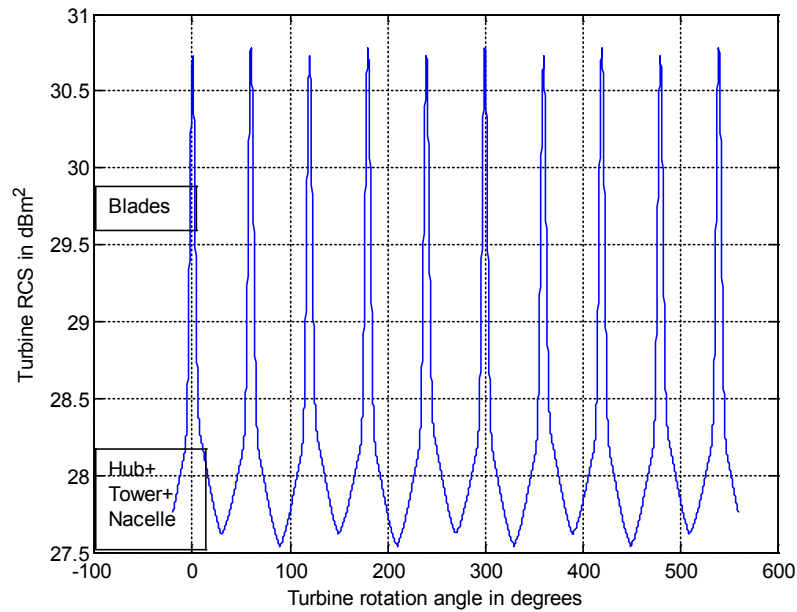


Figure 40: Enercon E66 reference turbine RCS.

In Figure 39 we see that the turbine hub contributes most of the rotor RCS.

Noting that all ASRs use Doppler filters to suppress stationary clutter, define a simple, two-pole high-pass filter with a -3 dB cut-off at f_3 Hz as:

$$H(f) = \left(\frac{\left(\frac{f}{f_0}\right)^2}{1 + \left(\frac{f}{f_0}\right)^2} \right)^2 \quad (9)$$

where f is the turbine Doppler frequency at rotor radius R and $f_0 = 0.6383f_3$ Hz is the reciprocal of the filter time constant. The turbine rotor is a rigid rotator and thus the filter frequency parameters are proportional to the rotor radius so that:

$$f = \frac{2\omega R}{\lambda} \sin(\theta_Y) \quad (10)$$

for rotor radius R , turbine rotation rate, ω yaw angle θ_Y and radar wavelength λ .

Converting $H(f)$ to $H(R)$ and applying the simple high-pass filter (HPF) with $f_3 = 55$ Hz to the rotor RCS we see in Figure 41 that the blade root component of the hub assembly still dominates the turbine RCS but that the tower, nacelle and hub center RCS contributions have been removed.

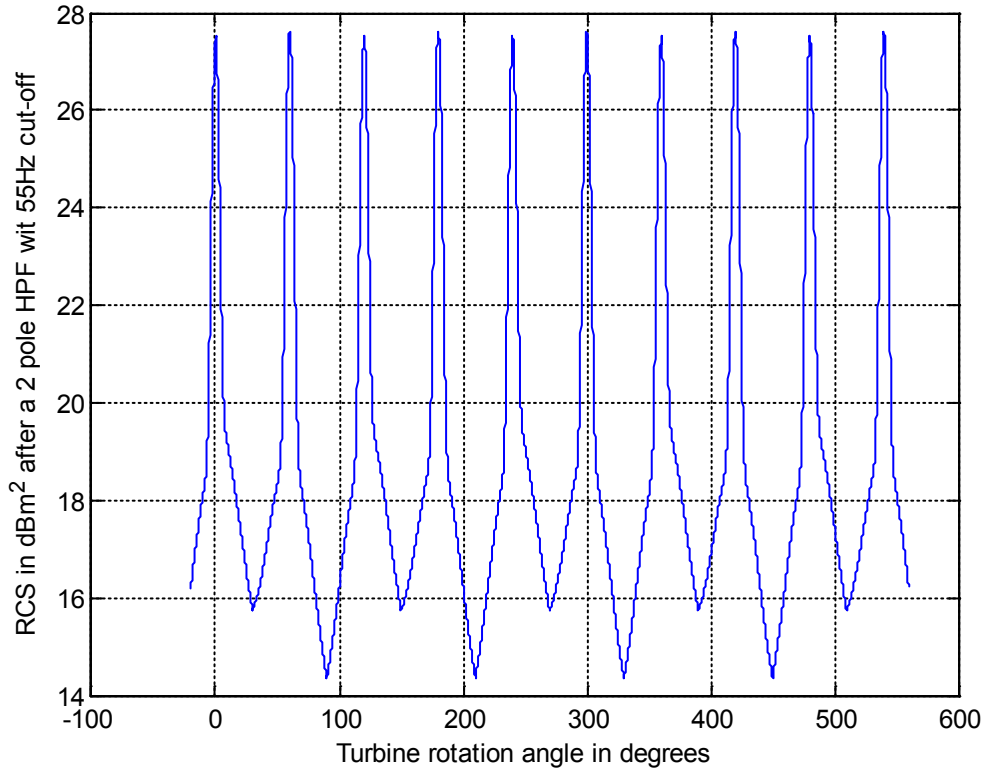


Figure 41: Enercon E66 turbine RCS after a two-pole high pass filter with 55 Hz cut-off.

4.2.3 Rotor RCS model for yaw angles within $\pm 5^\circ$ of 0° and $\pm 180^\circ$

When the ASR views the turbine rotor nearly face-on or nearly from the back face view, the rotor Doppler spectrum is constrained to the frequency range near 0 Hz and the Doppler spectrum width is given by equation (10) with the radius R replaced by the rotor radius. For the Enercon E66 reference turbine turning at 16 RPM, the Doppler spectrum width is 210 Hz centered at 0 Hz when the yaw angle is $\pm 5^\circ$ from the turbine rotation axis.

No data that describes the radial RCS distribution for the turbine rotor at yaw angles near the turbine rotation axis has been found. However, detailed model calculation of an Enercon E66 turbine [15] described in Figures 21 and 22 for yaw angle 0° show that the envelope of turbine RCS maxima varies from approximately 28 dBm² to approximately 15 dBm² with a functional form:

$$\sigma_{turb} = \frac{(\sigma_{max} + \sigma_{min})}{2} + (\sigma_{max} - \sigma_{min})\cos(3\varphi + 120) \text{ dBm}^2 \quad (11)$$

for rotation angle φ in degrees.

Model calculations in [14] show that the application of a narrow-bandwidth zero-Doppler filter (the filter bandwidth is not specified in [14]) to the results shown in Figure 21 yield $\sigma_{max} = 28 \text{ dBm}^2$ and $\sigma_{min} = 9 \text{ dBm}^2$. The empirical data for the entire turbine shown in Figure 23 sets the σ_{max} to approximately 33 dBm^2 and σ_{min} to approximately 21 dBm^2 . For this turbine design, the nacelle is masked by the rotor hub at 180° yaw angle. The empirical minimum RCS from Figure 23 and equation (11) corresponds to rotation angles where one blade is vertically up and also contains the turbine tower RCS. Figure 21 also shows the tower masking effect by a vertically down blade to yield a peak RCS reduction of approximately 5 dB. In the RCS measurements shown in Figure 23, the tower interaction notch depth is approximately 7 dBm². Equation (11) represents the expected rotor signature when the turbine is operating in its constant speed regime and when dynamic blade pitch control is active. It is expected that the term $(\sigma_{max} - \sigma_{min})$ will approach zero when the turbine is not under pitch control.

We will use equation (11) as an empirical model of the dynamic component of wind turbine RCS when the turbine is viewed within $\pm 5^\circ$ of yaw angles 0° and 180° . The constants in equation (11) scale with the rotor area ratio $A_{Rotor}/(AE_{66})$ in dB.

Note that equation (11) only models the fundamental component of the temporal variation of the rotor RCS signature at 0° yaw angle and that the observed RCS will be modulated by fine-structure as is illustrated in Figures 21 and 23. Later in the discussion, we will conceptually couple the RCS modulation amplitude to dynamic pitch control of the individual turbine blades that is exercised when the wind speed exceed the rated wind speed for the turbine.

The variation of the turbine rotor RCS with radius is required to address terrain screening effects. No quantitative sources have been found that allow the rotor RCS to be decomposed into its radial dependence for yaw angles near 0° or 180° . From the inverse SAR spotlight image shown in Figure 28 and the range-Doppler image shown in Figure 29, the RCS of the blade root portion of the hub assembly is large and the RCS of the rest of the turbine blade varies approximately as the area of the plan view of the blade. This observation is also made in [14]. Unfortunately the RCS colour bar that gives the relative magnitudes of the radar returns is not available from the source [19] of Figure 28.

Since crucial details describing the radial dependence of turbine rotor RCS values have not been found for 0° yaw, we combine available observational comments and the blade plan view from Figure 33 to form the following RCS model proposal for one blade for the reference turbine. Until data is found to evaluate this model it must be considered to be speculative.

Figure 33 is a simplified plan view of an Enercon E66 turbine blade that does not include the blade twist. The figure identifies three blade outline regions:

1. The blade root is a cylindrical structure that extends from the blade mount at 0m to the blade transition region at 2.5 m. This is a thick-walled composite structure that contains embedded metal mounting structures.
2. The blade transition region is composed of partial airfoils that start at the blade root (at 2.5 m radial distance and extends to the full blade airfoil regions at radial distance 6 m.

3. The blade airfoil region is the blade lifting body and is composed of a sequence of airfoil profiles that start with low-velocity shapes and transition to high-velocity shapes at the blade tip. Table 1 shows an example blade cross section sequence for a 61 m blade. For the Enercon E66 blade illustrated by Figure 33, the airfoil region starts at 6 m radial distance from the blade attachment point and extends to the blade tip at 32.5 m radial distance from the same reference.

The blade is assumed to contain a box-beam spar illustrated in Figure 4 and outlined in Figure 33. From discussions in [22], the spar makes significant contributions to the blade RCS at all yaw angles. We will assume that it contributes 50% of the transition region and airfoil region RCS (in m²). The dielectric blade anechoic chamber measurements shown in Figure 16 suggest that the RF scattering from the blade shell is distributed over the blade according to a relationship between the propagation direction of the illuminating signal and the blade structure. Since the required structural information is not available, we will make the following simple assumptions and assertions using the symbols; $\sigma_X(L)$ is the radar cross section of component X (X is B for the blade surface and S for the spar) at radial distance L from a reference, σ_X is the integrated radar cross section of component X and σ_X^0 is the normalized radar cross section of component X per unit area:

1. From the start of the blade transition region to the blade tip, the blade RCS in m² per unit radial distance is proportional to the sum:

$$d\sigma_B(L) = (\sigma_B^0 w_B(L) + \sigma_S^0 w_S(L))dL \quad (12)$$

where:

- L is defined as the radial distance from the blade attachment point at the turbine hub,
 - σ_B is the radar cross section of the blade in m²,
 - σ_1^0 is the normalized radar cross section of the blade shell,
 - $w_B(L)$ is the blade shell width at radius R=L+1.1,
 - σ_2^0 is the normalized radar cross section of the blade spar,
 - $w_S(L)$ is the spar width at radius R=L+1.1,
 - dL is a blade length increment.
2. The blade width and the spar width in the transition region and in the airfoil region are given by:

$$w_B(L) = 2.5 + 0.676(L - 2.5) \text{ and } w_S(L) = 2 - 0.0629(L - 2.5) \text{ for } 2.5 \leq L < 6 \quad (13a)$$

and:

$$w_B(L) = 5 - 0.151(L - 6) \text{ and } w_S(L) = 2 - 0.0629((L - 2.5) \text{ for } 6 \leq L < 32.5 \quad (13b)$$

3. Using the spectral data for the rotor hub from Table 3, the RCS at radius R is proportional to:

$$\sigma_{root}(L) = 10^{-0.488L} \text{ for } 0 \leq L \leq 2.5 \text{ and } \sigma_{root}(L) = 0 \text{ for } L > 2.5 \quad (14)$$

since the blade root cross section is cylindrical and should not depend on azimuth angle. From estimates based on Figures 34 and 36, the blade root and hub center combined contribute approximately 40% of the blade RCS.

4. If we assume that the blade surface and the spar contribute equally to the blade RCS then $\frac{\sigma_B^0}{\sigma_S^0} = \frac{\int_{2.3}^{32.5} w_S(R) dR}{\int_{2.3}^{32.5} w_B(R) dR} = 0.35$. Any other contribution proportionality can be obtained by appropriately weighting the integrals.
5. Lacking other evidence, we will assume that the central portion of the rotor hub (1 m radius) behaves as a disk that has a uniform normalized RCS σ_H when viewed from 0° yaw angle and does not contribute to the rotation angle dependence of the rotor RCS. The hub contribution to the total rotor RCS is $\sigma_{Hub} = 2\pi\sigma_H R_H^2$ where the hub radius is R_H .
6. The RCS of a rotor blade assembly can be expressed as a function of rotor radius R for an Enercon E66 turbine as:

$$\sigma_{Blade}(R) = \int_{1.1}^R (k_1 \sigma_{root}(x) + \sigma_B(x)) dx \quad (15)$$

for $1.1 \leq R < 33.6$ and $\sigma_B(L) = \sigma_S^0(0.35w_B(L) + w_S(L))$ when the blade rotation angle is not considered. The relative values of k_1 and σ_S^0 can be estimated from the relative contribution of the blade RCS and blade root RCS to the RCS of their sum.

The turbine RCS in equation (11) contains the sum of contributions from all three blades as a function of rotation angle when the turbine is operating with its blades under dynamic pitch control. Equations (12) to (15) are not dependent on rotation angle. Noting that each blade has the same twist (for example, Figure 1 and Table 1), the blade geometry seen from yaw angle 0° is constant at all rotation angles and the rotor RCS is simply the sum of the hub RCS and the RCS of the three blades when pitch control is not active.

If we assume that the RCS of a single blade seen from yaw angle 0° is the same as the single blade RCS at 90° yaw as discussed in Section 2.2, the RCS of the rotor disk viewed at 0° yaw will be approximately 5 dB larger than the RCS of the rotor disk viewed at 90° . Calculations reported in [21] place this ratio at approximately 8 dB for a different rotor design. This suggests that the

blade RCS at yaw angle 0° is approximately twice the RCS at yaw angle 90° . We will assume without justification that this ratio is universal. From our previous discussions and using results presented in Figures 39 and 41 for the E66 turbine the total rotor RCS is $\sigma_{Rotor} = \sigma_{Hub} + 3k_1 \int_0^{2.5} \sigma_{root}(L) dL + 3 \int_{2.5}^{32.5} \sigma_B(L) dL \approx 6300 \text{ m}^2$, $\sigma_{Blade}(32.5) = 2000 \text{ m}^2$, $\sigma_{Hub} \approx 300 \text{ m}^2$, $k_1 \sigma_{root} = 770 \text{ m}^2$ and $\sigma_B \approx 1230 \text{ m}^2$. Integrating equation (11), using the functions in equation (13) and the ratio defined in (4), $\sigma_2^0 \approx 18.336$. Integrating the second term of equation (15) $k_1 \approx 8.77$.

For terrain shadow masking calculations, the turbine rotor RCS variation with time can be estimated from the turbine rotation rate and the rotor radius at which three blades spaced at 120° rotation angle fall within the shadow mask as a function of rotation rate and rotation angle.

When the turbine is operating at its rated rotational speed and the wind speed is above the rated wind speed, the blade pitch angles are dynamically adjusted as a function of rotation angle as illustrated in Figure 12. The pitch angle variation imposed on the blades is a function of the wind speed and is adjusted to decrease the blade efficiency as the cut-out wind speed is approached. The maximum and minimum rotor RCS in Figure 21 correspond to the one blade up and one blade down conditions as shown in Figure 22. Since the blade pitch is the only turbine rotor parameter that systematically varies with turbine rotation angle we can combine the information in Figures 12, 21 and 22 to infer that the minimum pitch angle corresponds to the largest rotor RCS and the maximum pitch angle corresponds to the minimum rotor RCS.

A functional model for the turbine rotor RCS at yaw angle 0° with no shadowing effects is then:

$$\sigma_{Rotor} = \sigma_{Hub} + 3k_1 \int \sigma_{root}(x) dx + (F(\theta_{Rot}) + F(\theta_{Rot} + 120) + F(\theta_{Rot} + 240)) \int \sigma_B(x) dx \quad (16)$$

where the function F maps the effect of the blade pitch angle θ_p into the blade RCS contribution to the rotor RCS as a function of the turbine rotation angle θ_{Rot} for three turbine blades spaced 120 degrees apart. The turbine operating principles infer that F is a function of both rotation angle and wind speed and may be a function of the detailed blade design. Although equation (11) provides an observed example, there is insufficient evidence to pursue a reasonable model for F .

When the rotor is viewed at yaw angle $\pm 180^\circ$ the rotor hub is screened by the turbine nacelle. Simulation studies reported in [21] suggest that the RCS peak for the back of the rotor is shifted approximately 5° in rotation angle but is very similar in form to the rotor face RCS peak. Since no other data has been found, the model will assume that the functional form of the rotor radial distance dependence is the same for the front and back face of the rotor.

The radial distance dependence of the turbine face model is based on inadequate data and, until verified, must be considered to be speculative. It has limited value for the estimation of terrain screening effects for turbine yaw angles close to the turbine axis. The rotation angle dependence of the total rotor RCS is based on measurements and is considered to be reliable.

For now, the radial dependence discussion for turbine face observations is considered to be a place-holder and has not been included in the turbine RCS model scripts.

4.2.4 Yaw and pitch angle effects for turbine rotor RCS

Since the turbine blades are only visible to an ASR when they are in a nearly vertical position for all yaw angles except those close to 0° yaw, the width of the Doppler spectrum can be calculated from the turbine rotation rate ω , exposed (part of the blade may be masked by terrain) blade radius distance R and yaw angle θ_Y as shown in equation (10).

When the turbine is not close to 0° yaw angle (the rotor is viewed face on at yaw angle 0°) the turbine rotor RCS is dominated by the radar returns from the blades and hub. The vertical blade RCS peaks can be used to modulate a scale factor that adapts the turbine RCS results to yaw angle. At some rotor yaw angles the turbine blade RCS will be reduced by more than 30 dB. For the Enercon E66 turbine, the lowest rotor RCS is observed at yaw angles between -30° and -70° , 20° and 70° , 110° and 160° , 170° and 190° , and between 240° and 250° . Examination electromagnetic scattering model results [15] shows that these low RCS features depend on the blade design used in the turbine and cannot be generalized to all turbine types. If the turbine type and blade design are known, prediction of high blade RCS and low blade RCS yaw angles may be possible.

The turbine yaw angle is controlled by the local wind direction to within $\pm 10^\circ$. Wind direction measurements are usually made by sensors that are mounted on the top of the turbine nacelle. If the local wind direction at the turbine site is known, the rotor angle with respect to the radar observation vector can be predicted to within the $\pm 10^\circ$ tolerance. Since the local terrain influences the wind direction at the turbine site, coarsely gridded wind direction data is mainly useful for turbine RCS predictions in a statistical sense. These predictions can be tuned using ASR observation data if wind direction and yaw pointing reporting capability is implemented.

Model calculations for an Enercon E66 turbine blade [14] show that the effect of the blade pitch angle is to shift the apparent yaw angle position of blade RCS peaks by the blade pitch angle when the yaw angle is near 0° and $\pm 180^\circ$.

Unfortunately the blade-model results in [14] are insufficient to model the yaw angle dependence of the turbine rotor so that the dynamic rotor RCS features can be extended beyond the $\pm 90^\circ$ yaw used for their definition. Various studies show that the turbine rotor cross section with one blade in the vertical orientation varies with yaw angle. All sources agree that the rotor RCS is largest when the rotor is viewed from the front at 0° yaw. The yaw scattering pattern shown in Figure 78 of [22] for a 2.8 GHz radar suggests that the rotor RCS at 0° yaw is at least 7 dB larger than the rotor RCS at 90° yaw. This reference shows a highly structured, somewhat asymmetric scattering pattern as the yaw angle is varied over 360° . Figure 78 in [22] cannot be reproduced well and has been enhanced by red dots that mark the prominent scattering peaks in Figure 42 to illustrate an example of the yaw dependence of a turbine rotor RCS. Note that blade shape effects are clearly seen in Figure 42.

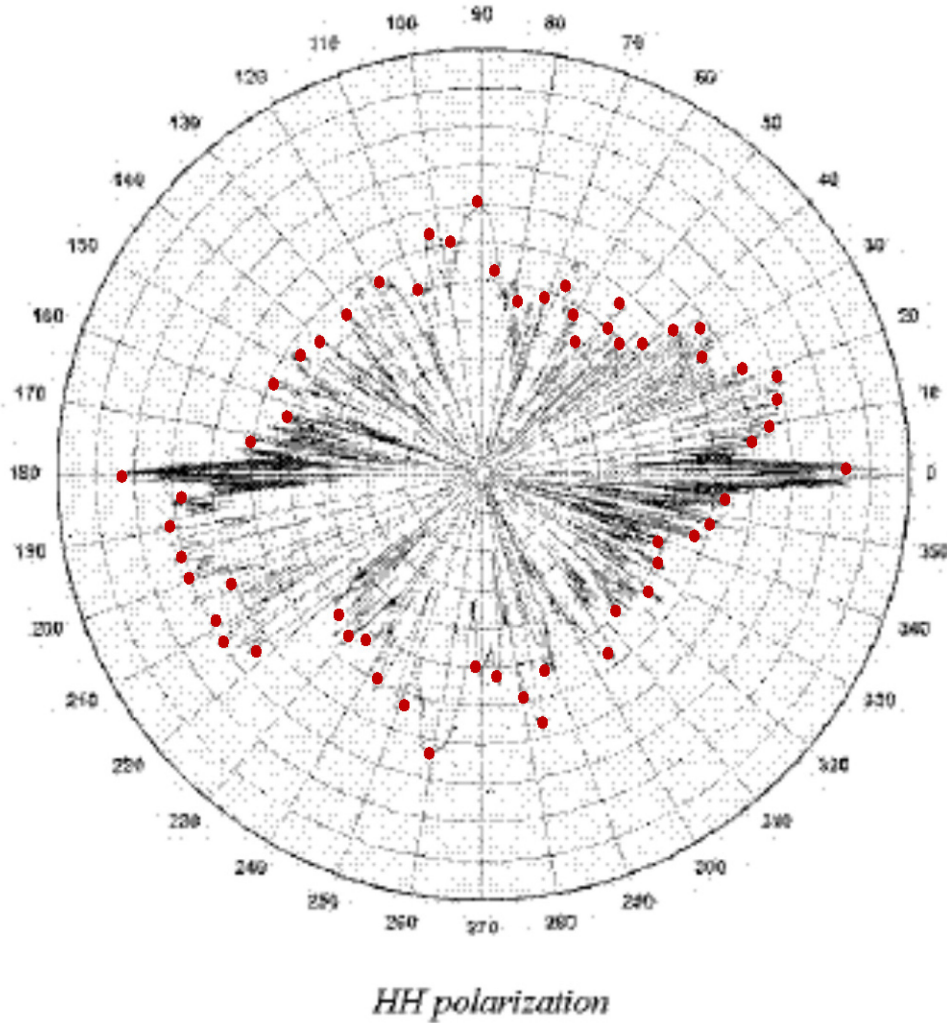


Figure 42: Rotor RCS for a 126 m diameter turbine as a function of yaw angle when one blade is vertically up from [22] Figure 78.

Image credit: reference [22].

In Figure 42, the ring spacing is 5 dBm^2 and the outer ring is 55 dBm^2 and the radial grid lines are stepped by 10° . Figure 42 is based on model calculations for a 126 m diameter rotor with fiberglass blades. The effects of the internal spar structure are included but the rotor hub and nacelle and the tower are not. Table 5 displays an RCS step approximation to the data in Figure 42 and includes the scattering pattern asymmetries between the positive and negative yaw angles on the $\pm 180^\circ$ yaw angle scale.

Table 5: Normalized yaw dependence of the turbine blade RCS.

Yaw angle range	Relative RCS (dBm ²)	Notes
$-1^\circ \leq \text{yaw} < 0^\circ \mid 0^\circ \leq \text{yaw} < 1^\circ$ and $-179^\circ \geq \text{yaw} \mid \text{yaw} \geq 179^\circ$	0	Rotor front and rear faces (three blades)
$1^\circ \leq \text{yaw} < 32^\circ$	-7.0	Airfoil top and bottom minimum curvature surfaces
$32^\circ \leq \text{yaw} < 40^\circ$	-12.0	
$40^\circ \leq \text{yaw} < 85^\circ$	-17.5	Maximum curvature airfoil top surface
$85^\circ \leq \text{yaw} < 95^\circ$	-8.0	Airfoil leading edge
$95^\circ \leq \text{yaw} < 179^\circ$	-17.5	High-pressure (concave) blade surface
$-179^\circ < \text{yaw} \leq -140^\circ$	-6.0	
$-140^\circ < \text{yaw} \leq -105^\circ$	-18.0	
$-105^\circ < \text{yaw} \leq -95^\circ$	-8.0	Airfoil trailing edge
$-95^\circ < \text{yaw} \leq -1^\circ$	-18.0	High-pressure (concave) blade surface

Noting that blade design and materials choice will make scattering patterns (similar to that shown in Figure 42 for different blades) somewhat different, there will be common features that can be used to create a crude, empirical model (RCS error ≤ 5 dBm²) of the yaw angle dependence of the turbine blade RCS. From Figure 42 with the yaw angle mapped into the range $-180^\circ \leq \text{yaw} < 180^\circ$, the symmetrized yaw effects on the blade RCS follow the pattern shown in Table 6 and Figure 43.

Table 6: Symmetrized yaw dependence of the turbine blade RCS.

Yaw angle range	Relative RCS (dBm ²)	Notes
$-1^\circ < \text{yaw} < 0^\circ \mid 0^\circ < \text{yaw} < 1^\circ$ and $-179^\circ > \text{yaw} \mid \text{yaw} > 179^\circ$	0	Rotor front and rear faces (three blades)
$1^\circ \leq \text{yaw} < 40^\circ$ and $-179^\circ \leq \text{yaw} < -140^\circ$	-7.5	Airfoil top and bottom minimum curvature surfaces
$40^\circ \leq \text{yaw} < 85^\circ$ and $-140^\circ \leq \text{yaw} < -95^\circ$	-17.5	Maximum curvature airfoil top and bottom surfaces
$85^\circ \leq \text{yaw} < 95^\circ$ and $-95^\circ \leq \text{yaw} < -85^\circ$	-8	Airfoil leading and trailing edges
$95^\circ \leq \text{yaw} < 179^\circ$ and $-85^\circ \leq \text{yaw} < -1^\circ$	-7.5	

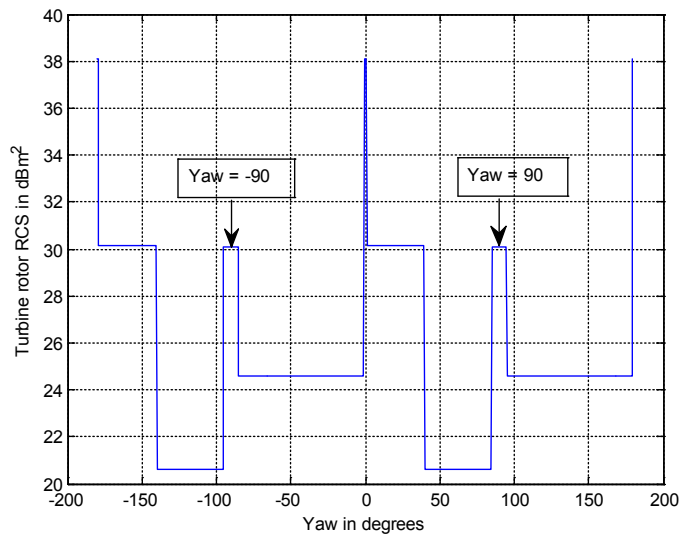


Figure 43: Simplified rotor RCS yaw dependence from Table 5 scaled for the Enercon E66 turbine.

Since yaw dependence data comparable to Figure 42 have not been found, the simplified model shown in Table 6 and Figure 43 was used to define the yaw dependence of the turbine rotor RCS. Comparing Figure 43 to the gross features of Figure 42, the asymmetries of Figure 42 are absorbed into the 5 dB tolerance range of the model except for the 10° shift in the -90° peak. The RCS peaks for rotor edge views are symmetrized in Figure 43 and in the current turbine model since the peak position asymmetry in Figure 42 is not supported by comparable data.

Although the yaw angle dependence of the rotor hub, blade and blade-tip features are probably different, from the blade model there are no data to support this. In the model, the yaw angle weighting is applied to the rotor RCS scale factor that converts the normalized rotor RCS to m^2 . If better data are found, the model can be easily amended. Annex C contains wind turbine rotor cross-sections and power spectra for yaw angles between -10° and -170° that are based on the current yaw RCS model.

Noting the relationship between wind speed and turbine rotation rate the turbine RCS observed by an ASR appears as a time series of radar return amplitude flashes. For terrestrial wind farms, the wind speed and direction at the turbine nacelle height are not uniform but varies over the site and can be influenced by the wakes of up-wind turbines. Some statistical models will be needed to simulate the speed and yaw angle distribution of turbines in the wind farm. Noting that the turbine yaw angle is set to within $\pm 10^\circ$ of the mean, local wind direction² the turbine yaw angle can be estimated from the wind direction with respect to the radar bearing of the turbine plus a random fraction of the $\pm 10^\circ$ control range.

Table 7 summarizes the elements of a simple turbine interference model that could be used for first-order evaluation of wind farm effects.

² [22] shows that a 60 second moving average wind direction and $\pm 8^\circ$ yaw drive onset error provide optimum results when yaw motor cycle time is included.

Table 7: Selected model parameters.

Parameter	Source parameters	Model representation	Scaling
Yaw angle	Wind direction and radar bearing	Computed angle plus a random angle in the $\pm 10^\circ$ range $\theta_Y = (\theta_{wind} - \phi_{turb} + 180)$	none
Turbine rotation rate	Wind speed and turbine rotation specifications	$\omega = \frac{\omega_{Rated} - \omega_{start}}{V_{Rated} - V_{cut-in}} V_{Wind}$	none
Dopper bandwidth	Blade length, tower height, terrain mask height and rotation rate	$B_{Dop} = \omega \frac{R - R_{min}}{\lambda} \sin(\theta_Y)$	none
Maximum and minimum Doppler frequencies	Blade length, tower height, terrain mask height and rotation rate	$f_{max} = 2\omega \frac{R}{\lambda} \sin(\theta_Y)$ $f_{min} = 2\omega \frac{(H - h) - R}{\lambda} \sin(\theta_Y)$ $0 < H - h \leq R$	none
Tower height H	Turbine specifications	H	none
Tower RCS	Tower height and reference data	$A_{Tower} = 100 \left(\frac{H}{67} \right)^2$	Tower height ratio squared
Terrain mask height	Tower location, radar location, illumination geometry	h	none
Nacelle RCS	Reference models, nacelle type, rotor hub diameter	$A_{Nacelle}$ $= A_{Reference} \left(\frac{D_H}{D_{Reference}} \right)^2$	Hub diameter ratio squared
Rotor RCS	Reference model, turbine hub height, terrain mask height	Normalized reference model tables, $A_{Blade} =$ $A_{Blade_ref} \left(\frac{L}{33.5} \right)^2$	Blade length squared

4.2.5 Terrain height masks

In practical situations, wind turbines are often partially screened from the ASR field of view by intervening terrain features and vegetation. This model does not compute the screened height above ground at the turbine locations but contains a module that uses an imported, screened height at a turbine base location to compute screening effects on the static and dynamic turbine RCS. The symbol σ_X is used to represent the RCS for component X.

The terrain mask module re-expresses the turbine component modules in terms of their height above ground at the turbine location in preparation for the masking calculations so that:

1. When the mask height $h = 0$ the turbine RCS in m^2 is:

$$\begin{aligned}\sigma_{Turbine} = & \sigma_T + \sigma_N + \int_{R_T}^{L_B} (\sigma_{TFd}(R) + \sigma_{TFu}(R))dR \\ & + \int_{R_H}^{L_B} (\sigma_{Bd}(R) + \sigma_{Bu}(R))dR + 2 \int_0^{R_H} \sigma_H(R)dR\end{aligned}\quad (17)$$

where:

- L_B is the rotor radius
- σ_T is the tower RCS,
- R_T is the minimum radius of the blade tip feature,
- R_H is the hub radius,
- $\sigma_{Turbine}$ is the turbine RCS,
- σ_N is the nacelle RCS,
- σ_{TFd} is the blade tip feature RCS per unit length for the blade down,
- σ_{TFu} is the blade tip feature RCS per unit length for the blade up,
- σ_{Bd} is the blade RCS per unit length for the blade down,
- σ_{Bu} is the blade RCS per unit length for the blade up, and
- σ_H is the hub RCS per unit radius.

The following conventions are used in the turbine masking calculations:

- i. The turbine nacelle rests on the top of the tower and has height HN.
- ii. The tower height is HT.
- iii. The center of the turbine hub is the turbine rotor axis and is at height HH = HT+HN/2.
- iv. The functions σ_{TFd} , σ_{TFu} , σ_{Bd} , and σ_{Bu} are defined in terms of distance from the blade root.
- v. The function σ_H is defined in terms of distance from the hub axis.

When no terrain masking is present, the turbine Doppler power spectrum occupies the Doppler frequency range $-\frac{2\omega L_B}{\lambda} \sin(\theta_Y) < f < \frac{2\omega L_B}{\lambda} \sin(\theta_Y)$, where ω is the turbine rotation rate in radians per second and λ is the radar wavelength. The turbine is assumed to rotate clockwise as viewed from the rotor face at yaw angle 0° . The relationship between the sign of the power spectrum components that correspond to the blade up or down orientations depends on the yaw angle of the turbine axis with respect to the observing radar.

- For $5^\circ < \text{yaw} < 175^\circ$ radar returns from the upper blade positions are found in the positive spectral frequency interval and radar returns from the lower blade positions are found in the negative frequency interval.
 - For $-5^\circ < \text{yaw} < -175^\circ$, the relationship between the blade positions and the sign of the spectral frequency interval is reversed.
2. When $h < H_H - L_B$ only the tower RCS is affected by the terrain mask:

$$\sigma_{Tm} = \sigma_T \left(\frac{H_T - h}{H_T} \right)^2 m^2. \quad (18)$$

3. When $H_H - L_B \leq h < H_H - R_T$, the tower, blade tip feature and the blade RCS are affected as is the maximum Doppler shift for the downward pointing blade. For $-175^\circ \leq \text{yaw} < -5^\circ$ positive Doppler frequency components are affected. For $5^\circ \leq \text{yaw} < 175^\circ$ negative Doppler frequency components are affected. The partially masked tower RCS is given by equation (18). The partially masked blade-tip feature and blade RCSs are:

$$\sigma_{TFm} = \int_{R_T}^{H_H - h} \sigma_{TF}(R) dR \text{ and} \quad (19)$$

$$\sigma_{Bm} = \int_{R_H}^{H_H - h} \sigma_{Bd}(R) dR \text{ m}^2. \quad (20)$$

All other turbine RCS components are not affected. The maximum absolute value of the Doppler frequency f_{Dd_m} of the downward blade is:

$$f_{Dd_m} = \frac{2\omega(H_H - h)}{\lambda} \quad (21).$$

4. When $H_H - R_T \leq h < H_H - R_h$ the blade tip component (if present for the downward blade) has been removed. The residual tower RCS is given by equation (18). The downward residual blade RCS is given by equation (20). The maximum absolute value of the Doppler frequency of the downward blade is given by equation (21). All other turbine RCS components are unaffected by the terrain mask.
5. When $H_H - R_H \leq h < H_H$ the downward blade and tower RCS have been removed and the lower half of the hub is filtered by the terrain mask. The downward rotor RCS is:

$$\sigma_{Hm} = \int_0^{H_H - h} \sigma_H(R) dR \quad (22)$$

and the residual nacelle RCS is:

$$\sigma_{Nm} = \sigma_N \left(\frac{H_N - h + H_H}{H_N} \right)^2 . \quad (23)$$

The magnitude of the lower rotor Doppler frequency has the maximum value given by equation (21). All remaining rotor RCS components are unaffected.

6. When $H_H \leq h < H_H + R_H$, all of the lower rotor RCS components have been removed and the upper hub and nacelle RCS values are reduced by the terrain shadowing filter. The residual nacelle RCS contribution is given by equation (23) and the residual hub RCS is given by:

$$\sigma_{Hm} = \int_0^{h-H_H} \sigma_H(R) dR . \quad (24)$$

No lower rotor Doppler components remain and the magnitude of the maximum upper rotor Doppler frequency is:

$$f_{Dd_m} = \frac{2\omega L_B}{\lambda} . \quad (25)$$

The previously defined Doppler spectrum sign conventions apply.

7. When $H_H + R_H \leq h < H_H + R_B$ The turbine hub no longer contributes to the turbine RCS and only the residual nacelle contribution given by equation (23) (for $h - R_T - H_N < 0$) and the upper blade and blade tip features remain. The turbine RCS now becomes:

$$\sigma_{Turbine} = \int_{h-H_H}^{L_B} \sigma_{Bu}(R) dR + \int_{R_T}^{L_B} \sigma_{TFu}(R) dR + \sigma_{Hm} . \quad (26)$$

8. When $h > H_H + L_B$ the turbine is fully screened by the terrain mask and no components remain.

Due to uncertainties in the RCS radial dependence model, the terrain screening mask effects for the front and rear turbine rotor faces have not been developed into a software module but, when developed, will follow a similar pattern to the discussion above.

The Matlab script version of the terrain mask filter algorithm is introduced in Annex B.2.4. When a wind turbine is partially masked by terrain, ASR observations of the turbine interference capture the blade-up and blade-down conditions at different times. Figure 44 displays the turbine RCS as a function of terrain mask height for an Enercon E66 turbine on a 67 m tower for the blade-down condition at yaw angle -90° .

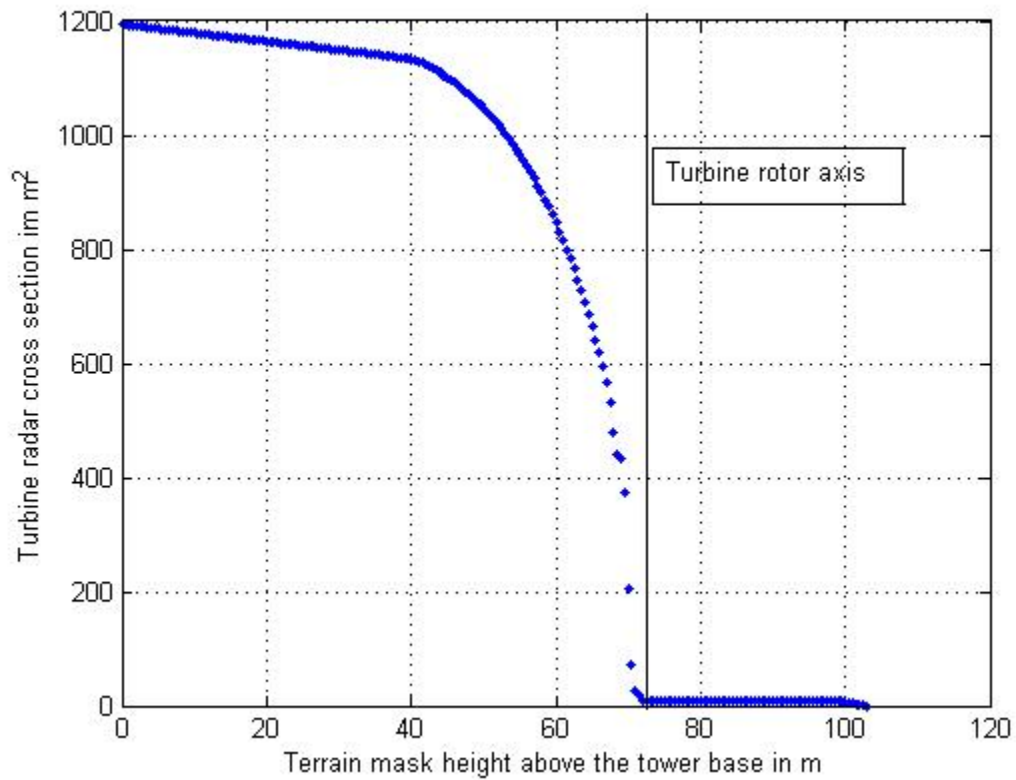


Figure 44: Enercon E66 turbine radar cross section in m^2 for -90° yaw as a function of terrain mask height at the turbine base when the turbine blades are vertically down.

Figure 45 displays the blade-up turbine RCS in m^2 for the same turbine and terrain mask height.

As the terrain mask rises to cover the turbine rotor, the Doppler frequency returns from the masked portion of the rotor are removed and the Doppler bandwidth of the turbine signature decreases with mask height. The Doppler frequency associated with the upper blade tip is present until the entire rotor is obscured by the terrain mask.

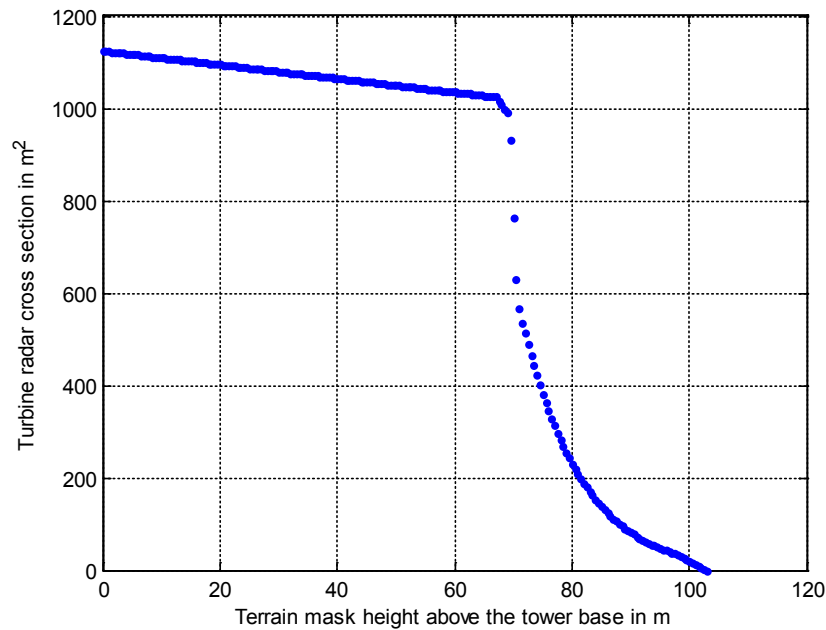


Figure 45: Enercon E66 turbine radar cross section in m^2 for -90° yaw as a function of terrain mask height at the turbine base when the turbine blades are vertically up.

Figure 46 illustrates the Doppler signature effect as a function of mask height for the reference Enercon E66 turbine viewed at yaw angle -90° when the rotor is turning at 16 RPM.

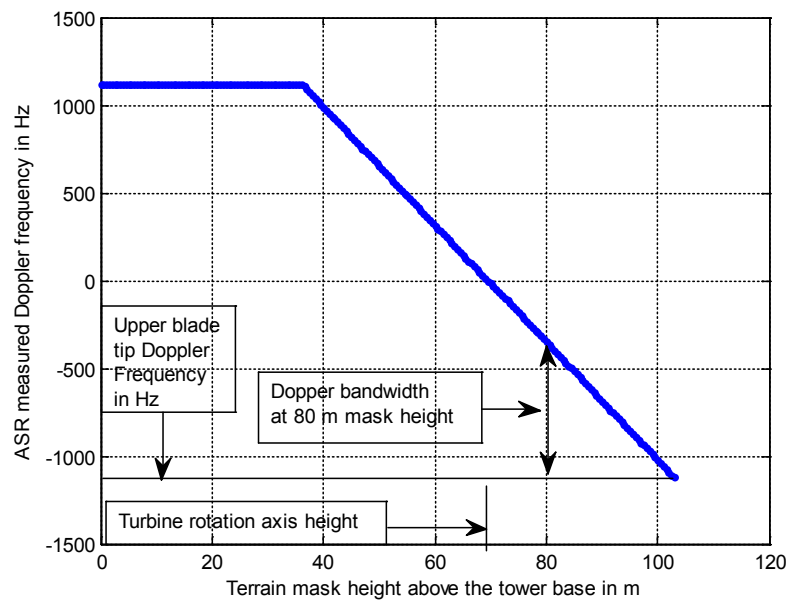


Figure 46: Doppler returns from an Enercon E66 turbine viewed at -90° yaw when the turbine is turning at 16 RPM as a function of terrain mask height in m.

4.3 Wind turbine RCS model implementation

The wind turbine RCS and Doppler frequency model discussed in Sections 4.1 and 4.2 have been implemented as Matlab scripts. To facilitate model refinements, the model is implemented in a modular fashion and the code contains detailed annotations.

The major code modules are:

1. the turbine RCS model,
2. a two-pole high-pass filter model,
3. a turbine Doppler spectrum display routine, and
4. a terrain shadow mask model.

The Matlab code implementation is structured as a developmental tool that can be easily modified when more and better information becomes available. Coherent interference effects are not included in this version. The developmental code has not been optimized for computational efficiency.

The turbine RCS model uses data from modeling and measurements of an Enercon E66 turbine as presented in [15] to generate the reference case. The Vestas V47 nacelle data from [15] are used to model the effects of rectangular form-factor nacelles. Simple scaling laws discussed in Section 4.2 are used to generalize the reference data to other systems.

The RCS model code is structured as an input section that can form a model for data input to an operational version, followed by turbine model calculation blocks. The nacelle RCS calculation parameters are discussed in Section 4.1.2 and are developed in Annex B1. The turbine rotor calculations are based on Figure 34, Table 3 and Table 4. The yaw angle dependence of the Rotor RCS is based on Figures 42, 43 and Table 5. For lack of more detailed information, these are applied to the turbine RCS scale factor. The model code computes the rotor RCS as hub, blade and blade-tip feature components which are summed at the end of the calculation to generate the rotor RCS. The model code has been designed so that the turbine RCS model must be run first since all other model components use matrices that are generated by this script.

Since the RCS models for the turbine front and rear face views (Section 4.2.3) are highly speculative at this time no code was developed for these cases.

The high-pass filter, Doppler spectrum display and terrain shadow mask modules can be run in any order following the RCS model execution.

The high-pass filter module was designed to emulate a simple ASR zero-Doppler rejection filter to remove static RCS components from the computed data. This module can be replaced by any other filter by adapting the filter code to the input variables.

The Doppler spectrum display module uses Doppler frequency and RCS data generated by the RCS module to transform the radius-rotational angle coordinates to radius-frequency coordinates and map the input data into an image format.

The terrain shadow mask model generates a set of shadow mask heights that scans the entire turbine to generate Figures 44, 45 and 46. To use the model for a specific input mask height, the mask height generation loop can be disabled and the input parameters can be ingested. The core of the module parses the turbine into tower and nacelle static components and further parses the rotor into blade-up, blade-down, blade tip feature and hub components for the terrain masking calculations. Both positive and negative yaw angles are accepted.

5 Wind-farm arrays of wind turbines

ASRs seldom have a single wind turbine in their field of view but more commonly see a wind farm (an array of wind turbines) that occupy a number of range bins over one or more scan angle intervals. Since the wind turbines are individually controlled, their motions and orientations are not synchronized and respond to local wind conditions at the top of each nacelle. Oceanic wind farms frequently use a rectangular array of turbines. Terrestrial wind farm turbine distributions are determined by land availability and by terrain surface relief and are seldom regular.

Taken alone, each wind turbine extracts energy from the incident wind and results in a reduction in wind speed within its wake structure. Since the turbine blades are airfoils that use a lift force to turn the turbine rotor, they have a net circulation flow that results in spiral, down-stream wing-tip vortices in the turbine's wake [26]. The tip vortices remain distinct near the wind turbine and degrade into a larger scale turbulent structures in the turbine wake within down-stream distances comparable to approximately 5 rotor diameters [26], [27].

Observations from the Horns Rev wind farm in Denmark reported by Schmits [28] and shown in Figure 47 demonstrate wind turbine wake and turbulence persistence over long distances. The wakes in Figure 47 are visible because the atmospheric dew point allowed the formation of vapor contrails in the wakes. The structure of the condensation trails in Figure 47 clearly show that the turbine wakes expand in the down-wind direction and that local wind direction varies down the wake. Wake model considerations can be found in [26] and [27].

Studies of Danish wind farm arrays [29] and [30] have reported significant variation in wind speed and direction at down-wind turbines that fall into the wakes of upwind turbines. Downwind power reductions of up to 30% were observed at the 8th turbine in a wind-aligned row and maximum power reductions of up to 25% were observed at the first down-wind turbine in a row [29]. Extreme turbine efficiency reductions of up to 40% were reported for turbines that were located in the center of a wake. These observations were made in regularly gridded ocean turbine arrays.

A comment in [27] notes that the wake turbulence structure degrades more rapidly over forested areas than it does over oceans or smooth terrain. Results for complex terrain noted in [30] do not support this conjecture but the terrain cover in the contradicting report was not described.

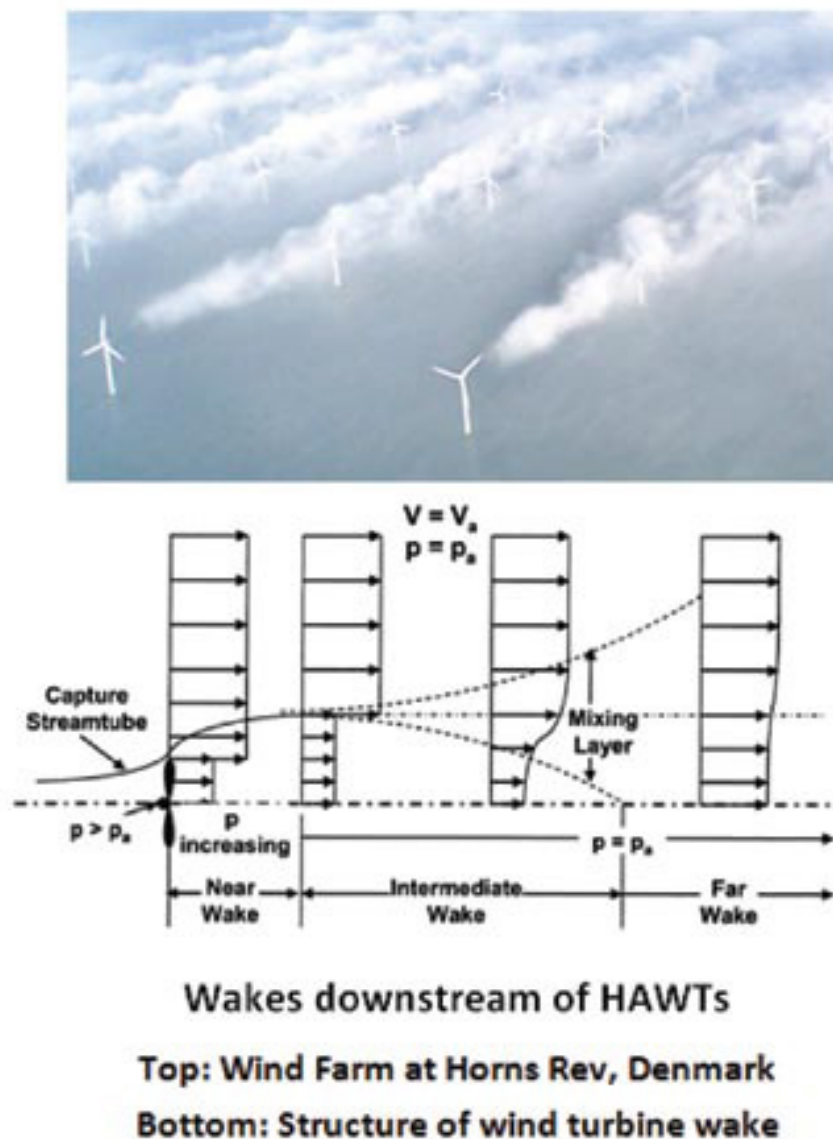


Figure 47: Wind turbine wakes in an ocean wind farm under favorable atmospheric conditions.

Illustration credit: reference [28].

An illustration of the wake interaction effect is provided from data delivered by the Wolfe Island (eastern Lake Ontario at the start of the St. Lawrence river) wind farm operator, TransAlta Inc. in support of a DRDC project that was examining space-based SAR-GMTI signatures of wind turbines. Figure 48 shows the locations of the Wolfe Island turbines. The land area containing the turbines has low relief (a few metres) with primarily agricultural terrain cover.

Data for 45 (of 86) wind turbines that fell within the DRDC study area are presented in Table 6 for October 9, 2009 at approximately 23:02 UTC (18:02 local time). From Table 6 and Figure 48 turbines 3, 4, 6, 7, 15, 17, and 18 are on the windward side of the array and are unaffected by the

wakes of other turbines. The mean wind speed estimated by the turbine anemometers was 6.09 ± 0.32 m/s and the mean yaw angle reported by the turbines was $252.7^\circ \pm 7.4^\circ$. Part of the standard deviation in the wind direction is the yaw-steering dead-band of approximately $\pm 10^\circ$ and part of the standard deviation will be wind direction change. Regression analysis indicates a 10° yaw angle trend over the length of the windward turbine array (and/or over the yaw angle estimate integration time at each turbine). Although the wind speed appears to be stable, the wind direction changes over the observed windward turbine data. Wolfe Island meteorological data for October 9 show the wind speed to be 6.4 m/s and the wind direction to be 252° at the turbine rotor height at 12:00 EST.

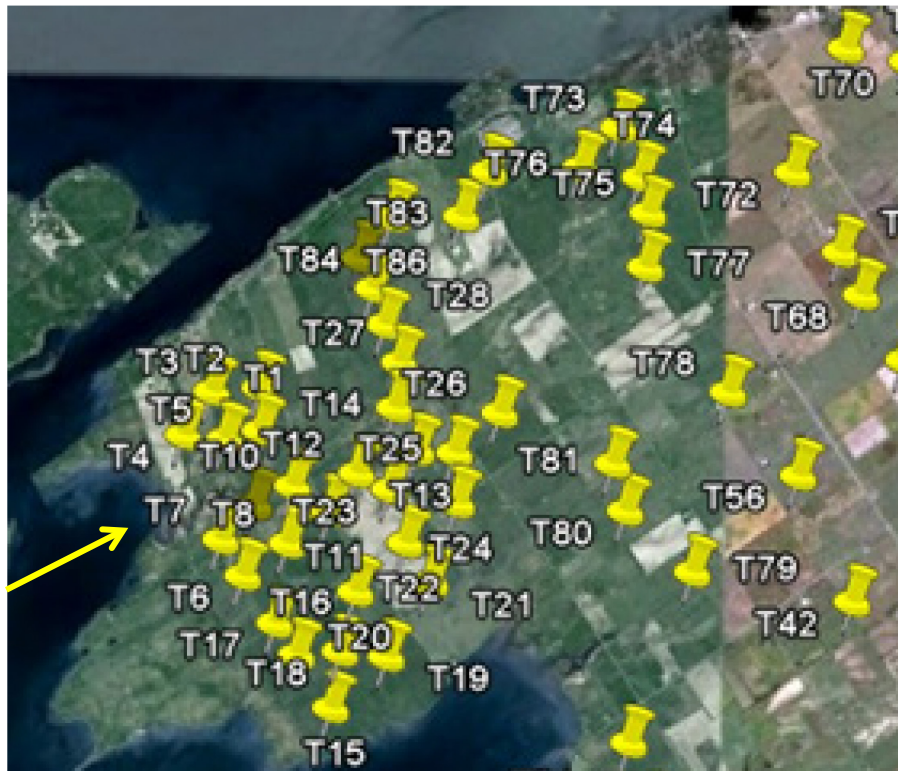


Figure 48: Wolfe Island wind farm turbine locations corresponding to Table 6. The yellow arrow indicates the approximate wind direction.

From Table 8 and Figure 48 turbines 1, 5, 8, 10, 11, 12, 16, 19, 20, 22, and 23 lie just down-wind of the windward row and some of these are positioned to be affected by the wakes of the windward turbines. Looking at the parameters reported by this second set of turbines we see that the average measured wind speed was 5.36 ± 0.973 m/s and the mean turbine yaw angle was $251.5^\circ \pm 43.4^\circ$. Although the available data are not suited to providing definitive answers, the yaw angle standard deviation indicates a probable turbine wake influence on down-wind turbines and further indicates that yaw angle predictions based on uniform wind speed and directions are not suitable for estimating wind farm impacts on ASRs.

Table 8: Wolfe Island wind turbine operating condition measurements for October 9, 2009 at 23 h UTC.

Date	Time	Name	WindSpeed	YawAngle	RotorRPM
09/10/2009	2301710	T01	5.9215	332.899	10.81017
09/10/2009	2301977	T02	5.520534	13.02254	9.177295
09/10/2009	2301947	T03	6.234167	247.7458	10.70983
09/10/2009	2301948	T04	6.143667	255.1082	10.91167
09/10/2009	2301544	T05	5.6925	308.0208	10.3045
09/10/2009	2301869	T06	5.9995	241.1193	11.3925
09/10/2009	2301986	T07	5.585643	252.5631	10.54474
09/10/2009	2301953	T08	5.136333	271.7507	9.4085
09/10/2009	2301964	T09	6.136167	231.1748	10.2925
09/10/2009	2301966	T10	3.3625	237.252	7.521167
09/10/2009	2301968	T11	5.803167	221.5487	9.221333
09/10/2009	2301713	T12	5.729667	229.1392	10.33583
09/10/2009	2301553	T13	4.975667	258.6583	8.782333
09/10/2009	2301546	T14	5.310833	293.214	9.293667
09/10/2009	2301698	T15	5.8655	243.3218	11.46333
09/10/2009	2301705	T16	5.809333	174.2795	11.25483
09/10/2009	2301716	T17	6.2265	261.4657	11.36067
09/10/2009	2301972	T18	6.575	249.2377	11.799
09/10/2009	2301700	T19	6.275167	265.3517	11.1305
09/10/2009	2301706	T20	6.132167	244.3748	11.20517
09/10/2009	2301547	T21	5.285167	72.55933	9.2015
09/10/2009	2301711	T22	5.4895	261.6543	9.3105
09/10/2009	2301699	T23	3.618333	225.5983	8.009667
09/10/2009	2301957	T24	5.400333	235.5557	9.241667
09/10/2009	2301697	T25	3.498833	233.2475	7.730667
09/10/2009	2301870	T26	4.445	254.1098	7.748167
09/10/2009	2301975	T27	4.144	192.4118	7.831667
09/10/2009	2301868	T28	4.234558	197.6489	8.316528
09/10/2009	2301550	T42	6.564833	244.183	11.93
09/10/2009	2301965	T56	6.197167	256.0848	11.05067
09/10/2009	2301867	T73	5.33	222.78	9.672833
09/10/2009	2301709	T74	5.389167	192.5955	9.071
09/10/2009	2301971	T75	4.488167	354.8863	8.213167
09/10/2009	2301951	T76	5.611667	216.3762	9.147667
09/10/2009	2301973	T77	5.091167	257.0658	8.864333
09/10/2009	2301960	T78	4.329167	280.1597	7.9105
09/10/2009	2301549	T79	6.833667	244.429	12.23583
09/10/2009	2301715	T80	6.206167	232.6428	11.52717
09/10/2009	2301979	T81	4.780667	344.1662	8.607333
09/10/2009	2301712	T82	5.210351	186.2097	9.027713
09/10/2009	2301959	T83	5.306167	246.3243	9.605
09/10/2009	2301714	T84	5.679667	288.2447	10.36567
09/10/2009	2301717	T85	6.1365	238.6875	11.06517
09/10/2009	2301704	T86	5.4045	209.7635	10.975
		MEAN =	5.434324	239.0598	9.854067
		STD =	0.827756	57.88357	1.331597

When all 45 turbines in Table 8 are considered, the turbine interaction effects on the wind speed and yaw angle measurements and on the statistical variability of these measurements are evident when the relative turbine positions are examined in the context of the incident wind field. The

Wolfe Island wind farm manager has noted that yaw angle variations over the turbine array typically vary at least $\pm 15^\circ$ ³ even when the ambient wind-field is uniform at the site.

The good news for wind farm impacts on ASR performance is that worst case that has coordinated turbine interference is very unlikely. When model calculations are used to predict the impact of a proposed wind farm on an ASR, only the up-wind turbines will respond to the undisturbed ambient wind speed and direction. Model calculations for turbines that lie within predicted wake structures need to use appropriately randomized wind speed and direction perturbations to the ambient wind field to estimate their probable ASR impacts.

³ Data provided in [31] show that typical mean yaw pointing errors are in the range $\pm 12^\circ$ to $\pm 15^\circ$ and typical RMS errors are in the range $\pm 16^\circ$ to $\pm 21^\circ$ for 2 MW turbines in Alberta.

6 Conclusions and summary

To estimate the effects of wind turbines on ASR performance we treat the wind turbine as a complex target that resides in a single ASR range cell and we assume that the radar range to the wind turbine is large enough that the radar pulse wave front is approximately planar at the wind turbine. For these assumptions, all radar reflections from the turbine will add coherently at the radar and coherent fading effects will be present. Estimation of coherent fading requires a detailed model of the turbine structure, and the electromagnetic wave reflection distribution over the turbine components. This information is not available and will be specific to each turbine that is being observed. To estimate the gross properties of wind turbine scattering, we use an incoherent sum (RCS estimate sum) over each wind turbine component and combine these in an incoherent fashion to create a target RCS estimate that will provide a characterization of the mean radar properties of the target for a given set of wind and radar look direction conditions. The incoherent sum approach will under-estimate coherent sum RCS peaks by as much as 3 dB and will overestimate the RCS corresponding to coherent fading nulls.

The discussions in this document provide an S-band, first-order target RCS estimate that has been based on published measured data and detailed electromagnetic scattering models to the greatest degree possible. The model looks at horizontal-axis wind turbines that deliver between 0.6 and 5 MW of power at their rated operating conditions. The model uses local wind speed and wind direction to determine the turbine rotation rate and the turbine axis pointing direction and uses the axis pointing and the radar bearing to estimate the turbine yaw angle as seen by the ASR. The model assumes that the turbine responds to the local wind field as measured by sensors on the turbine nacelle.

The model presented in this report can be used as a template for more detailed work as primary data become available. In its present form it can be used to characterize the expected influence of wind turbines and turbine arrays on ASRs and can be tuned to estimate probable interference of existing wind turbines on existing ASRs from environmental conditions.

Wind turbines are modeled as a set of components consisting of:

1. the turbine tower,
2. the turbine nacelle,
3. the rotor blades and
4. the rotor hub.

All components are scaled to reference models using the dimensions of the reference and the turbine to be modeled to determine RCS scale factors.

Wind turbine towers are assumed to be tapered cylinders made of concrete or steel and have an RCS that is proportional to the 67 m tower used for the Enercon E66 turbine located at Swaffham UK. The tower RCS is assumed to scale as the square of the ratio of the tower height to the height

of the Swaffham tower. For terrain screening the tower RCS estimates are based on the unscreened height.

Two turbine nacelle models are used to estimate the nacelle RCS as a function of yaw angle. Rounded profile nacelles are assumed to have an RCS proportional to the RCS of an Enercon E66 nacelle. Rectangular, flat sided nacelles are assumed to have RCSs proportional to the Vestas V47 nacelle RCS. The nacelle RCS is assumed to scale as the nacelle area which is assumed to vary as the square of the turbine hub diameter.

The turbine tower and nacelle RCS are static (zero Doppler) RCS contributions to the target signature seen by an ASR.

A three-bladed turbine rotor is assumed and the rotor was modeled as a hub component and blade components. The rotor RCS was modeled as a function of the radius distance from the turbine axis. The radial variation of rotor RCS was derived from a turbine Doppler spectrum that was measured at 90° yaw angle. The frequency variable was assumed to be proportional to radius distance from the rotor axis.

The turbine hub was modeled as a central core whose RCS is independent of turbine rotation angle and three blade root mounts whose RCS was given a nominal Gaussian decay with turbine rotation angle. A nacelle shadowing function was defined to account for hub screening by the nacelle as the yaw angle approaches $\pm 180^\circ$.

The turbine blades were modeled as radius varying RCS with a nominal Gaussian dependence on rotation angle. The argument of the Gaussian function was selected to attenuate the blade RCS by 20 dB at 5° rotation from a vertical position to yield behavior that has been reported in the literature. The blade model includes a blade-tip feature function (possible related to lightning protection structures) that has a Gaussian RCS decay with turbine rotation angle. The RCS of the blade-tip feature was extracted from the Doppler spectrum at 90° yaw. The form of the blade tip feature is expected to vary between turbine blade designs. Features of this type are observed in many reported turbine spectral histories.

Data from an Enercon E66 turbine were used to generate the model reference functions. Blade and hub components for other turbines are scaled by the squares of the hub diameter and blade length ratios.

The model sums the rotor RCS from all components and used the integral over the radius to create an RCS scale factor that is applied to the entire rotor. The Doppler signature of the rotor was modeled as a function of radius from the turbine axis.

The yaw dependence for the rotor RCS was based on electromagnetic scattering-model results for a different turbine and was simplified to capture the major features of the yaw relationship. Since the yaw dependence of the hub and blade structures are not known independently, the RCS yaw compensations was applied to the entire rotor. The report discusses an approach to modeling the conditions where the yaw angle is within $\pm 5^\circ$ of 0° and $\pm 180^\circ$ (front and rear faces of the rotor) but does not implement model calculations for these cases due to uncertainties in the set of assumptions that are required.

The model contains a terrain-screening mask that removes turbine components that fall within the mask. The mask height above the tower base is not calculated by this model but is accepted as input.

The turbine RCS and Doppler model was implemented as an internally-documented Matlab script that has been constructed in a modular fashion to allow easy adaptation to new and more reliable data. The script is divided into blocks containing:

- input parameters,
- static turbine components,
 - ♦ tower RCS and
 - ♦ nacelle RCS,
- dynamic turbine components,
 - ♦ hub RCS and Doppler frequencies,
 - hub core,
 - blade root,
 - ♦ blade RCS and Doppler frequencies,
 - blade,
 - blade-tip features, and
 - ♦ turbine RCS sum and scaling.

References

- [1] Martinez, J., Modelling and control of wind turbines, MSc thesis Imperial College London, 2007.
- [2] Preesapati, V. and Cotton, I., Lightning Protection of wind turbines – a comparison of real lightning strike data and finite element lightning attachment analysis, [http:// www.supergen-wind.org.uk](http://www.supergen-wind.org.uk), accessed April 16, 2013.
- [3] Nijssen, R., de Winkel, G.D. and Peeringa, J.M., WMC5MW laminate lay-out of reference blade for WP-3, Upwind Project WP3 contract report SES6, 2007
http://www.wmc.eu/UPWIND%20blade%20laminate%20layout_revision%201.pdf ,
accessed April24, 2013.
- [4] Stackpole, B., Sandia sizes-up wind turbine blade design,
http://www.designnews.com/document.asp?doc_id=23008, 2011, accessed April 15, 2013.
- [5] Wood, K., Wind turbine blades: Glass vs. carbon fiber, Composites Technology 2013,
<http://www.compositesworld.com/.../wind-turbine-blades-glass-vs-carbon-fiber>, accessed April 11, 2013.
- [6] Peeringa, J., Brood, R., Ceyhan, O. Engels, W. and de Winkel, G., Upwind 20 MW wind turbine pre-design, European Commission, ECN-E-11-017, 2011.
- [7] Jonkman, J., Butterfield, S., Musial, W. and Scott, G., Definition of a 5-MW reference wind turbine for offshore system development, National Renewable Energy Laboratory Technical Report NRE L/TP-500-38060, 2009.
- [8] Wind turbine control methods: National Instruments tutorial,
http://www.ni.com/white_paper/8189/en, accessed April 16, 2012.
- [9] Schubel, P.J. and Crossley, R.J., Wind turbine blade design, Energies 2012, P3425-3449.
- [10] Selvam, K., Individual pitch control for large scale wind turbines, Energy research Center of the Netherlands, report ECN-07-053, 2007.
- [11] Jenn, D. and Ton, Cuong, Wind turbine radar cross section, International Journal of Antennas and Propagation, V 2012.
- [12] Ohs, R.R., Skidmore, G.J and Bedrosian, G., Modelling the effects of wind turbines on radar returns, Military Communications conference 2010, San Jose, November 2010.
- [13] Bobillot, G., Boust, F., Langlet, S., Cheraly, A. and Phan, H.K., RADAR and wind turbines: Onera studies, http://enr-ee.com/.../user.../1_Bobillot_ONERA/Koordinierungstelle/pdf,
accessed April 22, 2013.

- [14] Poupart, G.J., Wind farms impact on radar aviation interests-final report, Department of Trade and Industry report DTI PUB URN 03/1294, 2003.
- [15] Wang, J., Brookner, E., Cornwell, P., Rerecke, M. and Farr, J., Modernization of en route surveillance radar, IEEE transactions on Aerospace and Electronic Systems, V. 48, No. 1, P. 103-115, 2012.
- [16] Thomsen, A.C.K., Marqversen, O., Pedersen, M.O., Moeller-Hundberg, C., Nielsen, E., Jensen, L.J. and Hansen, K., Air traffic control at wind farms with TERMA SCANTER 4000/5000, Proc. IEEE Radar Conference, Kansas City, P. 247-252, 2011.
- [17] ascSignal S-band air traffic control radar antenna system, http://ascsignal.com/files/radar/air_traffic/S-bandAirTrafficControlRadarAntennaSystem/pdf, accessed May 10, 2013.
- [18] Marcellin, J.-P., Cheraly, A., Petec, J.-F. and Phan, H.-K., Measurement of Doppler radar signature of wind turbines at high resolution in distance, Proc. EURAD'12 2012.
- [19] Wind turbines http://Twinkle-Toes_engineering.home.comcast.net, accessed June 18, 2013.
- [20] Lekou, D.J., Scaling limits and costs regarding WT blades, ESA Upwind Project: Integrated Wind Turbine Design, Contract Report SESE6 deliverable 3.4.3, 2010.
- [21] Frye, A, Neumann, C. and Muller. A., Compatibility of wind turbines with radars. Annual Report 2008, EADS Deutschland GmbH, 2009.
- [22] McDonald, J.J., Brock, W.C., Allen, S.E., Clem, P.G., Paquette, J.A., Patitz, W.E., Miller, W.K., Calkins, D.A. and Loui, H., Radar-cross-section reduction of wind turbines (Part 1), Sandia Report SAND2012-0480, 2012.
- [23] Henderson, F.M. and Lewis, A.J. (Eds), Principles and Applications of Imaging radar, Chapter 8, John Wiley and sons, 1998, ISBN 0-471-29406-3.
- [24] Sherry, M., Sheridan, J. and Lo Jacono, D. Characterization of a horizontal axis wind turbines tip and root vortices, Experiments in fluids, V54, 2013.
- [25] Odemark, Y., Wakes behind wind turbines – Studies on tip vortex evolution and stability, Technical report, Swedish Royal institute of technology KTH mechanics, 2012.
- [26] Schmitz, S., Technology: wakes behind wind turbines, Wind System Magazine, May 2011, <http://windsystemsmag.com/article/detail/244/technology>, accessed September 26, 2013.
- [27] Barthelmie, R.J., Frandsen, S.T., Rathmann, O., Hansen, K., Politis, E.S., Prospathopoulos, J., Schepers, J.G., Rados, K., Cabezon, D., Schlez, W. Neubert, A, and Heath, M. Flow and wakes in large wind farms: Final report for upwind WP8, Riso-R_1765(EN), 2011.
- [28] Hojstrup, J., Courtney, M.S., Christensen, C.J. and Sanderhoff, P., Full scale measurements in wind farm arrays, Riso report Riso-I-684(EN), 1993.

- [29] Major, J.S., Hopkins, A., Gaiser, B.D. and Belen, F., Yaw control optimization, Wind systems magazine, January 2013, <http://windsystemsmag.com/article/detail/447/yaw-control-optimization>, accessed October 1, 2013.
- [30] Mamidipudi, P., Dakin, E., Hopkins, A., Belen, F.C., and Leishman, J.G., Yaw control: the forgotten control problem, Proc. European Wind Energy Association conference, Brussels, 2011.
- [31] Chiu S., Personal communication.
- [32] Gamal, A. WE handbook 2 Aerodynamics and loads, www.academia.edu, accessed April 5, 2012.
- [33] ENERCON Product Overview, http://www.enercon.de/downloads/EN_Productoverview_1710, Accessed March 26, 2014.

This page intentionally left blank.

Annex A Turbine blade models

The QinetiQ study reported in [15] examined electromagnetic scattering model calculations for the radar returns from three turbine blade designs as seen by a 3.0 GHz radar. The model used a plane wave illumination at the blade surface and four blade rotation angles (0° , 60° , 120° and 180°) were modelled for a continuum of monostatic azimuth angles between -90° and 270° where the results at -90° , 270° corresponded to the leading edge of a blade that is oriented vertically up (rotation angle 0°), 0° azimuth angle corresponds to the blade viewed from the front along the turbine axis, and 180° azimuth corresponds to the blade viewed from the rear (nacelle side) along the turbine axis. The turbine nacelle and tower were not included in these calculations nor were shadowing effects. All results were for a single turbine blade.

The turbine blades that were modelled were the Vestas V47 turbine blade (22.5 m length), the Enercon E66 turbine blade (30.8 m length) and a MEG Micon 40 m length. The model results for the Vestas V47 blade were generated for 0° blade pitch and those for the Enercon E66 and TEK Micon blades were presented for 0° , 5° and 10° pitch. For the pitch angle cases, the normal pitch angle modulation by blade rotation angle was not used. The lightning protection system was not included in any of the models.

All models used a CAD (computer aided design) hollow-shell representation of the blade without internal support structure. The CAD representation includes the blade twist. Blade pitch angle effects were modelled for some blade types and were shown to primarily affect the blade RCS values near 0° yaw and $\pm 180^\circ$ yaw. The turbine hub assembly was not modelled nor was the RCS distribution along the blade length.

This page intentionally left blank.

Annex B Turbine RCS models

Since the entire wind turbine is contained within one ASR range cell the radar returns will be the coherent sum of signals scattered from the tower, the blades, the hub and the nacelle. For turbine rotation angles other than 0° and 180° (one blade vertically up or down), two of the turbine blades (the non-vertical ones) will only be visible to the radar when the turbine yaw angle from the radar is either 0° or 180° . The vertical blades will have significant radar returns at most yaw angles.

B.1 Empirical observations

Using the Enercon E66 1.8 MW turbine as the baseline for modelling, Figure 20 shows that the envelope of the turbine RCS at 0° yaw angle can be approximately described by $RCS = A-B\cos(3\phi)$ where the turbine rotation angle $\phi = 0^\circ$ when one blade is vertically up and A-B is the radar cross section of the static components (in dBm^2) at yaw angle $\theta_Y = 0$. The yaw angle is zero when the turbine axis is aligned with the radar range vector so that the rotor is facing the radar. Analysis in [15] shows that blade returns quickly become insignificant when the yaw angle departs significantly from 0° . Figure 20 suggests that this is almost true in the real world.

To build empirical models of wind-turbine RCS as functions of yaw angle we suggest that one or two example cases for blade size, tower, and nacelle design be established as baseline references using available data and that a set of scaling laws be defined to accommodate different turbine sizes.

There are two broad classes of wind turbine nacelle design, the rounded design shown in Figure 30 that houses a low-speed multi-pole alternator (other designs with rounded shells use gear boxes and high-speed alternators) and a more rectangular design shown in Figure 31 which houses the more common combination of a gear box and a high speed alternator. Since RCS data are available for the designs shown in Figures 30 and 31, these are used to represent the two general nacelle design classes. The model can be readily adapted to additional models if RCS data are available.

The Enercon E66 turbine has a hub diameter of approximately 5 m (estimated from an image that had a standing man as a reference). The Vestas V47 turbine 660 kW discussed in [15] has the shape shown in Figure 31 and an approximate hub diameter of 2.5 m.

B.1.1 Enercon E66 turbine nacelle (rounded profile nacelle)

The Enercon E66 nacelle is taken to be a model for a nacelle design that has a rounded profile. Data points were extracted from the nacelle scattering model results presented in [15] at intervals of 5° yaw angle. The major features of the data were modeled by simple functions by sequentially minimizing a feature and modelling the residuals. The data for the Enercon turbine in [15] were generated for radars operating at 3.0 and 1.0 GHz.

Since the sample points for Figure 24 are not available the data were manually estimated from Figure 24 at $5^\circ \pm 2^\circ$ intervals and approximately ± 0.5 dB estimation accuracy to create the data in

Figure B.3 that were used for model generation. The coherent fading effects seen at 1.0 GHz in Figure 25 were not extracted.

Figure B.1 shows the results for a 3.0 GHz radar. Yaw is 0° when the nacelle is viewed from the rotor end.

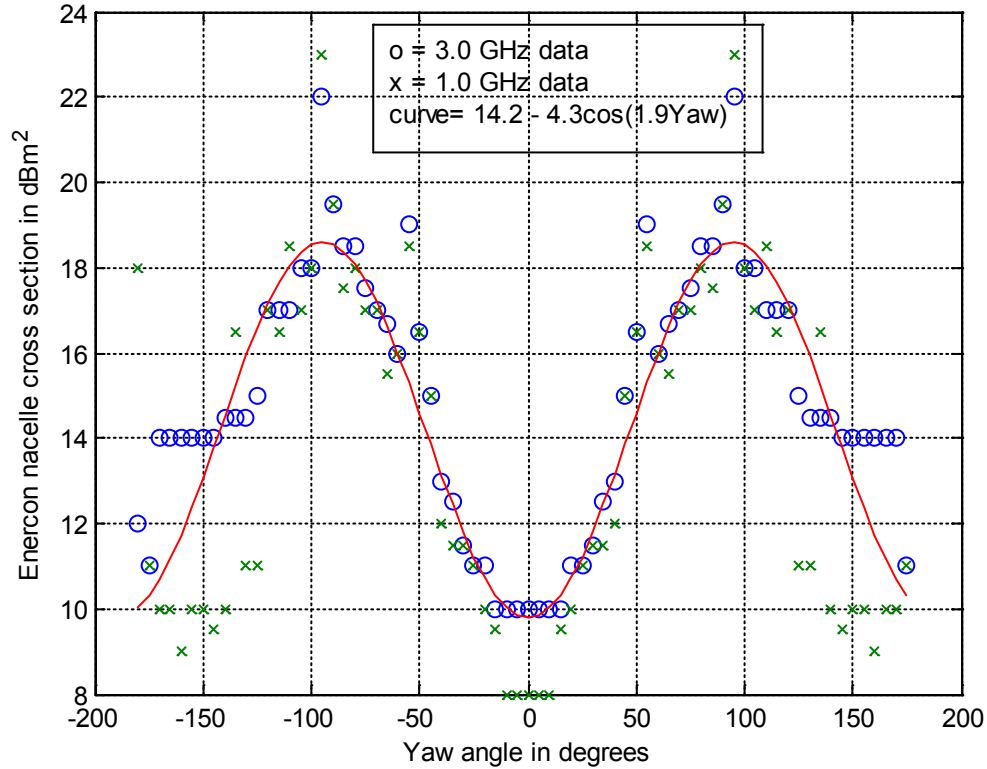


Figure B.1: Data extracted from a figure in [15] for an Enercon E66 turbine nacelle modeled at 3.0 GHz and 1.0 GHz.

The data from [15] show differences between the nacelle cross section estimates for 3.0 GHz and 1.0 GHz radars, however, a simple descriptive model of the data was only constructed for the 3 GHz radar data to represent signals seen from an S-band ASR.

Starting with the 3 GHz data points the major feature of the 3 GHz data can be modelled using a cosine transform of the data points. θ_Y is the yaw angle and $\{B\}$ is the set of 3.0 GHz data points shown in Figure B.1.

To simplify the estimates, the mean RCS and the four peaks from the sampled data set B are removed to define a somewhat smoothed RCS data-point set $\{A\}$ that has zero mean:

$$\{A\} = \{B\} - \text{mean}(\{B\}) - 4 \cdot \exp(-.25 \cdot \text{abs}(\text{abs}(\theta_Y) - 95^\circ)) - 3.5 \cdot \exp(-.25 \cdot \text{abs}(\text{abs}(\theta_Y) - 55^\circ)) \quad (\text{B.1})$$

The mean value of $\{B\}$ is $C = 15.11 \text{ dBm}^2$ for the available data and the RCS peaks for the nacelle are modeled in equation (B.1) as simple exponential functions scaled to the data points.

When the spike features and mean are removed from the nacelle data, the rest of the nacelle signature is modeled as a discrete cosine transform whose Fourier coefficients are:

$$F_k = \frac{1}{n} \sum_{m=1}^n A_m \cos(N_k \theta_Y(m)) \quad (\text{B.2})$$

where A_m are the sample points in $\{A\}$ describing the nacelle RCS, N_k is the “frequency” corresponding to the k^{th} coefficient, n is the number of data points and $\theta_Y(m)$ is the yaw angle corresponding to each data point A_m .

The Fourier coefficients F_k are listed in Table B.1.

Table B.1: Enercon E66 nacelle Fourier coefficients.

N_k	Fourier coefficient, F_k	N_k	Fourier coefficient, F_k
0	-0.6762	10.5	-0.3682
0.5	-0.6109	11	-0.1283
1	-0.9950	11.5	-0.0125
1.5	-2.1962	12	-0.1488
2	-2.9857	12.5	-0.0849
2.5	-2.1357	13	0.1965
3	-0.4487	13.5	0.1871
3.5	0.3714	14	-0.1159
4	0.1276	14.5	-0.1241
4.5	-0.1002	15	0.2416
5	0.0522	15.5	0.3625
5.5	0.0470	16	0.0361
6	-0.1590	16.5	-0.1822
6.5	-0.0589	17	-0.0064
7	0.2490	17.5	0.1286
7.5	0.1955	18	-0.0500
8	-0.0953	18.5	-0.1794
8.5	-0.0013	19	-0.0230
9	0.3641		
9.5	0.3022		
10	-0.1775		

To regenerate the nacelle RCS for any number of samples, n , of the yaw angle interval $-180^\circ \leq \theta_Y < 180^\circ$, the model is generated in degrees by $\theta_Y = [-180:360/n:180-360/n]$ and the nacelle model is:

$$RCS(\theta_Y(m)) = \frac{1}{2} \sum_{k=1}^K F_k \cos(N_k \theta_Y(m)) + 4e^{-0.25 \text{abs}(\text{abs}(\theta_Y(m)) - 95)} + 3.5e^{-0.25 \text{abs}(\text{abs}(\theta_Y(m)) - 55)} + C \quad (\text{B.3})$$

where abs is the absolute value function.

The model is displayed in Figure B.2 for 76 data points and 39 Fourier coefficients.

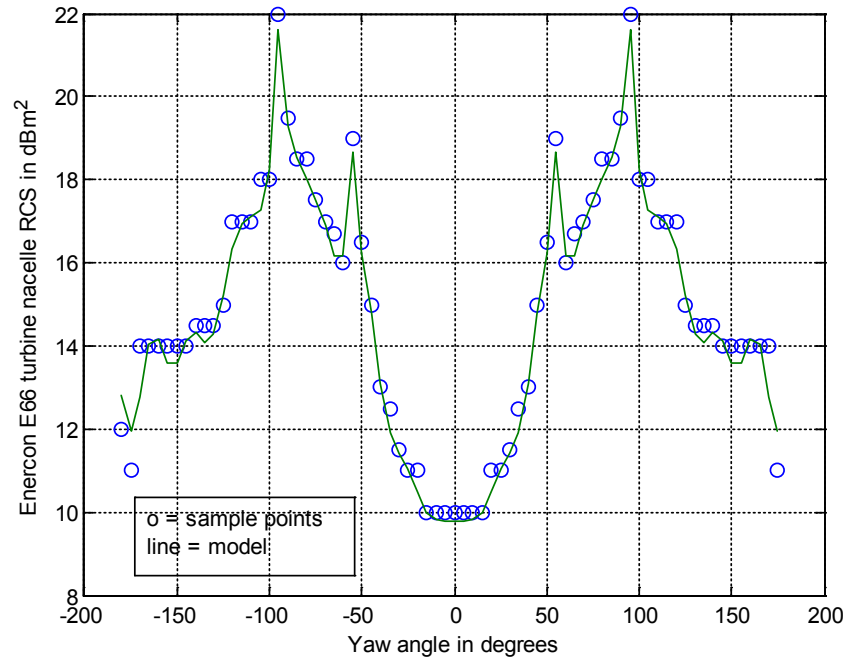


Figure B.2: Enercon E66 turbine nacelle RCS at 3.0 GH.

The residuals between the sample points and the RCS model are displayed in Figure B.3.

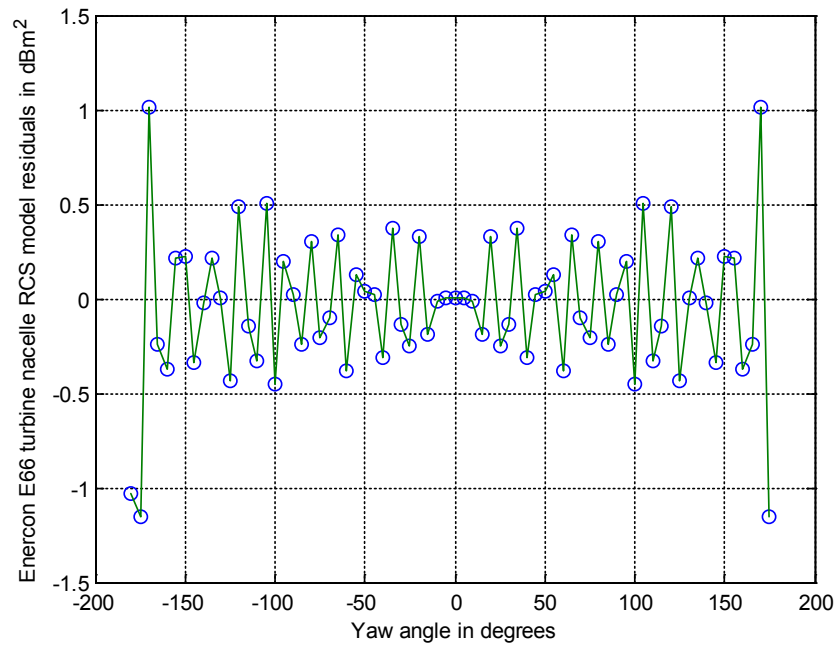


Figure B.3: *Model residuals for the Enercon E66 turbine nacelle model.*

The standard deviation of the residuals is 0.3857 dBm^2 and is compatible with the expected errors in extracting the sample points from Figure 24.

B.1.2 Vestas V47 turbine nacelle (rectangular profile nacelle)

The Vestas V47 turbine nacelle is taken to be a model for a wind turbine nacelle that has a rectangular profile. The major features of the data were modeled by simple functions by sequentially minimizing a feature and modelling the residuals. The data for the Vestas turbine in [15] were generated by electromagnetic scattering models for radars operating at 3.0 and 1.0 GHz.

Since the sample points for Figure 26 are not available, the data were manually estimated from Figure 26 at $5^\circ \pm 2^\circ$ intervals and approximately $\pm 0.5 \text{ dB}$ estimation accuracy to create the data in Figure B.4 that were used for model generation.

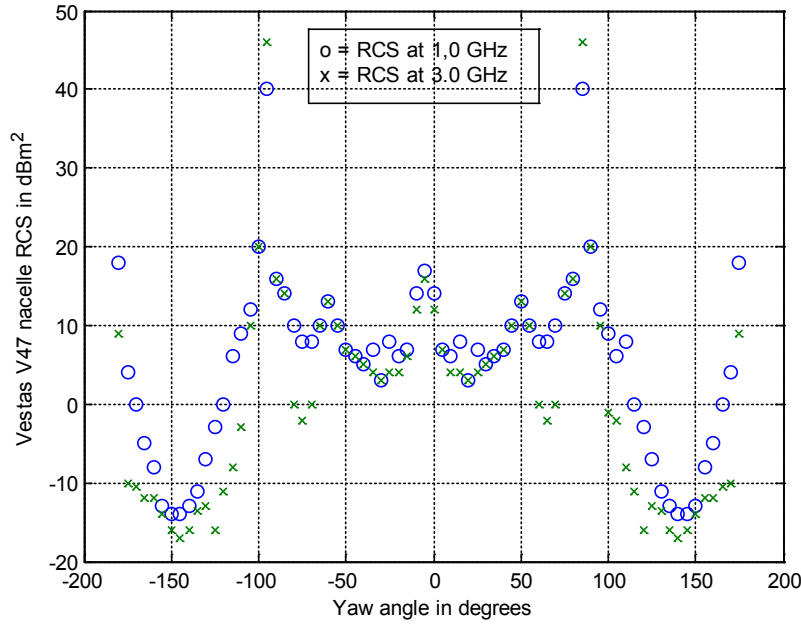


Figure B.4: Data extracted from a figure in [15] for a Vestas V47 turbine nacelle modeled at 3.0 GHz and 1.0 GHz.

As was the case for the mathematical description of the Enercon nacelle RCS, a model description of the Vestas nacelle RCS at 3.0 GHz was constructed in sequential layers. The Vestas V47 nacelle RCS is dominated by the flat panel glint returns at $\pm 90^\circ$ yaw angle. These features can be modelled as the sum of two functions M1 and M2 whose parameters are derived from the 3.0 GHz data points shown in Figure B.4:

$$x1 = \frac{\theta_Y + 90}{18}, x2 = \frac{\theta_Y - 90}{18}, M1 = 25(\text{sinc}(x1) + \text{sinc}(x2)), M2 = 25e^{-||\theta_Y| - 90|} \quad (B.4)$$

The next major feature is a spike at the aft end of the nacelle which can be modelled as:

$$M3 = 22e^{-5(180-|\theta_Y|)} \cos(11.7\theta_Y) \quad (B.5)$$

After removing the spikes, the DC bias ($C = -2.2349 \text{ dBm}^2$ for this case) is removed.

When the spike features are removed from the nacelle data, the rest of the nacelle signature is modeled as the discrete cosine transform using equation (B.2).

The Fourier coefficients for the Vestas nacelle data are given in Table B.2.

Table B.2: *Vestas nacelle Fourier coefficients.*

N_k	Fourier coefficient, F_k	N_k	Fourier coefficient, F_k
0	0	10.5	-0.1773
.5	3.9383	11	-0.2726
1	12.2412	11.5	0.4310
1.5	8.2369	12	1.5411
2	0.3416	12.5	2.1405
2.5	-4.7313	13	1.6895
3	-2.5814	13.5	0.5743
3.5	1.5472	14	-0.2783
4	1.6175	14.5	-0.3733
4.5	-1.1909	15	-0.0799
5	-1.9082	15.5	0.0192
5.5	0.6771	16	-0.1106
6	3.3778	16.5	-0.1624
6.5	3.6487	17	-0.0948
7	2.1027	17.5	-0.0079
7.5	0.5008	18	0.2852
8	-0.3534	18.5	0.8902
8.5	-0.4828	19	1.2496
9	-0.1117	19.5	0.7263
9.5	0.2993	20	-0.2956
10.	0.2472		

For any number of samples, K , in the yaw angle interval $-180^\circ \leq \theta_Y < 180^\circ$, the nacelle model is:

$$RCS_m = \frac{1}{2} \sum_{k=1}^K F_k \cos(N_k \theta_Y(m)) + 25 \left(\text{sinc} \left(10 \frac{\theta_Y(m) + 90}{180} \right) + \text{sinc} \left(10 \frac{\theta_Y(m) - 90}{180} \right) \right) + 25e^{-\text{abs}(\text{abs}(\theta_Y(m) - 90))} + 22e^{-5(180 - \text{abs}(\theta_Y(m)))} \cos(11.7\theta_Y(m)) + C \quad (\text{B.6})$$

where abs is the absolute value function.

The model is displayed in Figure B.5 for 76 data points and 21 Fourier coefficients.

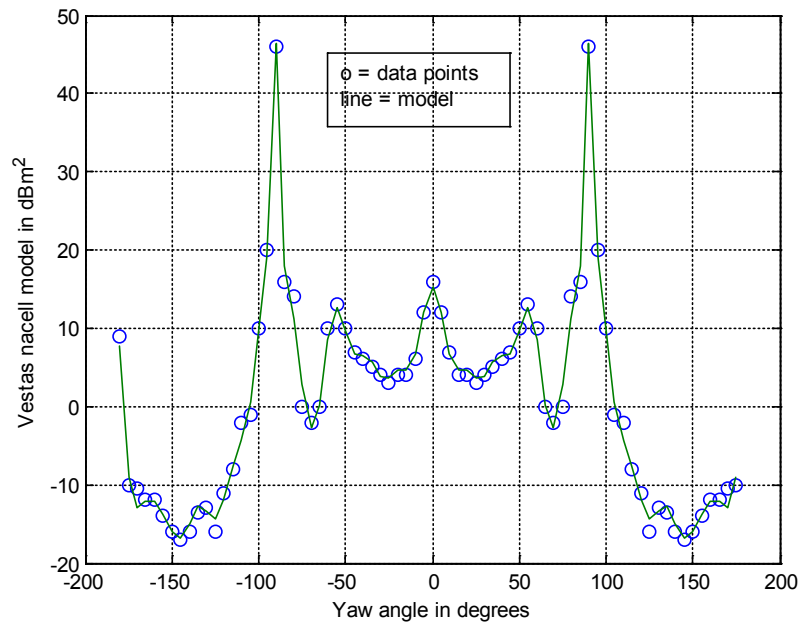


Figure B.5: *Vestas V47 nacelle model RCS showing the source data points.*

The residuals between the nacelle model and the source data points are shown in Figure B.6 as a function of yaw angle.

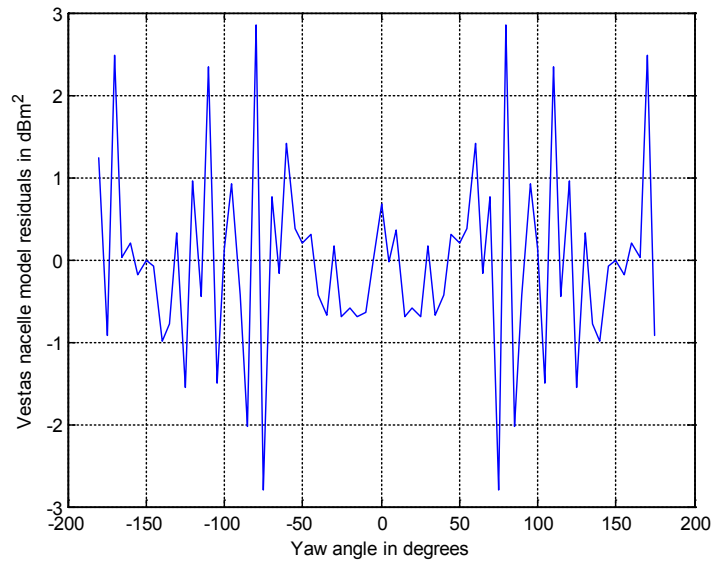


Figure B.6: *Vestas V47 nacelle model residuals.*

The model residuals have a standard deviation of 1.1450 dBm² which is dominated by the data point extraction error.

B.2 Matlab scripts for wind turbine RCS and spectrum modelling

The scripts introduced in this section are developmental tools that have not been optimized for computational efficiency. They are internally annotated to simplify modification and further development and are modular in form. The code can be easily modified to include cases that are not supported by available data at the time of writing.

Although a number of different cases have been tested, testing is not complete. Although the developmental scripts are introduced in this annex, the model Matlab code is not published in this report. Access to the developmental model code can be obtained through the DRDC Ottawa Technology Exploitation group (613) 998-3210 which reports to Director S&T External Relations (613) 995-8022.

B.2.1 Matlab script for the turbine RCS model

% This script is an empirical model based on published data. Computed values are based on reference turbine parameters and are scaled for other systems by simple scaling laws. Low RCS technology has not been included.

% Nacelle models are based on data from a nominally representative rounded nacelle design (Enercon E66 turbine) and a nominally representative flat sided nacelle design (Vestas V47 turbine).

%The tower RCS is based on analysis for a 67 m steel tower that was used for the Swatham UK turbine.

% The rotor blade model is based on the Enercon E66 design.

%

% custom functions that are used in these calculations are rad.m, deg.m, modulo_180.m

%

% Author: Chuck Livingstone August 30, 2013, correct Hub RCS September 24, 2013, correct hub shadow September 30, 2013

%

% Reference parameters

% Tower height m

HTref=67;

% Tower RCS m²

RTref=100;

% Reference blade length (m)

LBref=32.5;

%Rotor radius reference (Enercon) in m

LReref=33.5;

% Rotor hub diameter (Enercon) in m

HubE=5;

% Rotor diameter (Vestas) in m

LRVref=20;

% Rotor hub diameter (Vestas) in m;

HubV=2.5;

% Maximum blade RCS at yaw = $\pm 90^\circ$

```

        BRCSref = 1000;
%
%Input Turbine parameters
    %Tower Height (m)
        HT=67;
    %Rotor radius (m)
        LR=33.5;
    %Turbine hub diameter (m). If this number is unknown enter 0.
        DH=5;
    % Surface roughness parameter for scattering angle estimation (degrees)
        Beta=3.4;
    % Hub blade root roughness parameter for scattering angle estimation as a function of
    rotation angle
        Gamma= 20;
    % Blade tip feature roughness parameter for scattering angle estimation as a function of
    rotation angle
        Delta=40;
    % Cut-in wind speed (m/s)
        Vstart=4;
    % Rated wind speed (m/s)
        Vrate=13;
    % Cut-out wind speed (m/s)
        Vstop=25;
    % Start RPM
        RPMmin= 6;
    %Rated RPM
        RPMrate=16;
    % Nacelle type: Selector switch S=1 selects the Enercon E6 (rounded nacelle) turbine
    model, S=2 selects the Vestas V47 (rectangular nacelle) turbine model.
        S=1;
%
%Input environmental parameters
    % Wind speed (m/s)
        Vwind=16;
    % Wind direction (from, clockwise from north) in degrees
        Awind=0;
%
% Input radar observation parameters
    % Terrain shadow mask height at the tower base (m)
        h=0;
    % Radar wavelength (m)
        lam=0.1;
    % Turbine bearing angle
        Aturb=270;
    % Radar azimuth beam-width (degrees)
        Arad=3;
    % Radar range to the turbine (km)
        Rad=37;

```

```

% Turbine elevation angle at the radar
    Aelev=0;
% Radar scan rate (RPM)
    RPMrad=12;
% Radar PRF (Hz)
    PRF=900;
% Radar pulse length in micro-seconds
    Tpulse=1;
%
% Model calculation parameters
% Initial blade angles
    zeta=rad([0,120,240]);
%Turbine rotation angle for blade vertically up or down
    Bu=[0,120,240,360,480];
    Bd=Bu+60;
%
% Model calculations (Available on request)
%
```

B.2.2 Simple high-pass filter model

```

% This script defines a simple, two-pole high pass filter with a cut-off frequency  $f_c$ 
%
% Author: Chuck Livingstone August 31, 2013
%
% Computation script (Available on request)
```

B.2.3 Script for rendering the Doppler and RCS matrices as a normalized power spectrum

```

% This script creates a turbine Doppler power spectrum image using RCS rotor model
estimates. The spectrum is normalized to 0 dBm2 at 0 Hz.
% The radar range, gain and antenna pattern terms are not included nor are the static
components at zero Doppler.
% The input parameters are:
    % The turbine rotation rate Omeg (rad/s)
    % The turbine radius vector, R
    % The turbine rotation angle vector, Phi
    % The negative Doppler hub matrix, fHn
    % The positive Doppler hub matrix, fHp
    % The negative Doppler blade matrix, fBn
    % The positive Doppler blade matrix, fBp
    % The blade tip Doppler matrix, fT
    % The turbine rotor hub RCS
    % The turbine blade RCS for positive Doppler BRCSp
    % The turbine blade RCS for negative Doppler, BRCSn
    % The turbine blade tip RCS feature BT
%
```

```

% Author Chuck Livingstone: This version September 3, 2013
%
% Algorithm script (Available on request)
%

```

B.2.4 Terrain shadow mask for turbine RCS screening

% This script implements a shadow mask filter for use in estimating the effective RCS of a wind turbine that has been partially masked by intervening terrain.

% The shadow mask script requires that the turbine RCS model script has been run and that the RCS model parameters are in local memory.

% The calculation assumes that the shadowed portion of the turbine is described by the shadow height, h , that is contained in the model's radar observation parameter input block. This height is defined with respect to the tower base and has been derived from radar observation geometry models.

% The parameters required for the shadow mask calculations are:

```

% The tower height in m, HT,
% The tower RCS in m^2, Trcs,
% The nacelle height in m, Hn,
% The nacelle RCS in m^2, Nracs,
% The rotor radius in m, LR,
% The rotor radius scale factor, Lscale
% The hub diameter in m, DH,
% The rotor tip minimum radius RT,
% The rotor rotation angle in degrees, Phi,
% The rotor radius vector R,
% The rotor rotation rate Omeg,
% The rotor hub RCS matrix HRCS,
% The advancing blade RCS matrix, BRCSp,
% The retreating blade RCS matrix, BRCSn,
% The blade tip feature RCS matrix, TRCS,
%

```

% Author: Chuck Livingstone, this version September 9, 2013

```

%
% Algorithm script (Available on request)
%

```

Annex C Turbine RCS yaw angle dependence

The Enercon E66 wind turbine's radar signature as a function of yaw angle is illustrated by a set of figures that span the yaw range from -10° to -170° using the RCS yaw model shown in Table 6 and Figure 43. The symmetry of this model allows half of the yaw angle range to be used. The more complex model shown in Table 5 breaks the symmetry between the positive and negative angle ranges.

Yaw angle -10° .

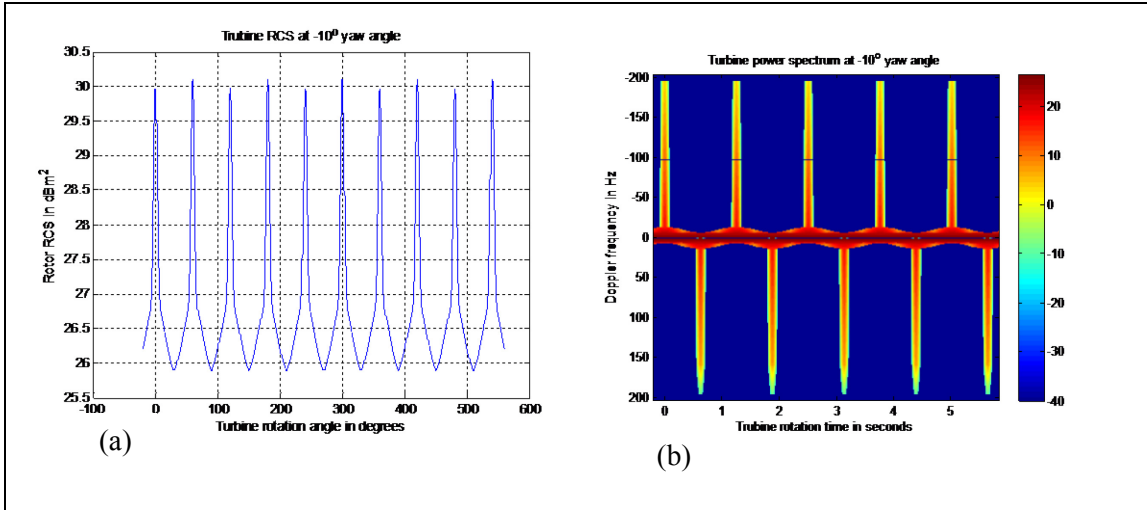


Figure C.1: (a) Turbine RCS at -10° yaw angle (b) Turbine power spectrum as a function of rotation time. The color bar scale is the power density in dBm^2 .

Yaw angle -20° .

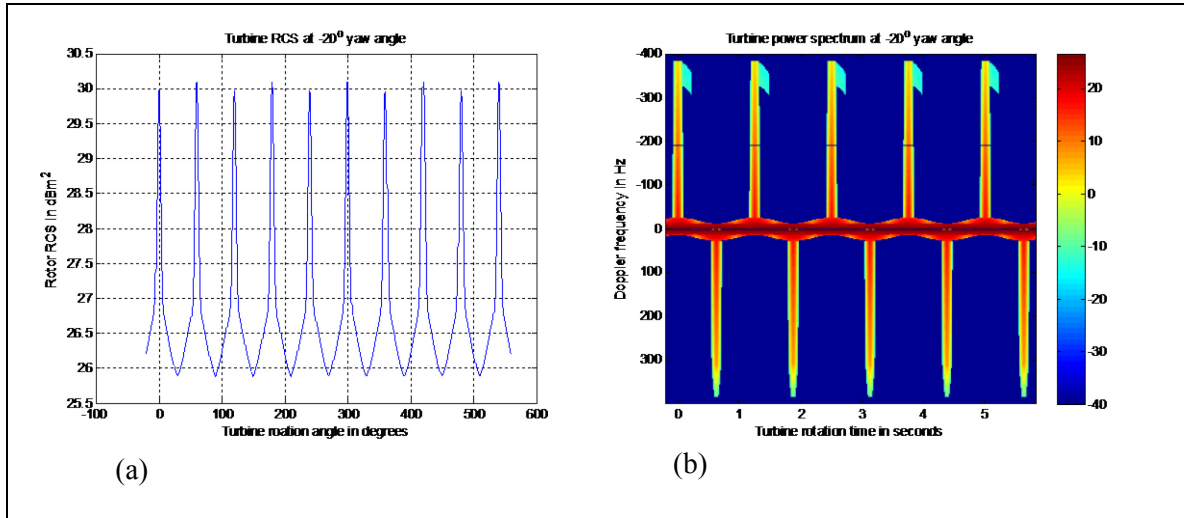


Figure C.2: (a) Turbine RCS at -20° yaw angle (b) Turbine power spectrum as a function of rotation time. The color bar scale is the power density in dBm^2 .

Yaw angle -30° .

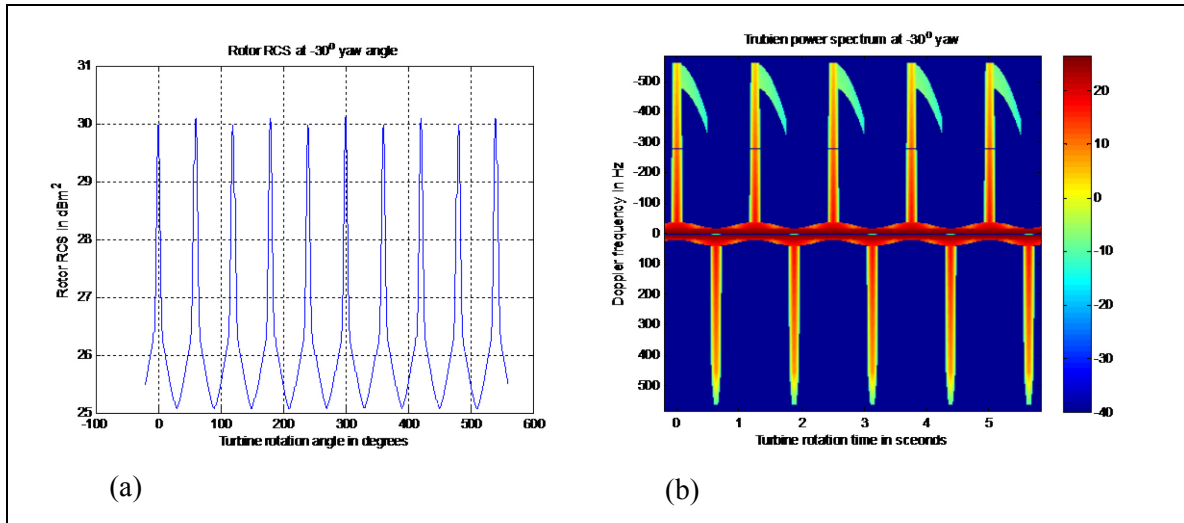


Figure C.3: (a) Turbine RCS at -30° yaw angle (b) Turbine power spectrum as a function of rotation time. The color bar scale is the power density in dBm^2 .

Yaw angle -40° .

Note the RCS scale changes as the yaw angle enters its low RCS regime.

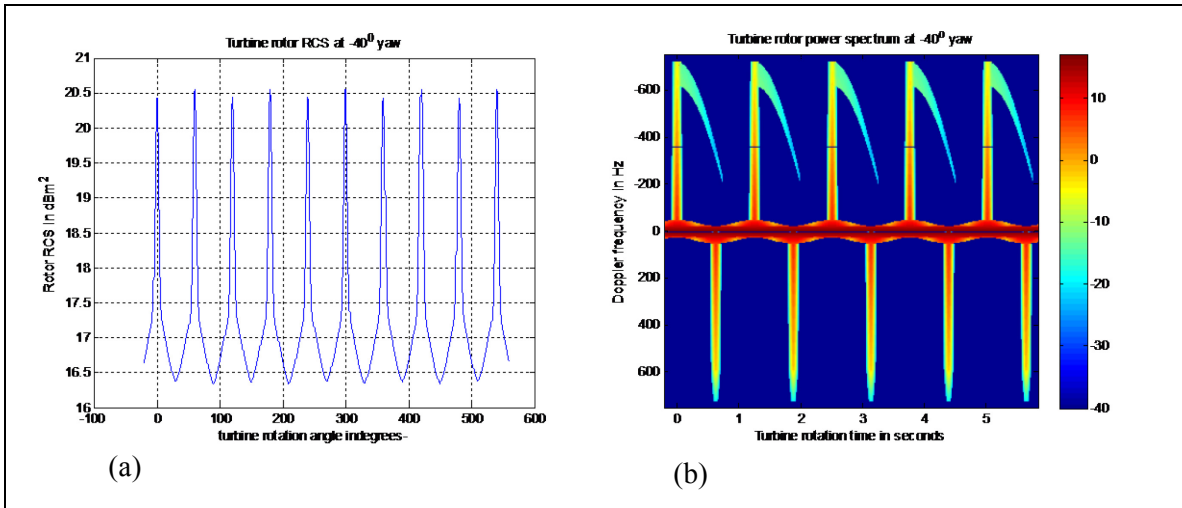


Figure C.4: (a) Turbine RCS at -40° yaw angle (b) Turbine power spectrum as a function of rotation time. The color bar scale is the power density in dBm^2 .

Yaw angle -50° .

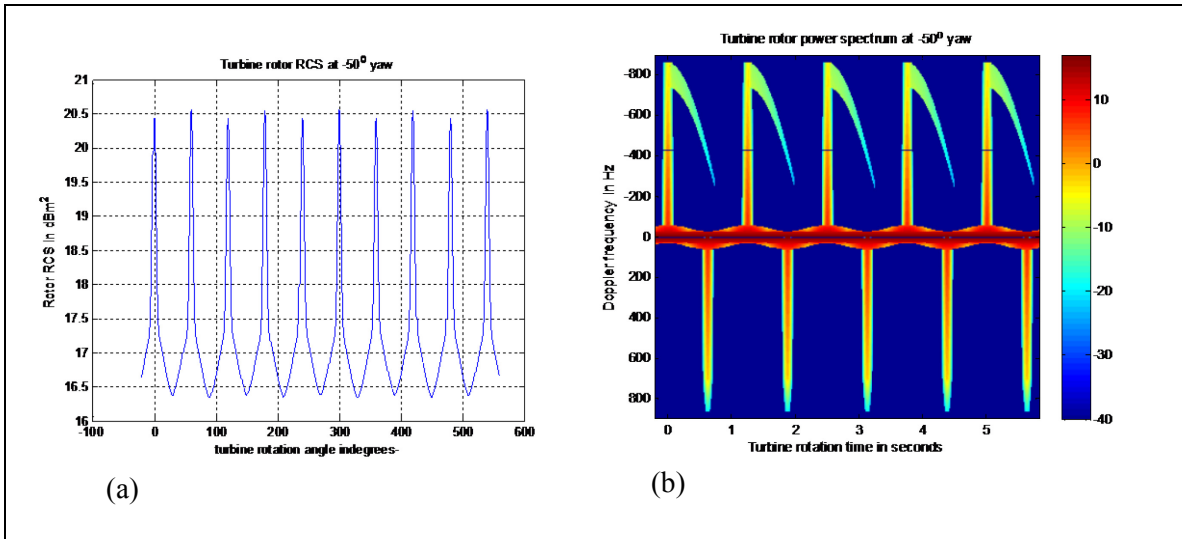


Figure C.5: (a) Turbine RCS at -50° yaw angle (b) Turbine power spectrum as a function of rotation time. The color bar scale is the power density in dBm^2 .

Yaw angle -60° .

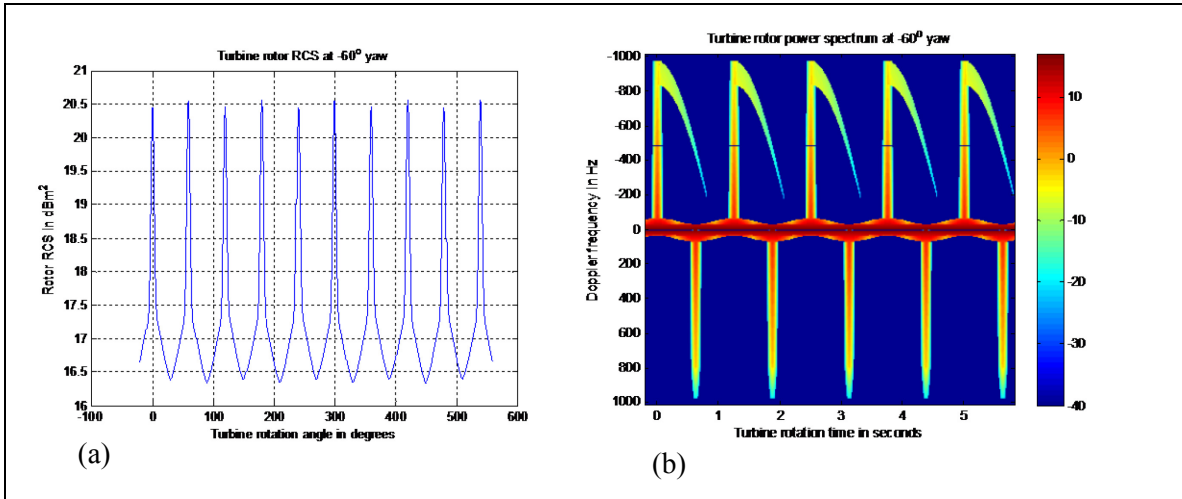


Figure C.6: (a) Turbine RCS at -60° yaw angle (b) Turbine power spectrum as a function of rotation time. The color bar scale is the power density in dBm^2 .

Yaw angle -70° .

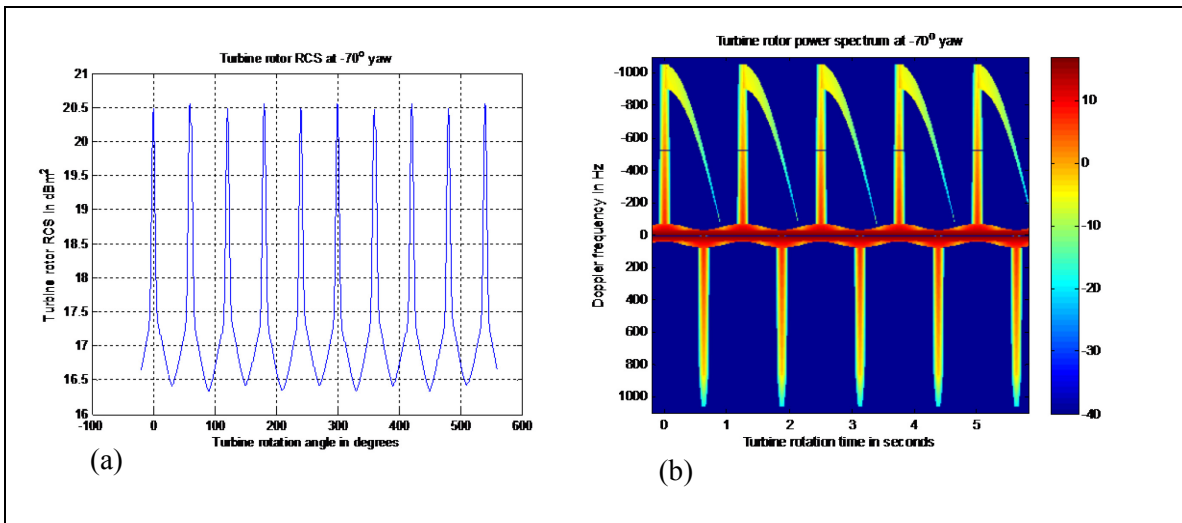


Figure C.7: (a) Turbine RCS at -70° yaw angle (b) Turbine power spectrum as a function of rotation time. The color bar scale is the power density in dBm^2 .

Yaw angle -80° .

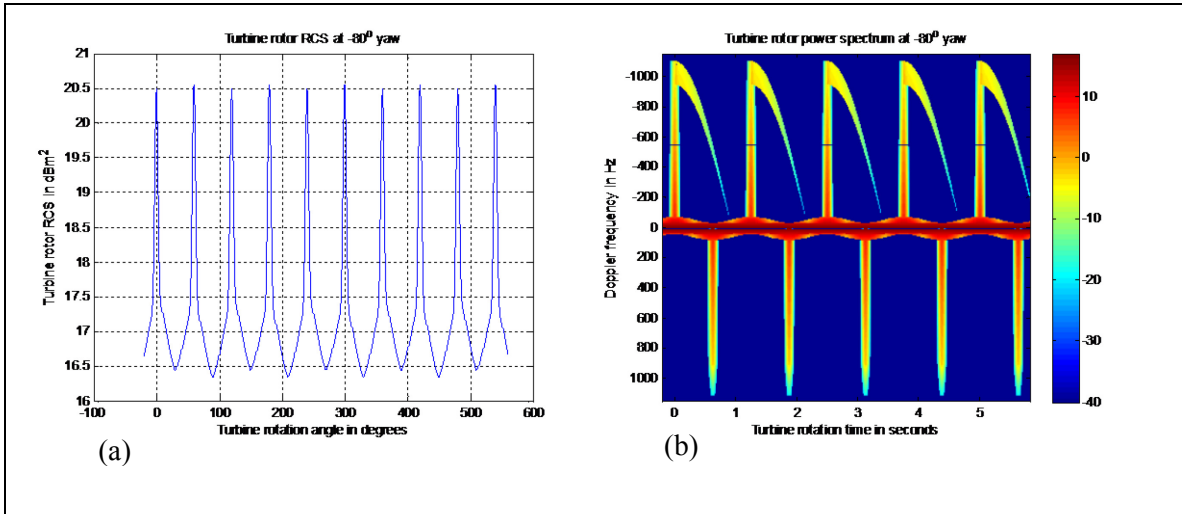


Figure C.8: (a) Turbine RCS at -80° yaw angle (b) Turbine power spectrum as a function of rotation time. The color bar scale is the power density in dBm^2 .

Yaw angle -90° .

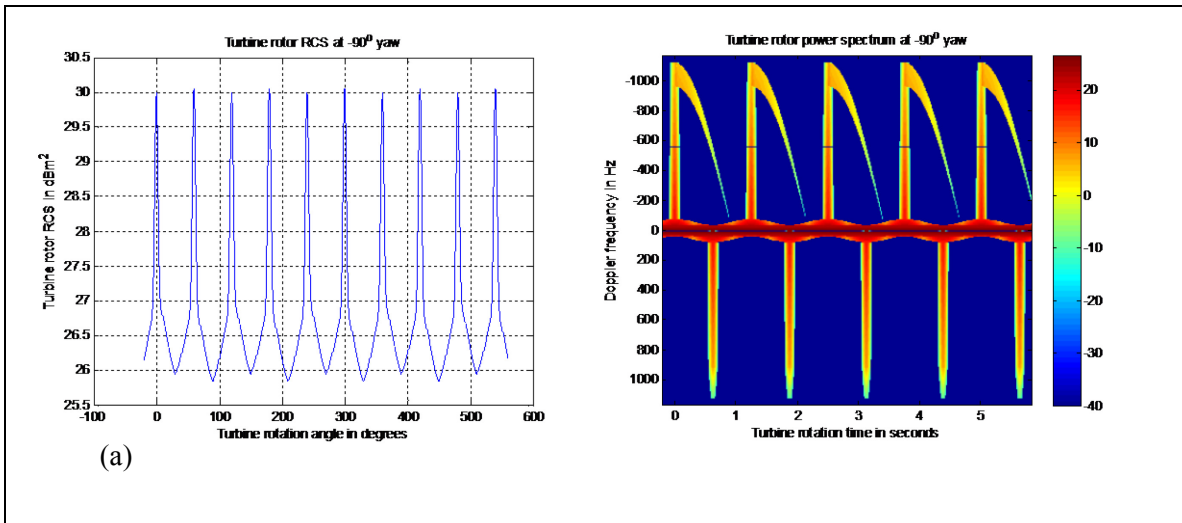


Figure C.9: (a) Turbine RCS at -90° yaw angle (b) Turbine power spectrum as a function of rotation time. The color bar scale is the power density in dBm^2 .

Yaw angle -100° .

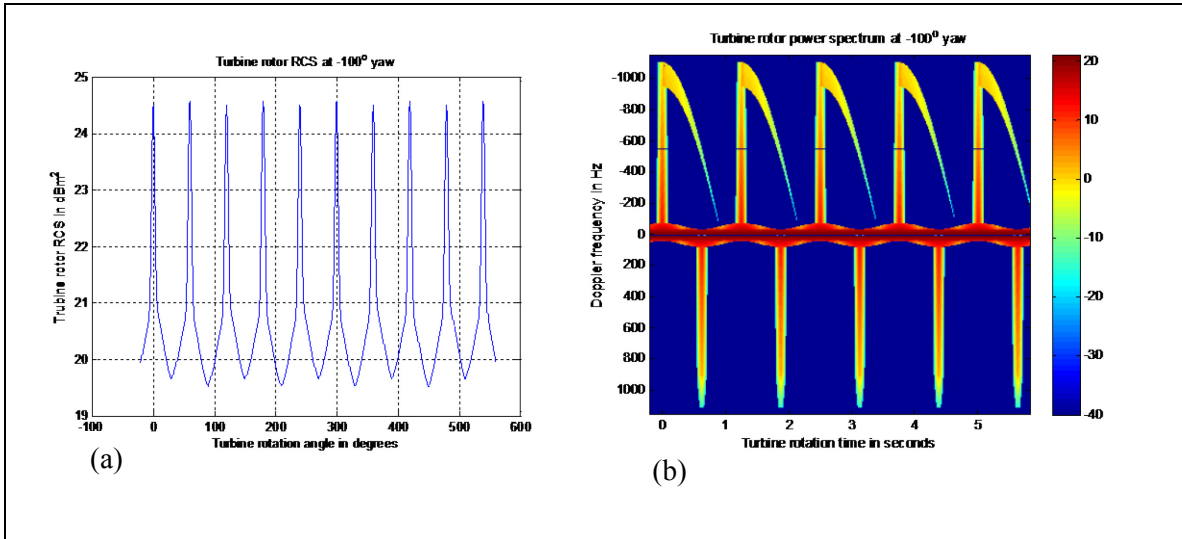


Figure C.10: (a) Turbine RCS at -100° yaw angle (b) Turbine power spectrum as a function of rotation time. The color bar scale is the power density in dBm^2 .

Yaw angle 110° .

Note the onset of the hub shadowing by the nacelle.

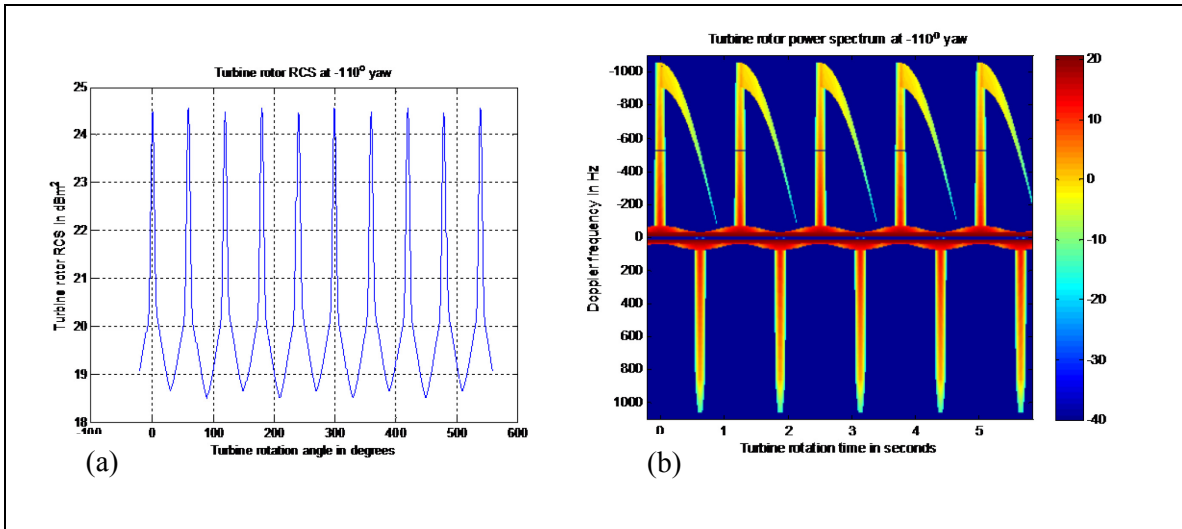


Figure C.11: (a) Turbine RCS at -110° yaw angle (b) Turbine power spectrum as a function of rotation time. The color bar scale is the power density in dBm^2 .

Yaw angle -120° .

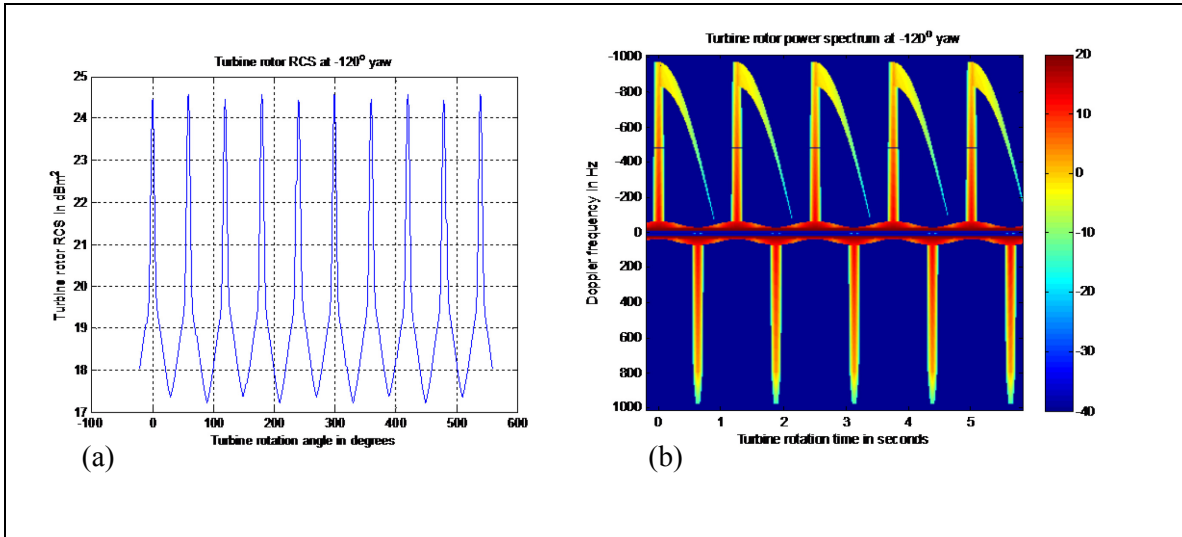


Figure C.12: (a) Turbine RCS at -120° yaw angle (b) Turbine power spectrum as a function of rotation time. The color bar scale is the power density in dBm^2 .

Yaw angle -130° .

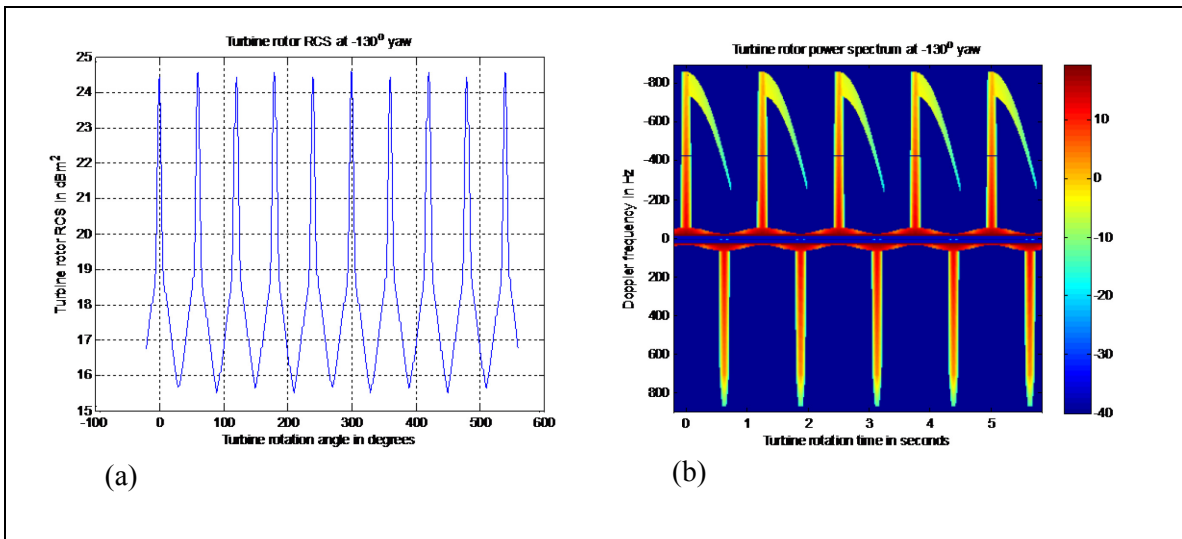


Figure C.13: (a) Turbine RCS at -130° yaw angle (b) Turbine power spectrum as a function of rotation time. The color bar scale is the power density in dBm^2 .

Yaw angle -140° .

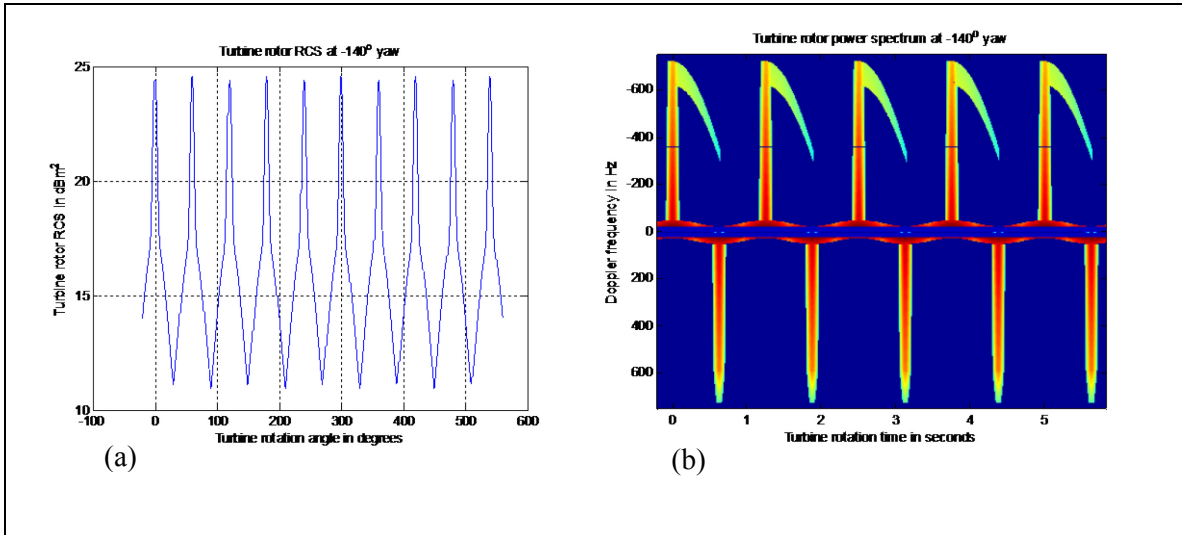


Figure C.14: (a) Turbine RCS at -140° yaw angle (b) Turbine power spectrum as a function of rotation time. The color bar scale is the power density in dBm^2 .

Yaw angle -150° .

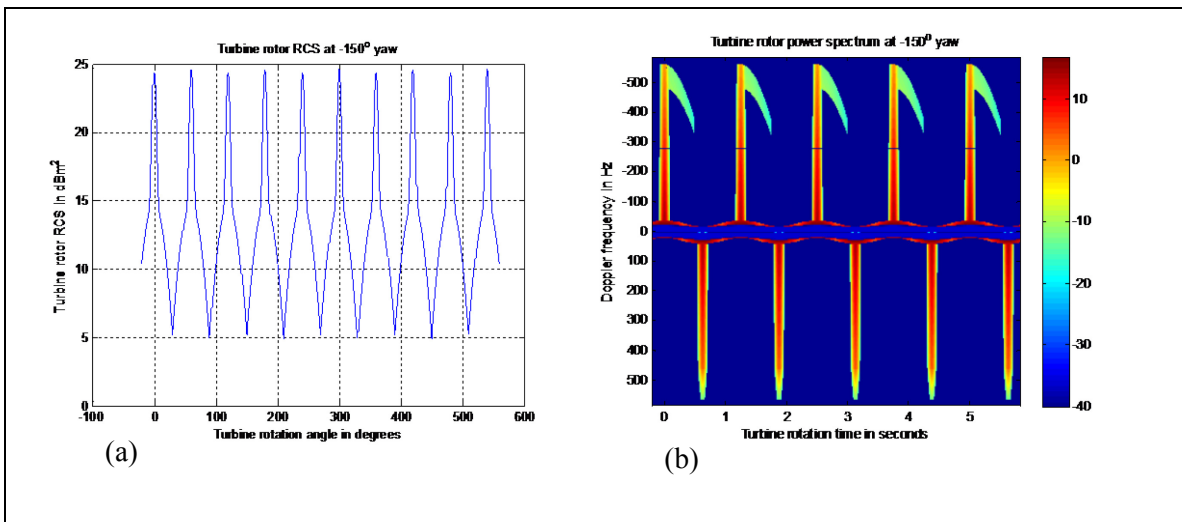


Figure C.15: (a) Turbine RCS at -150° yaw angle (b) Turbine power spectrum as a function of rotation time. The color bar scale is the power density in dBm^2 .

Yaw angle -160° .

The rotor hub is now fully screened and only the blades contribute to the dynamic RCS.

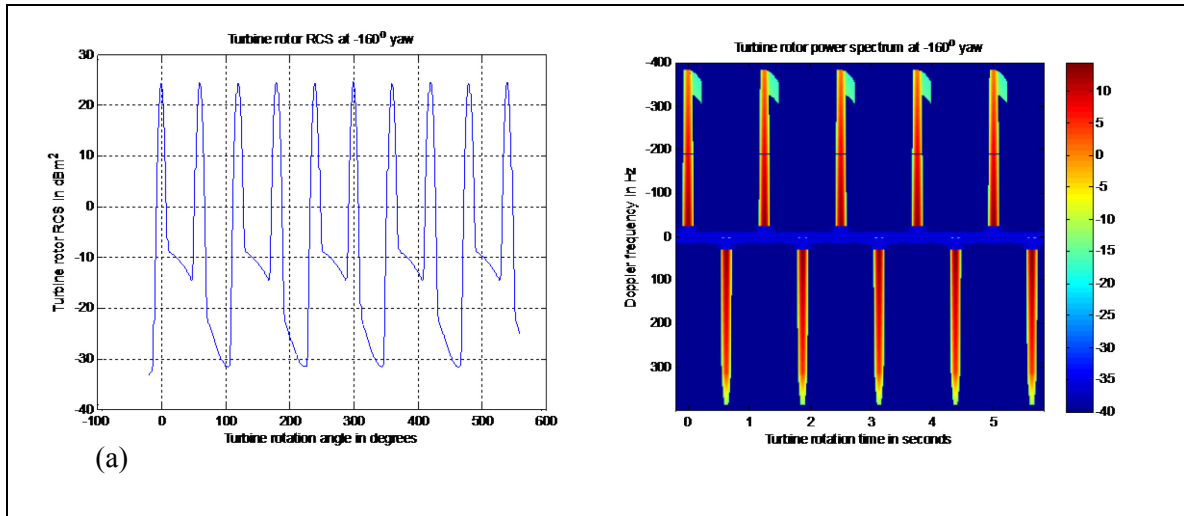


Figure C.16: (a) Turbine RCS at -160° yaw angle (b) Turbine power spectrum as a function of rotation time. The color bar scale is the power density in dBm .

Yaw angle -170° .

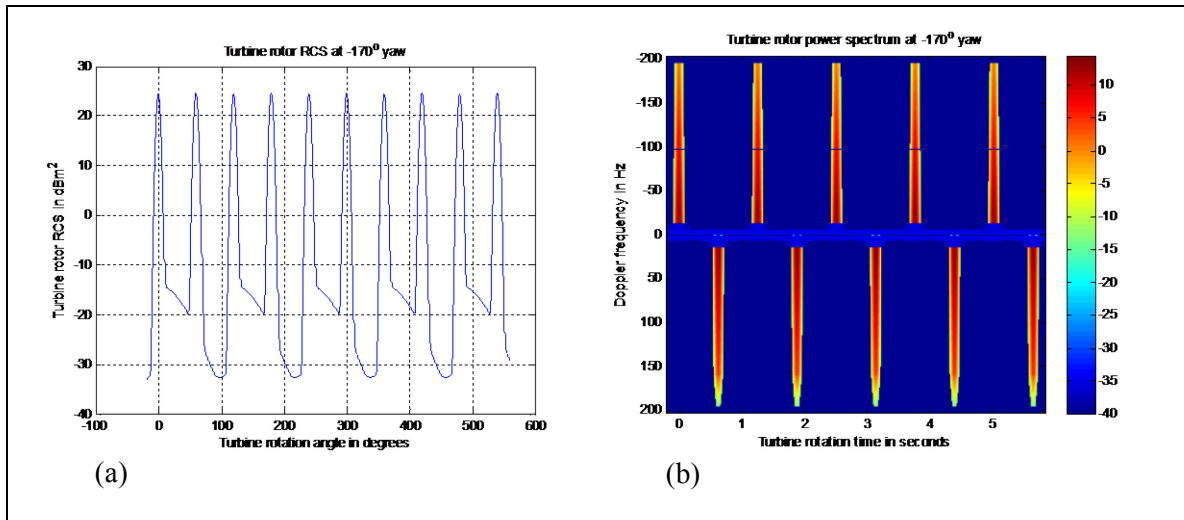


Figure C.17: (a) Turbine RCS at -170° yaw angle (b) Turbine power spectrum as a function of rotation time. The color bar scale is the power density in dBm^2 .

This page intentionally left blank.

List of symbols/abbreviations/acronyms/initialisms

ASR	Air traffic Surveillance Radar
CFAR	Constant False Alarm Rate
DND	Department of National Defence
DRDC	Defence Research and Development Canada
DSTKIM	Director Science and Technology Knowledge and Information Management
HAWT	Horizontal Axis Wind Turbine
HH	Horizontal transmit, Horizontal receive
HPF	High-Pass Filter
ISAR	Inverse Synthetic Aperture Radar
MW	Mega Watt
PRF	Pulse Repetition Frequency
R&D	Research and Development
RCAF	Royal Canadian Air Force
RCS	Radar Cross Section
RPM	Revolutions per Minute
UK	United Kingdom

This page intentionally left blank.

DOCUMENT CONTROL DATA		
(Security markings for the title, abstract and indexing annotation must be entered when the document is Classified or Designated)		
1. ORIGINATOR (The name and address of the organization preparing the document. Organizations for whom the document was prepared, e.g., Centre sponsoring a contractor's report, or tasking agency, are entered in Section 8.) Defence Research and Development Canada – Ottawa 3701 Carling Avenue Ottawa, Ontario K1A 0Z4		2a. SECURITY MARKING (Overall security marking of the document including special supplemental markings if applicable.) UNCLASSIFIED
		2b. CONTROLLED GOODS (NON-CONTROLLED GOODS) DMC A REVIEW: GCEC DECEMBER 2012
3. TITLE (The complete document title as indicated on the title page. Its classification should be indicated by the appropriate abbreviation (S, C or U) in parentheses after the title.) Ground based radar observations of wind turbines		
4. AUTHORS (last name, followed by initials – ranks, titles, etc., not to be used) Livingstone, C.;Chiu, S.		
5. DATE OF PUBLICATION (Month and year of publication of document.) August 2014	6a. NO. OF PAGES (Total containing information, including Annexes, Appendices, etc.) 121	6b. NO. OF REFS (Total cited in document.) 33
7. DESCRIPTIVE NOTES (The category of the document, e.g., technical report, technical note or memorandum. If appropriate, enter the type of report, e.g., interim, progress, summary, annual or final. Give the inclusive dates when a specific reporting period is covered.) Scientific Report		
8. SPONSORING ACTIVITY (The name of the department project office or laboratory sponsoring the research and development – include address.) Defence Research and Development Canada – Ottawa 3701 Carling Avenue Ottawa, Ontario K1A 0Z4		
9a. PROJECT OR GRANT NO. (If appropriate, the applicable research and development project or grant number under which the document was written. Please specify whether project or grant.) 15eq	9b. CONTRACT NO. (If appropriate, the applicable number under which the document was written.)	
10a. ORIGINATOR'S DOCUMENT NUMBER (The official document number by which the document is identified by the originating activity. This number must be unique to this document.) DRDC-RDDC-2014-R57	10b. OTHER DOCUMENT NO(s). (Any other numbers which may be assigned this document either by the originator or by the sponsor.)	
11. DOCUMENT AVAILABILITY (Any limitations on further dissemination of the document, other than those imposed by security classification.) Unlimited		
12. DOCUMENT ANNOUNCEMENT (Any limitation to the bibliographic announcement of this document. This will normally correspond to the Document Availability (11). However, where further distribution (beyond the audience specified in (11) is possible, a wider announcement audience may be selected.) Unlimited		

13. **ABSTRACT** (A brief and factual summary of the document. It may also appear elsewhere in the body of the document itself. It is highly desirable that the abstract of classified documents be unclassified. Each paragraph of the abstract shall begin with an indication of the security classification of the information in the paragraph (unless the document itself is unclassified) represented as (S), (C), (R), or (U). It is not necessary to include here abstracts in both official languages unless the text is bilingual.)

Wind turbines are large radar targets whose radar cross sections (RCS) contain both static and dynamic components that are major interference sources for air traffic surveillance radars (ASRs). Investigations in response to a Canadian Air Force support request revealed that currently available wind-turbine RCS models are too primitive to answer the ASR interference questions asked. This report documents the development of a first-order RCS model that uses environmental conditions to replicate the static and dynamic effects present in the radar returns from wind turbines and generates the expected Doppler signatures of wind turbine targets that cause ASR interference effects. The model uses measured data from reference wind turbines and uses published results from detailed electromagnetic scattering models to create a semi-empirical description of a wind turbine target that replicates the target's properties under all normal operating conditions. The model includes scaling laws that allow it to be used for a wide range of commercial wind turbines whose detailed designs differ from the reference cases used for model development. The model contains a terrain screening filter that allows the radar returns from a partially screened turbine to be replicated for ASR interference analysis. Results obtained from the model closely replicate published, observed effects for wind turbine targets. RCS estimates are judged to be accurate to within 5 dBm².

Les surfaces équivalentes radar (RCS) des éoliennes comptent tant des éléments dynamiques que des éléments statiques; cela en fait de fortes sources d'interférences pour les radars de surveillance aérienne (ASR). Des études faites à la suite d'une demande de soutien de la Force aérienne du Canada ont révélé que les modèles RCS actuels des éoliennes sont trop simplistes pour répondre adéquatement aux questions sur les interférences touchant les ASR. Le rapport décrit le développement d'un modèle RCS de premier ordre qui reproduit à l'aide des conditions ambiantes les effets sur l'écho radar des éléments statiques et dynamiques des éoliennes et qui génère les signatures Doppler prévues des éoliennes qui créent les interférences touchant les ASR. À l'aide de données mesurées d'éoliennes de référence et de résultats publiés de modèles détaillés de diffusion électromagnétique, le modèle crée une description semi-empirique d'une éolienne qui en reproduit les propriétés dans toutes les conditions ambiantes normales. Le modèle intègre aussi des règles d'échelonnage qui lui permet de reproduire un grand nombre d'éoliennes commerciales dont la conception détaillée diffère des éoliennes de référence utilisées pour le développer. Il comporte aussi un modèle de filtrage du terrain qui permet aux fins d'analyse des interférences ASR de reproduire les échos radar d'une éolienne partiellement occultée par le terrain. Ce modèle reproduit étroitement les effets radar observés et publiés des éoliennes. Nous jugeons que les surfaces équivalentes radar sont fidèles à une précision de plus ou moins 5 dBm².

14. **KEYWORDS, DESCRIPTORS or IDENTIFIERS** (Technically meaningful terms or short phrases that characterize a document and could be helpful in cataloguing the document. They should be selected so that no security classification is required. Identifiers, such as equipment model designation, trade name, military project code name, geographic location may also be included. If possible keywords should be selected from a published thesaurus, e.g., Thesaurus of Engineering and Scientific Terms (TEST) and that thesaurus identified. If it is not possible to select indexing terms which are Unclassified, the classification of each should be indicated as with the title.)

ASR interference; wind turbine; radar cross section; Doppler spectrum; terrain masking

